Universität Rostock Traditio et Innovatio

Surface-modified interactions between Rydberg atoms

Dissertation
zur Erlangung des akademischen Grades
doctor rerum naturalium (Dr. rer. nat.)
der Mathematisch-Naturwissenschaftlichen Fakultät
der Universität Rostock

vorgelegt von
M.Sc. Johannes Block, geb. am 9. November 1990 in Lüneburg

Rostock, den 23.06.2021

https://doi.org/10.18453/rosdok_id00003717

Gutachter:
Prof. Stefan Scheel, Universität Rostock, Institut für Physik
Prof. Stefan Buhmann, Universität Kassel, Institut für Physik

Jahr der Einreichung 2021
Jahr der Verteidigung 2022

Don't panic.

Abstract

Rydberg atoms are highly excited atoms that offer a plethora of possible applications due to their intriguing properties. One of the key features of Rydberg atoms is the Rydberg blockade where only a single Rydberg excitation in a certain volume is allowed. This blockade mechanism is a direct result of the strong interactions between Rydberg atoms via the van der Waals potential. The van der Waals force belongs to the dispersion forces that originate in the quantum nature of the electromagnetic field. It is well known from the theory of dispersion forces that macroscopic objects in the vicinity of particles can influence the interaction potential significantly. Since many Rydberg atomic experiments are conducted near surfaces, the question arises to what extend these surfaces play a role in the experiments or whether these boundary effects can be utilized. In this work both one-particle and two-particle systems in front of surfaces are investigated. Internal atom dynamics for a single atom are investigated up to a fourth order equation of motion. For two particles, both analytical and numerical investigations of the pair potential as a function of surface distance are conducted. It is shown that there is a window of surface distances where surface-induced molecules of two Rydberg atoms may exist, so-called Rydberg macrodimers.

Zusammenfassung

Rydberg-Atome sind hoch angeregte Atome die durch ihre faszinierenden Eigenschaften eine Vielzahl von Anwendungsbereichen bieten. Ein besonderer Effekt und Baustein vieler Anwendungen ist die Rydberg-Blockade, bei der in einem bestimmten Volumen nur ein einziges Atom in den Rydberzustand angeregt werden kann. Dieser Blockademechanismus folgt direkt aus den starken Wechselwirkungen zwischen Rydberg-Atomen durch das van der Waals-Potential. Die van der Waals-Kraft gehört zu den Dispersionskräften, die ihren Urpsrung in den Quanteneigenschaften des elektromagnetischen Feldes haben. Aus der Theorie zu Dispersionskräften ist es gut bekannt, dass makroskopische Objekte in der Nähe von Teilchen ihr Wechselswirkungspotential signifikant beeinflussen können. Weil auch viele Experimente mit Rydberg-Atomen in der Nähe von Oberflächen durchgeführt werden, stellt sich die Frage, inwiefern diese Oberflächen eine Rolle in den Experimenten spielen und ob die Effekte durch die Grenzflächen sogar genutzt werden können. In dieser Arbeit werden sowohl Ein-Teilchen- als auch Zwei-Teilchen-Systeme in der Nähe von Oberflächen untersucht. Die interne Dynamik eines einzelnen Atoms vor einer Oberfläche wird bis zu einer Bewegungsgleichung vierter Ordnung untersucht. Für Zwei-Teilchen-System werden sowohl analytische als auch numerische Berechnungen des Paarpotentials als Funktion des Oberflächenabstandes durchgeführt. Es wird gezeigt, dass es einen gewissen Bereich vor einer Oberfläche gibt, in dem oberflächeninduzierte Moleküle bestehend aus zwei Rydberg-Atomen, sogenannte Rydberg-Makrodimere, entstehen können.

Contents

Chapter 1.

Introduction

Highly excited atoms are known as Rydberg atoms [1]. More specifically, the outmost valence electron is excited to a state that has a main quantum number n that is much larger than the maximum naturally occurring $n_{\mathrm{nat,max}} = 7$. At such high excitations, the atomic energy spectrum becomes $E \sim E_{\mathrm{Ryd}} {n^*}^{-2}$ with Rydberg energy E_{Ryd} and effective quantum number n^*. This spectrum is similar to the well-known energy spectrum of hydrogen and, thus, allows for a relatively easy description of the underlying atomic physics. The large interest in Rydberg atoms is based on their intriguing properties. Both the lifetime τ and the radial extend of the wave function $\langle r \rangle$ reach large values as they scale with n^3 and n^2, respectively. One also finds the dipole transition moment $\langle nd|er|nf \rangle \sim n^2$ and the polarizability $\alpha \sim n^7$. All these properties make Rydberg states well accessible in experiments and suitable for a variety of applications. For example, due to the large polarizability Rydberg atoms are very sensitive to electromagnetic fields and have been used as sensors for such fields for more than 20 years [2; 3]. The interest in this form of application even has risen significantly more recently [4–10]. Atomic Rydberg states of the noble gas elements argon [2] and krypton [3] allowed measurements of electric fields to a precision level below $0.01\,\mathrm{V/m}$. Later experiments ordinarily rely on the preparation of alkali atoms in Rydberg states. Since alkali atoms possess only one electron in their outmost shell, the distinction between the negatively charged excited Rydberg electron on the one hand and the positively charged remainder of the atom naturally is very pronounced. Carter *et al.* [4] use ^{87}Rb atoms to detect fields near atom chips and benefit directly from the Rydberg states' large polarizability that is found to be 10^8 times greater than the ground state's. Rydberg atoms are also used in microwave electrometry [5; 6; 10] and radio-frequency electrometry [7; 8]. Here, rubidium [5–7; 9; 10]and cesium [7; 8] are the most frequently used elements. Meyer *et al.* [9] state that the choice of species depends on the desired or experimentally available laser colors or operating temperatures and that one atomic species is not inherently superior to others. The authors also point out that the wide spectral

coverage of Rydberg sensors and their high sensitivity make them competitive with established electric field sensors.

The external fields that Rydberg atoms are subjected to due to their task as sensors are not limited to those intentionally or necessarily turned on during an experiment. From the theory of field quantization it is known that fluctuations of the electromagnetic vacuum are always present and are the underlying reason for the emergence of dispersion forces, namely the Casimir force, the Casimir-Polder force and the van der Waals force [11–14]. Dispersion forces are an interesting field to study by themselves. For example, the Casimir effect famously derived first by Casimir [15] determines the potential between two macroscopic objects. The resulting force is attractive in general [13] but repulsive forces were suggested theoretically for certain configurations as early as 1961 [16] and observed experimentally almost 50 years later [17]. Secondly, the Casimir-Polder potential describes interactions between a macroscopic object such as an atom chip or the walls of a cavity and a microscopic object like an atom or molecule. It plays a role in scanning probe microscopy experiments that involve the scanning of a surface with a cold atom cloud [18]. The authors of [18] show that neglecting the effects of the attractive Casimir-Polder potential between the atoms and a nanotube leads to an underestimation of the nanotube's height by approximately 25%. Thirdly, the van der Waals potential acts between two microscopic objects like Rydberg atoms. Due to the Rydberg atoms' large polarizabilities they experience strong interatomic van der Waals interactions. That causes a phenomenon called Rydberg blockade [19]. Due to the interaction between two atoms, the excited states are shifted out of resonance from the exciting laser for distances smaller than a certain blockade radius R_{block}. Consequently, only one Rydberg excitation is allowed in a volume with radius R_{block}.

Another field of applications of Rydberg atoms is quantum computing and simulation [20–22]. As these reviews show, the field of quantum computing is extremely broad and the specific implementation of Rydberg atoms are manifold. One of the key features utilized in this field is the Rydberg blockade because it allows the excitation of a single atom inside an atomic ensemble. For example, quantum gates can be realized by Rydberg atoms trapped in optical lattices and using the interatomic interaction to perform the desired gate operations [23–25]. An array of trapped Rydberg atoms can also work as a quantum simulator for exotic spin systems [26]. Other approaches include Rydberg atoms trapped inside a cavity [27] or coupled to a coplanar wave guide [28].

As some of the experiments are conducted close to macroscopic objects [4; 27; 28], a closer look at the atomic interactions seems necessary. It is well known from the theory of dispersion forces, that macroscopic objects modify the interatomic van der Waals interaction

or directly interact with the atoms in form of the Casimir-Polder potential [12–14; 29]. When using Rydberg atoms in applications like sensors or as components of a quantum computer, extreme precision is asked for and knowing all parameters seems vital in order to push towards new technological limits. Therefore, the question arises how to treat the influence of surfaces on Rydberg atoms in an experiment. Does it only serve as an unwanted error source or might it be used as an additional tool to shape experiments? While the answer to this question certainly depends strongly on the concrete parameters of the experiment, one has to acknowledge that contrary to external fields, dispersion forces cannot be turned off at will and, thus, always have to be considered.

This thesis was written in order to illuminate certain aspects of the broad topic *Surface-modified interactions between Rydberg atoms*. It is organized as follows. In chapter 2, the fundamentals of classical electrodynamics are reviewed to lay the foundation for the quantization of the electromagnetic field. After that, a brief overview over different dispersion forces and their applications is presented. This is followed by an introduction to Rydberg physics. Chapter 3 covers the internal dynamics of a single atom in front of a macroscopic object. After deriving a general equation of motion in fourth order it is applied to an idealized atom in front of a dielectric plate. Rabi oscillations between the ground states of the atom are predicted and the ground work for future work is laid out. In chapter 4, we move to two atoms in front of a plate. It can be shown both by analytical and numerical means that the van der Waals interaction between two Rydberg atoms is significantly modified by the plate at close distance. For two ^{87}Rb atoms, the plate induces potential wells in the pair potential which can be associated with bound molecular states, so-called Rydberg macrodimers. In chapter 5, the results of this thesis are summarized along with a brief outlook.

Chapter 2.

Macroscopic QED, dispersion forces and Rydberg physics

In section 2.1, a brief review of classical electrodynamics is presented first in order to lay the foundation for the following quantization marking the transition to quantum electrodynamics. Electric and magnetic field operators are given for the case of a non-vacuum background medium without charges or currents present. The Green's tensor $\boldsymbol{G}(\mathbf{r}, \mathbf{r}', \omega)$ is introduced as a solution to the homogeneous Helmholtz equation. In the following section 2.2, the nature of the dispersion forces Casimir-Polder and van der Waals force is discussed along with a variety of applications and intriguing properties. The last section 2.3 provides an overview over the basics of Rydberg physics. While research has been most extensive in the field of atomic Rydberg physics, other Rydberg systems such as excitons and molecules are covered as well.

2.1. Macroscopic quantum electrodynamics

The subject of classical electrodynamics is part of every undergraduate physics curriculum and hence a plethora of literature can be consulted for this chapter of fundamental physics. Among the most prominent works is the extensive book by Jackson [30]. Because of the great number of texts it is convenient to choose a source that is explicitly tailored to interatomic dispersion forces that are subject of this thesis like the field's comprehensive books by Buhmann [13]. Therefore, this section follows the detailed introductory chapters of [13; 14] that include the field quantization and highlights the most relevant aspects. A more condensed approach is provided for example by Vogel and Welsch [11].

2.1.1. Classical electrodynamics in free space

The governing equations of classical electrodynamics are Maxwell's equations for the electric field $\mathbf{E}$ and the induction field $\mathbf{B}$ which in the absence of charges and currents are given by

$$\nabla \cdot \mathbf{E}(\mathbf{r}, t) = 0, \tag{2.1}$$

$$\nabla \cdot \mathbf{B}(\mathbf{r}, t) = 0, \tag{2.2}$$

$$\nabla \times \mathbf{E}(\mathbf{r}, t) = -\dot{\mathbf{B}}(\mathbf{r}, , t), \tag{2.3}$$

$$\nabla \times \mathbf{B}(\mathbf{r}, t) = \frac{1}{c^2}\dot{\mathbf{E}}(\mathbf{r}, t). \tag{2.4}$$

In order to solve these equations one often introduces the scalar potential $\phi(\mathbf{r}, t)$ and the vector potential $\mathbf{A}(\mathbf{r}, t)$ that are related to $\mathbf{E}$ and $\mathbf{B}$ via

$$\mathbf{B}(\mathbf{r}, t) = \nabla \times \mathbf{A}(\mathbf{r}, t), \tag{2.5}$$

$$\mathbf{E}(\mathbf{r}, t) = -\nabla\phi(\mathbf{r}, t) - \dot{\mathbf{A}}(\mathbf{r}, t). \tag{2.6}$$

The choice of these potentials guarantees the validity of equations (2.2) and (2.3). While ϕ and $\mathbf{A}$ are not physical quantities in the sense that they are themselves measurable, their use provides mathematical means to solve Maxwell's equations (2.1) to (2.4). When one inserts the expressions of equations (2.6) and (2.5) into (2.1) and (2.4), one arrives at

$$-\Delta\phi(\mathbf{r}, t) - \nabla \cdot \dot{\mathbf{A}}(\mathbf{r}, t) = 0, \tag{2.7}$$

$$\frac{1}{c^2}\nabla\dot{\phi}(\mathbf{r}, t) + \frac{1}{c^2}\ddot{\mathbf{A}}(\mathbf{r}, t) - \Delta\mathbf{A}(\mathbf{r}, t) + \nabla(\nabla \cdot \mathbf{A}(\mathbf{r}, t)) = \mathbf{0}. \tag{2.8}$$

The potentials ϕ and $\mathbf{A}$ are subject to gauge freedom which allows one to, for example, set

$$\nabla \cdot \mathbf{A}(\mathbf{r}, t) = 0 \tag{2.9}$$

which is known as the Coulomb gauge. The Coulomb gauge simplifies equations (2.7) and (2.8) significantly but is not Lorentz covariant. This is disadvantageous for relativistic problems where for this reason the Lorentz covariant Lorenz gauge is often used,

$$\nabla \cdot \mathbf{A}(\mathbf{r}, t) + \frac{1}{c^2}\frac{\partial^2}{\partial t^2}\phi(\mathbf{r}, t) = 0. \tag{2.10}$$

However, in this thesis the calculations remain non-relativistic and, thus, the Coulomb gauge will be used in the following. Furthermore, every vector field can be decomposed into longitu-

dinal and transverse components according to

$$\mathbf{E}(\mathbf{r},t) = \mathbf{E}^{\parallel}(\mathbf{r},t) + \mathbf{E}^{\perp}(\mathbf{r},t). \tag{2.11}$$

In the chosen gauge, these components are related to the scalar and vector potential by

$$\mathbf{E}^{\parallel}(\mathbf{r},t) = -\nabla\phi(\mathbf{r},t), \tag{2.12}$$

$$\mathbf{E}^{\perp}(\mathbf{r},t) = -\dot{\mathbf{A}}(\mathbf{r},t). \tag{2.13}$$

In Coulomb gauge, the partial differential equations (2.7) and (2.8) decouple leaving a Laplace equation for the scalar potential ϕ and a wave equation for the vector potential $\mathbf{A}$,

$$\Delta\phi(\mathbf{r},t) = 0, \tag{2.14}$$

$$\frac{1}{c^2}\ddot{\mathbf{A}}(\mathbf{r},t) - \Delta\mathbf{A}(\mathbf{r},t) = \mathbf{0}. \tag{2.15}$$

In absence of particles, the solutions to equations (2.14) and (2.15) are

$$\phi(\mathbf{r},t) = 0, \tag{2.16}$$

$$\mathbf{A}(\mathbf{r},t) = \mathbf{A}_0 e^{\mathrm{i}(\mathbf{k}\cdot\mathbf{r}-\omega t)}. \tag{2.17}$$

Equation (2.17) describes a plain wave with the wave number $|\mathbf{k}| = \omega/c$ and frequency ω. Inserting this into equations (2.6) and (2.5) results in the respective electric and induction fields.

2.1.2. Classical electrodynamics with charged particles

In the presence of point particles with mass m_i and charge q_i at positions $\mathbf{r}_i$, there is a non-vanishing charge density

$$\rho(\mathbf{r},t) = \sum_i q_i \delta(\mathbf{r}-\mathbf{r}_i) \tag{2.18}$$

and current density

$$\mathbf{j}(\mathbf{r},t) = \sum_i q_i \dot{\mathbf{r}}_i \delta(\mathbf{r}-\mathbf{r}_i). \tag{2.19}$$

They are linked by the continuity equation

$$\dot{\rho} + \nabla \cdot \mathbf{j} = 0 \tag{2.20}$$

that states that temporal changes of ρ are equivalent to the sources and sinks of the current density $\mathbf{j}$ and constitutes a conservation law. The presence of charged particles leads to inhomogeneities in the Maxwell's equations (2.1) and (2.4),

$$\varepsilon_0 \nabla \cdot \mathbf{E}(\mathbf{r}, t) = \rho(\mathbf{r}, t), \tag{2.21}$$

$$\nabla \times \mathbf{B}(\mathbf{r}, t) = \frac{1}{c^2}\dot{\mathbf{E}}(\mathbf{r}, t) + \mu_0 \mathbf{j}(\mathbf{r}, t). \tag{2.22}$$

The vacuum speed of light is $c = 1/\sqrt{\mu_0 \varepsilon_0}$. Again, one can make use of the scalar potential ϕ and the vector potential $\mathbf{A}$. Using the Coulomb gauge equation (2.9) one finds a Poisson equation for ϕ,

$$\Delta\phi(\mathbf{r}, t) = -\frac{\rho(\mathbf{r}, t)}{\varepsilon_0}, \tag{2.23}$$

that is solved by the Coulomb potential of point charges,

$$\phi(\mathbf{r}) = \sum_i \frac{q_i}{4\pi\varepsilon_0 |\mathbf{r} - \mathbf{r}_i|}. \tag{2.24}$$

With the help of the continuity equation (2.20) and the inhomogeneous Maxwell equation (2.22), one can derive an inhomogeneous wave equation for vector potential $\mathbf{A}$,

$$\frac{1}{c^2}\ddot{\mathbf{A}}(\mathbf{r}, t) - \Delta\mathbf{A}(\mathbf{r}, t) = \mu_0 \mathbf{j}^{\perp}(\mathbf{r}, t). \tag{2.25}$$

The charged particles naturally obey Newton's equation of motion driven by the Lorentz force,

$$m_i \ddot{\mathbf{r}}_i = q_i \left[\mathbf{E}(\mathbf{r}_i) + \dot{\mathbf{r}}_i \times \mathbf{B}(\mathbf{r}_i)\right], \tag{2.26}$$

that can be rewritten in terms of the vector potential $\mathbf{A}$ and the Coulomb potential (2.24) as

$$m_i \ddot{\mathbf{r}}_i = q_i \left[\sum_{j \neq i} \frac{q_j (\mathbf{r}_i - \mathbf{r}_j)}{4\pi\varepsilon_0 |(\mathbf{r}_i - \mathbf{r}_j)|^3} - \dot{\mathbf{A}}(\mathbf{r}_i) + \dot{\mathbf{r}}_i \times (\nabla \times \mathbf{A}(\mathbf{r}_i))\right]. \tag{2.27}$$

The non-relativistic Lagrangian $L = T - V$ can then be written as

$$L = \frac{1}{2}\sum_i m_i \dot{\mathbf{r}}_i^2 - \sum_{i\neq j} \frac{q_i q_j}{8\pi\varepsilon_0 |\mathbf{r}_i - \mathbf{r}_j|} + \frac{1}{2}\int \mathrm{d}^3 r \left[\varepsilon_0 \dot{\mathbf{A}}^2 - \frac{1}{\mu_0}(\nabla \times \mathbf{A})^2\right] + \int \mathrm{d}^3 r\, \mathbf{j}\cdot\mathbf{A} \tag{2.28}$$

where the last term represents the particles' interaction with the transverse electromagnetic field. This representation is known as the minimal coupling scheme. We calculate the Lagrange equations,

$$\frac{\delta L}{\delta \mathbf{A}} = \frac{\mathrm{d}}{\mathrm{d}t}\frac{\delta L}{\delta \dot{\mathbf{A}}}, \tag{2.29}$$

$$\frac{\partial L}{\partial \mathbf{r}_i} = \frac{\mathrm{d}}{\mathrm{d}t}\frac{\partial L}{\partial \dot{\mathbf{r}}_i} \tag{2.30}$$

and assert that equation (2.29) leads to the Helmholtz equation (2.25) for the vector potential $\mathbf{A}$ and the Lagrange equations (2.30) for the particle positions $\mathbf{r}_i$ are indeed equivalent to the Newtonian equation of motion equation (2.27). The associated canonical momenta for vector potential $\mathbf{A}$ and particle position $\mathbf{r}_i$ are

$$\mathbf{\Pi} = \frac{\partial L}{\partial \dot{\mathbf{A}}} = \varepsilon_0 \dot{\mathbf{A}} = -\varepsilon_0 \mathbf{E}^{\perp}, \tag{2.31}$$

$$\mathbf{p}_i = \frac{\partial L}{\partial \dot{\mathbf{r}}_i} = m_i \mathbf{r}_i + q_i \mathbf{A}(\mathbf{r}_i), \tag{2.32}$$

respectively. With this, one can compute the Hamiltonian via a Legendre transformation as

$$H = \sum_i \mathbf{p}_i \cdot \dot{\mathbf{r}}_i + \int \mathrm{d}^3 r\, \mathbf{\Pi}\cdot\dot{\mathbf{A}} - L. \tag{2.33}$$

Expressed with the canonical momenta $\mathbf{p}_i$ and $\mathbf{\Pi}$, one arrives at

$$H = \sum_i \frac{(\mathbf{p}_i - q_i\mathbf{A}(\mathbf{r}_i))^2}{2m_i} + \sum_{i\neq j}\frac{q_i q_j}{8\pi\varepsilon_0|\mathbf{r}_i - \mathbf{r}_j|} + \frac{1}{2}\int \mathrm{d}^3 r \left(\frac{\mathbf{\Pi}^2}{\varepsilon_0} + \frac{(\nabla\times\mathbf{A})^2}{\mu_0}\right). \tag{2.34}$$

Here, one can substitute the expression (2.5) for the curl of the vector potential and equations (2.31) and (2.32) for the conjugate momenta $\mathbf{\Pi}$ and $\mathbf{p}_i$, respectively:

$$H = \frac{1}{2}\sum_i m_i \dot{\mathbf{r}}_i^2 + \sum_{i\neq j}\frac{q_i q_j}{8\pi\varepsilon_0|\mathbf{r}_i - \mathbf{r}_j|} + \frac{1}{2}\int_0^\infty \mathrm{d}^3 r \left(\varepsilon_0 (\mathbf{E}^{\perp})^2 + \frac{\mathbf{B}^2}{\mu_0}\right) \tag{2.35}$$

$$= \frac{1}{2}\sum_i m_i \dot{\mathbf{r}}_i^2 + \frac{1}{2}\int \mathrm{d}^3 r \left(\varepsilon_0 \mathbf{E}^2 + \frac{\mathbf{B}^2}{\mu_0}\right). \tag{2.36}$$

For this last step, the relations between the Coulomb term and the longitudinal electric field were used,

$$\sum_{i\neq j}\frac{q_i q_j}{8\pi\varepsilon_0|\mathbf{r}_i-\mathbf{r}_j|}=\frac{1}{2}\int \mathrm{d}^3r\,\varepsilon_0\left(\mathbf{E}^{\parallel}\right)^2. \tag{2.37}$$

The Hamiltonian (2.36) consists of the particles' kinetic energy and the energy of the electromagnetic field and, hence, yields the total energy of the system. As a prerequisite for the field quantization, it is convenient to introduce Poisson brackets $\{f,g\}$ as

$$\{f,g\}=\sum_i\frac{\partial f}{\partial\mathbf{r}_i}\frac{\partial g}{\partial\mathbf{p}_i}-\frac{\partial f}{\partial\mathbf{p}_i}\frac{\partial g}{\partial\mathbf{r}_i}+\int\mathrm{d}^3r\left(\frac{\delta f}{\delta\mathbf{A}}\frac{\delta g}{\delta\mathbf{\Pi}}-\frac{\delta f}{\delta\mathbf{\Pi}}\frac{\delta g}{\delta\mathbf{A}}\right). \tag{2.38}$$

The fundamental Poisson brackets for the particle and the field are

$$\{\mathbf{r}_i,\mathbf{r}_j\}=\{\mathbf{p}_i,\mathbf{p}_j\}=\mathbf{0}, \tag{2.39}$$
$$\{\mathbf{r}_i,\mathbf{p}_j\}=\delta_{ij}\mathbf{I}, \tag{2.40}$$
$$\{\mathbf{A}(\mathbf{r}),\mathbf{A}(\mathbf{r}')\}=\{\mathbf{\Pi}(\mathbf{r}),\mathbf{\Pi}(\mathbf{r}')\}=\mathbf{0}, \tag{2.41}$$
$$\{\mathbf{A}(\mathbf{r}),\mathbf{\Pi}(\mathbf{r}')\}=\boldsymbol{\delta}^{\perp}(\mathbf{r}-\mathbf{r}'), \tag{2.42}$$

while the classical equations of motion can be expressed as

$$\dot{\mathbf{r}}_i=\{\mathbf{p}_i,H\}, \tag{2.43}$$
$$\dot{\mathbf{p}}_i=\{\mathbf{r}_i,H\}, \tag{2.44}$$
$$\dot{\mathbf{A}}=\{\mathbf{A},H\}, \tag{2.45}$$
$$\dot{\mathbf{\Pi}}=\{\mathbf{\Pi},H\}. \tag{2.46}$$

This way, the Hamilton equations of motions can be written in a very compact form.

2.1.3. Classical electrodynamics in media

The vast amount of particles in a macroscopic object renders it impossible to solve the equations of motions for every particle separately. Thus, for bulk media, a collective theory has to be used. One starts by replacing the charge density ρ and current density $\mathbf{j}$ by their respective

internal counterparts $\rho_{\rm in}$ and $\mathbf{j}_{\rm in}$. The inhomogeneous Maxwell's equations become

$$\varepsilon_0 \nabla \cdot \mathbf{E}(\mathbf{r},t) = \rho_{\rm in}(\mathbf{r},t), \tag{2.47}$$

$$\nabla \times \mathbf{B}(\mathbf{r},t) = \frac{1}{c^2}\dot{\mathbf{E}}(\mathbf{r},t) + \mu_0 \mathbf{j}_{\rm in}(\mathbf{r},t). \tag{2.48}$$

Now, one may introduce polarization $\mathbf{P}$ and magnetization $\mathbf{M}$ according to

$$\rho_{\rm in}(\mathbf{r},t) = -\nabla \cdot \mathbf{P}(\mathbf{r},t), \tag{2.49}$$

$$\mathbf{j}_{\rm in}(\mathbf{r},t) = \dot{\mathbf{P}}(\mathbf{r},t) + \nabla \times \mathbf{M}(\mathbf{r},t), \tag{2.50}$$

as well as electric excitation or electric displacement field $\mathbf{D}$ and magnetic excitation or magnetic field $\mathbf{H}$ according to

$$\mathbf{D}(\mathbf{r},t) = \varepsilon_0 \mathbf{E}(\mathbf{r},t) + \mathbf{P}(\mathbf{r},t), \tag{2.51}$$

$$\mathbf{H}(\mathbf{r},t) = \frac{1}{\mu_0}\mathbf{B}(\mathbf{r},t) - \mathbf{M}(\mathbf{r},t). \tag{2.52}$$

Using these expressions, the equations (2.47) and (2.48) may be rewritten as

$$\nabla \cdot \mathbf{D}(\mathbf{r},t) = 0, \tag{2.53}$$

$$\nabla \times \mathbf{H}(\mathbf{r},t) - \dot{\mathbf{D}}(\mathbf{r},t) = \mathbf{0}. \tag{2.54}$$

In order to move to a collective description, constitutive relations for polarization $\mathbf{P}$ and magnetization $\mathbf{M}$ have to be found. It is convenient to express $\mathbf{P}$ and $\mathbf{M}$ as an equilibrium state that is perturbed by an electromagnetic field resulting in a linear response function. This is a good assumption as long as $\mathbf{E}$ and $\mathbf{B}$ do not become too strong. In case of the the response function being local, i.e. independent of effects in the surrounding medium, and isotropic, the constitutive relations can be written as

$$\mathbf{P}(\mathbf{r},t) = \varepsilon_0 \int_{-\infty}^{\infty} \mathrm{d}\tau\, \chi(\mathbf{r},\tau)\mathbf{E}(\mathbf{r},t-\tau) + \mathbf{P}_{\rm N}(\mathbf{r},t), \tag{2.55}$$

$$\mathbf{M}(\mathbf{r},t) = \frac{1}{\mu_0} \int_{-\infty}^{\infty} \mathrm{d}\tau\, \zeta(\mathbf{r},\tau)\mathbf{B}(\mathbf{r},t-\tau) + \mathbf{M}_{\rm N}(\mathbf{r},t). \tag{2.56}$$

The response functions $\chi(\mathbf{r},\tau)$ and $\zeta(\mathbf{r},\tau)$ fulfill the causality requirement, i.e. they vanish for times $\tau < 0$. Additionally, the noise polarization $\mathbf{P}_{\rm N}$ and the noise magnetization $\mathbf{M}_{\rm N}$ were introduced. They account for the statistical fluctuations occurring in any large atomic ensemble. Their classical averages vanish, $\langle \mathbf{P}_{\rm N} \rangle_{\rm cl} = \langle \mathbf{M}_{\rm N} \rangle_{\rm cl} = \mathbf{0}$.

The Fourier transformed response functions $\chi(\mathbf{r},\omega)$ and $\zeta(\mathbf{r},\omega)$ are connected to the fluctuations of $\mathbf{P}_\mathrm{N}(\mathbf{r},\omega)$ and $\mathbf{M}_\mathrm{N}(\mathbf{r},\omega)$ by the fluctuation-dissipation theorem [31],

$$\langle \Delta\mathbf{P}_\mathrm{N}(\mathbf{r},\omega)\Delta\mathbf{P}_\mathrm{N}^*(\mathbf{r}',\omega')\rangle_\mathrm{cl} = \frac{k_B T}{\pi\omega}\varepsilon_0 \mathrm{Im}\chi(\mathbf{r},\omega)\boldsymbol{\delta}(\mathbf{r}-\mathbf{r}')\delta(\omega-\omega') \tag{2.57}$$

$$\langle \Delta\mathbf{M}_\mathrm{N}(\mathbf{r},\omega)\Delta\mathbf{M}_\mathrm{N}^*(\mathbf{r}',\omega')\rangle_\mathrm{cl} = \frac{k_B T}{\pi\omega}\frac{\mathrm{Im}\zeta(\mathbf{r},\omega)}{\mu_0}\boldsymbol{\delta}(\mathbf{r}-\mathbf{r}')\delta(\omega-\omega'). \tag{2.58}$$

The fluctuations $\Delta\mathbf{P}_\mathrm{N}$ and $\Delta\mathbf{M}_\mathrm{N}$ are proportional to the imaginary part of the medium's response function. As the response function's imaginary part determines whether a given material is absorbing or amplifying, equations (2.57) and (2.58) demonstrate the link between the absorption of a material and the corresponding fluctuations. With relative permittivity $\varepsilon(\mathbf{r},\omega) = 1+\chi(\mathbf{r},\omega)$ and relative susceptibility $\mu(\mathbf{r},\omega) = \frac{1}{1-\zeta(\mathbf{r},\omega)}$, Maxwell's equations and the constitutive relations inside a medium with no currents or charges present are in Fourier space

$$\nabla\cdot\mathbf{D}(\mathbf{r},\omega) = 0, \tag{2.59}$$

$$\nabla\cdot\mathbf{B}(\mathbf{r},\omega) = 0, \tag{2.60}$$

$$\nabla\times\mathbf{D}(\mathbf{r},\omega) - \mathrm{i}\omega\mathbf{B}(\mathbf{r},\omega) = \mathbf{0}, \tag{2.61}$$

$$\nabla\times\mathbf{H}(\mathbf{r},\omega) + \mathrm{i}\omega\mathbf{D}(\mathbf{r},\omega) = \mathbf{0}, \tag{2.62}$$

$$\mathbf{D}(\mathbf{r},\omega) = \varepsilon_0\varepsilon\mathbf{E}(\mathbf{r},\omega) + \mathbf{P}_\mathrm{N}(\mathbf{r},\omega), \tag{2.63}$$

$$\mathbf{H}(\mathbf{r},\omega) = \frac{1}{\mu_0\mu}\mathbf{B}(\mathbf{r},\omega) - \mathbf{M}_N(\mathbf{r},\omega). \tag{2.64}$$

These equation are the foundation of more advanced electrodynamics and can be generalized to include free charges and currents inside the medium. However, this is beyond the scope of the introductory chapter of this thesis. Further considerations can be found in the aforementioned literature, with [13] focusing on the application in the field of dispersion forces and [30] giving a detailed analysis of the whole field of classical electrodynamics.

2.1.4. Field quantization in free space

Starting from the Poisson brackets (2.39) and (2.40) for the classical quantities f and g, one simply replaces f and g by the quantum mechanical operators $\hat{f}$ and $\hat{g}$ as well as the classical Poisson brackets by the quantum mechanical commutators, $\{f,g\} \to \frac{1}{\mathrm{i}\hbar}\left[\hat{f},\hat{g}\right]$ with the reduced

Planck's constant $\hbar$. The commutators therefore read

$$[\hat{\mathbf{r}}_i, \hat{\mathbf{r}}_j] = [\hat{\mathbf{p}}_i, \hat{\mathbf{p}}_j] = \mathbf{0}, \tag{2.65}$$

$$[\hat{\mathbf{r}}_i, \hat{\mathbf{p}}_j] = \mathrm{i}\hbar\delta_{ij}\mathbf{I}, \tag{2.66}$$

$$\left[\hat{\mathbf{A}}(\mathbf{r}), \hat{\mathbf{A}}(\mathbf{r}')\right] = \left[\hat{\mathbf{\Pi}}(\mathbf{r}), \hat{\mathbf{\Pi}}(\mathbf{r}')\right] = \mathbf{0}, \tag{2.67}$$

$$\left[\hat{\mathbf{A}}(\mathbf{r}), \hat{\mathbf{\Pi}}(\mathbf{r}')\right] = \mathrm{i}\hbar\boldsymbol{\delta}^{\perp}(\mathbf{r}-\mathbf{r}'). \tag{2.68}$$

In Coulomb gauge, the operator valued electric and magnetic (induction) field are

$$\hat{\mathbf{E}} = \hat{\mathbf{E}}^{\perp} = -\frac{1}{\varepsilon_0}\hat{\mathbf{\Pi}}, \tag{2.69}$$

$$\hat{\mathbf{B}} = \nabla \times \hat{\mathbf{A}} \tag{2.70}$$

with the commutator relations

$$\left[\hat{\mathbf{E}}(\mathbf{r}), \hat{\mathbf{E}}(\mathbf{r}')\right] = \left[\hat{\mathbf{B}}(\mathbf{r}), \hat{\mathbf{B}}(\mathbf{r}')\right] = \mathbf{0}, \tag{2.71}$$

$$\left[\hat{\mathbf{E}}(\mathbf{r}), \hat{\mathbf{B}}(\mathbf{r}')\right] = \frac{\mathrm{i}\hbar}{\varepsilon_0}\nabla \times \boldsymbol{\delta}(\mathbf{r}-\mathbf{r}'). \tag{2.72}$$

Finally, one can define the Hamiltonian of the electromagnetic field as

$$\hat{H} = \frac{1}{2}\int \mathrm{d}^3 r \left(\varepsilon_0 \hat{\mathbf{E}}^2 + \frac{\hat{\mathbf{B}}^2}{\mu_0}\right), \tag{2.73}$$

allowing one to express Heisenberg equations of motion of the form

$$\dot{\hat{f}} = \frac{1}{\mathrm{i}\hbar}\left[\hat{f}, \hat{H}\right]. \tag{2.74}$$

2.1.5. Field quantization in media

For field quantization in a medium, the approach via the Hamilton formalism is not as easily done as in free space. Therefore, a quantum theory of electromagnetic fields in media is guided by the principle that it has to resemble the classical Maxwell equations and that the fluctuations of the electromagnetic field have to obey the fluctuation-dissipation theorem (2.57) and (2.58). Additionally, a distinction between electric and magnetic fields and excitations has to be made. While the fields must obey the same commutation relations in a medium and free space, the excitations carry contributions from the medium's polarization and magnetization. One way to

achieve this is by introducing bosonic creation and annihilation operators $\hat{\mathbf{f}}^\dagger(\mathbf{r},\omega)$ and $\hat{\mathbf{f}}(\mathbf{r},\omega)$. They are subject to the respective bosonic commutation rules,

$$\left[\hat{\mathbf{f}}_\lambda(\mathbf{r},\omega),\hat{\mathbf{f}}_{\lambda'}(\mathbf{r}',\omega')\right]=\left[\hat{\mathbf{f}}^\dagger_\lambda(\mathbf{r},\omega),\hat{\mathbf{f}}^\dagger_{\lambda'}(\mathbf{r}',\omega')\right]=\mathbf{0}, \tag{2.75}$$

$$\left[\hat{\mathbf{f}}_\lambda(\mathbf{r},\omega),\hat{\mathbf{f}}^\dagger_{\lambda'}(\mathbf{r}',\omega')\right]=\delta_{\lambda\lambda'}\delta(\omega-\omega')\boldsymbol{\delta}(\mathbf{r}-\mathbf{r}'), \tag{2.76}$$

with the subscript $\lambda = e,m$ indicating the electric or magnetic field component. As it was described before in section 2.1.3, without charges or currents present, electrodynamics are driven by the noise polarization $\hat{\mathbf{P}}_N(\mathbf{r},\omega)$ and noise magnetization $\hat{\mathbf{M}}_N(\mathbf{r},\omega)$. One can write $\hat{\mathbf{P}}_N(\mathbf{r},\omega)$ and $\hat{\mathbf{M}}_N(\mathbf{r},\omega)$ using the operators $\hat{\mathbf{f}}^{(\dagger)}$ as

$$\hat{\mathbf{P}}_N(\mathbf{r},\omega)=\mathrm{i}\sqrt{\frac{\hbar\varepsilon_0}{\pi}\mathrm{Im}\varepsilon(\mathbf{r},\omega)}\hat{\mathbf{f}}_e(\mathbf{r},\omega), \tag{2.77}$$

$$\hat{\mathbf{M}}_N(\mathbf{r},\omega)=\sqrt{\frac{\hbar}{\pi\mu_0}\frac{\mathrm{Im}\mu(\mathbf{r},\omega)}{|\mu(\mathbf{r},\omega)|^2}}\hat{\mathbf{f}}_m(\mathbf{r},\omega). \tag{2.78}$$

The $\hat{\mathbf{P}}_N(\mathbf{r},\omega)$ and $\hat{\mathbf{M}}_N(\mathbf{r},\omega)$ are part of the constitutive equations

$$\hat{\mathbf{D}}(\mathbf{r},\omega)=\varepsilon_0\varepsilon\hat{\mathbf{E}}(\mathbf{r},\omega)+\hat{\mathbf{P}}(\mathbf{r},\omega), \tag{2.79}$$

$$\hat{\mathbf{H}}(\mathbf{r},\omega)=\frac{1}{\mu_0\mu}\hat{\mathbf{B}}(\mathbf{r},\omega)-\hat{\mathbf{M}}_N(\mathbf{r},\omega). \tag{2.80}$$

Maxwell's equation are fulfilled by the field operators,

$$\nabla\cdot\hat{\mathbf{D}}(\mathbf{r},\omega)=0, \tag{2.81}$$

$$\nabla\cdot\hat{\mathbf{B}}(\mathbf{r},\omega)=0, \tag{2.82}$$

$$\nabla\times\hat{\mathbf{E}}(\mathbf{r},\omega)-\mathrm{i}\omega\hat{\mathbf{B}}(\mathbf{r},\omega)=\mathbf{0}, \tag{2.83}$$

$$\nabla\times\hat{\mathbf{H}}(\mathbf{r},\omega)+\mathrm{i}\omega\hat{\mathbf{D}}(\mathbf{r},\omega)=\mathbf{0}, \tag{2.84}$$

given here for the case of no present charged particles. In vacuum, the expectation values of the noise polarization and magnetization are vanishing, $\langle\hat{\mathbf{P}}_N(\mathbf{r},\omega)\rangle=\mathbf{0}$ and $\langle\hat{\mathbf{M}}_N(\mathbf{r},\omega)\rangle=\mathbf{0}$.

However, via the fluctuation-dissipation theorem the average fluctuations are given by

$$\frac{1}{2}\langle\Delta\hat{\mathbf{P}}_N(\mathbf{r},\omega)\Delta\hat{\mathbf{P}}_N^\dagger(\mathbf{r}',\omega')+\Delta\hat{\mathbf{P}}_N^\dagger(\mathbf{r},\omega)\Delta\hat{\mathbf{P}}_N(\mathbf{r}',\omega')\rangle=\frac{\hbar}{2\pi}\varepsilon_0\mathrm{Im}\chi(\mathbf{r},\omega)\boldsymbol{\delta}(\mathbf{r}-\mathbf{r}')\delta(\omega-\omega'), \tag{2.85}$$

$$\frac{1}{2}\langle\Delta\hat{\mathbf{M}}_N(\mathbf{r},\omega)\Delta\hat{\mathbf{M}}_N^\dagger(\mathbf{r}',\omega')+\Delta\hat{\mathbf{M}}_N^\dagger(\mathbf{r},\omega)\Delta\hat{\mathbf{M}}_N(\mathbf{r}',\omega')\rangle=\frac{\hbar}{2\pi}\frac{\mathrm{Im}\zeta(\mathbf{r},\omega)}{\mu_0}\boldsymbol{\delta}(\mathbf{r}-\mathbf{r}')\delta(\omega-\omega') \tag{2.86}$$

with the electric susceptibility χ and the magnetic susceptibility ζ. The quantum noise magnetization and polarization are linked to the noise charge density $\hat{\rho}_N(\mathbf{r},\omega)$ and noise current density $\hat{\mathbf{j}}_N(\mathbf{r},\omega)$ via

$$\hat{\rho}_N=-\nabla\cdot\hat{\mathbf{P}}_N, \tag{2.87}$$

$$\hat{\mathbf{j}}_N=-\mathrm{i}\omega\hat{\mathbf{P}}_N+\nabla\times\hat{\mathbf{M}}_N, \tag{2.88}$$

which in turn are subject to the continuity equation

$$-\mathrm{i}\omega\hat{\rho}_N+\nabla\cdot\hat{\mathbf{j}}_N=0. \tag{2.89}$$

Combining the constitutive relations (2.79) and (2.80) with the quantum Maxwell's equations (2.81) to (2.81), one can derive an inhomogeneous Helmholtz equation for the electric field operator,

$$\left(\nabla\times\frac{1}{\mu}\nabla\times-\frac{\omega^2}{c^2}\right)\hat{\mathbf{E}}(\mathbf{r},\omega)=\mathrm{i}\mu_0\omega\hat{\mathbf{j}}(\mathbf{r},\omega). \tag{2.90}$$

The classical Green's tensor $\boldsymbol{G}(\mathbf{r},\mathbf{r}'\omega)$ is the solution to the homogeneous part of equation (2.90),

$$\left(\nabla\times\frac{1}{\mu}\nabla\times-\frac{\omega^2}{c^2}\right)\boldsymbol{G}(\mathbf{r},\mathbf{r}',\omega)=\boldsymbol{\delta}(\mathbf{r}-\mathbf{r}'). \tag{2.91}$$

Thus, a formal solution to 2.90 can be found using $\boldsymbol{G}(\mathbf{r},\mathbf{r}',\omega)$ as

$$\hat{\mathbf{E}}(\mathbf{r},\omega)=\mathrm{i}\mu_0\omega\int\mathrm{d}^3r'\,\boldsymbol{G}(\mathbf{r},\mathbf{r}',\omega)\cdot\hat{\mathbf{j}}_N(\mathbf{r}',\omega). \tag{2.92}$$

One can rewrite the noise current density (2.88) with the noise polarization (2.77) and magnetization (2.78) to get

$$\begin{aligned}\hat{\mathbf{E}}(\mathbf{r},\omega) = \mathrm{i}\mu_0\omega \int \mathrm{d}^3r'\, \boldsymbol{G}(\mathbf{r},\mathbf{r}',\omega)\cdot \Bigg(&\omega\sqrt{\frac{\hbar\varepsilon_0}{\pi}\mathrm{Im}\varepsilon(\mathbf{r}',\omega)}\hat{\mathbf{f}}_e(\mathbf{r}',\omega) \\ &+ \nabla'\times\sqrt{\frac{\hbar}{\pi\mu_0}\frac{\mathrm{Im}\mu(\mathbf{r}',\omega)}{|\mu(\mathbf{r}',\omega)|^2}}\hat{\mathbf{f}}_m(\mathbf{r}',\omega)\Bigg)\end{aligned} \tag{2.93}$$

The last term can be rearranged according to

$$\begin{aligned}\int \mathrm{d}^3r'\, \boldsymbol{G}(\mathbf{r},\mathbf{r}')\cdot\left(\nabla'\times\hat{\mathbf{f}}(\mathbf{r}')\right) &= \int \mathrm{d}^3r'\,\left(\hat{\mathbf{f}}(\mathbf{r}')\cdot(\nabla\times\boldsymbol{G}(\mathbf{r},\mathbf{r}')) - \nabla\cdot(\boldsymbol{G}(\mathbf{r},\mathbf{r}')\times\hat{\mathbf{f}}(\mathbf{r}))\right) \\ &= \int \mathrm{d}^3r'\,(\nabla\times\boldsymbol{G}(\mathbf{r},\mathbf{r}'))^T\cdot\hat{\mathbf{f}}(\mathbf{r}') - \underbrace{\oint \mathrm{d}S\,\boldsymbol{G}(\mathbf{r},\mathbf{r}')\times\hat{\mathbf{f}}(\mathbf{r})}_{=0}.\end{aligned} \tag{2.94}$$

The surface integral vanishes because $\lim_{|\mathbf{r}-\mathbf{r}'|\to\infty}\boldsymbol{G}(\mathbf{r},\mathbf{r}',\omega)=\mathbf{0}$. This allows one to shorten the expression (2.93) to

$$\hat{\mathbf{E}}(\mathbf{r},\omega) = \sum_{\lambda=e,m}\int \mathrm{d}^3r'\,\boldsymbol{G}_\lambda(\mathbf{r},\mathbf{r}',\omega)\cdot\hat{\mathbf{f}}_\lambda(\mathbf{r}',\omega) \tag{2.95}$$

with the coefficients

$$\boldsymbol{G}_e(\mathbf{r},\mathbf{r}',\omega) = \mathrm{i}\frac{\omega^2}{c^2}\sqrt{\frac{\hbar}{\pi\varepsilon_0}\mathrm{Im}\varepsilon(\mathbf{r}',\omega)}\boldsymbol{G}(\mathbf{r},\mathbf{r}',\omega), \tag{2.96}$$

$$\boldsymbol{G}_m(\mathbf{r},\mathbf{r}',\omega) = \mathrm{i}\frac{\omega}{c}\sqrt{\frac{\hbar}{\pi\varepsilon_0}\frac{\mathrm{Im}\mu(\mathbf{r}',\omega)}{|\mu(\mathbf{r}',\omega)|^2}}\,(\nabla'\times\boldsymbol{G}(\mathbf{r},\mathbf{r}',\omega)^T\,. \tag{2.97}$$

The full electric field at position $\mathbf{r}$ is given by

$$\hat{\mathbf{E}}(\mathbf{r}) = \int_0^\infty \mathrm{d}\omega\,\left(\hat{\mathbf{E}}(\mathbf{r},\omega)+\hat{\mathbf{E}}^\dagger(\mathbf{r},\omega)\right). \tag{2.98}$$

A similar calculation can be carried out for the magnetic field

$$\hat{\mathbf{B}}(\mathbf{r}) = \int_0^\infty \mathrm{d}\omega\,\left(\hat{\mathbf{B}}(\mathbf{r},\omega)+\hat{\mathbf{B}}^\dagger(\mathbf{r},\omega)\right) \tag{2.99}$$

where

$$\hat{\mathbf{B}}(\mathbf{r},\omega) = -\frac{\mathrm{i}}{\omega}\sum_{\lambda=e,m}\int \mathrm{d}^3r'\,\nabla\times\boldsymbol{G}_\lambda(\mathbf{r},\mathbf{r}',\omega)\cdot\hat{\mathbf{f}}_\lambda(\mathbf{r}',\omega). \tag{2.100}$$

The electric and magnetic field follow the commutation relations

$$\left[\hat{\mathbf{E}}(\mathbf{r}),\hat{\mathbf{E}}(\mathbf{r}')\right] = \left[\hat{\mathbf{B}}(\mathbf{r}),\hat{\mathbf{B}}(\mathbf{r}')\right] = \mathbf{0}, \tag{2.101}$$

$$\left[\hat{\mathbf{E}}(\mathbf{r}),\hat{\mathbf{B}}(\mathbf{r}')\right] = \frac{\mathrm{i}\hbar}{\varepsilon_0}\nabla\times\boldsymbol{\delta}(\mathbf{r}-\mathbf{r}'). \tag{2.102}$$

In addition , the field Hamiltonian can then be determined using the $\hat{\mathbf{f}}^{(\dagger)}$ operators as

$$\hat{H}_F = \sum_{\lambda=e,m}\int_0^\infty \mathrm{d}\omega\int \mathrm{d}^3r\,\hbar\omega\hat{\mathbf{f}}^\dagger_\lambda(\mathbf{r},\omega)\cdot\hat{\mathbf{f}}_\lambda(\mathbf{r},\omega). \tag{2.103}$$

The eigenstates of the field Hamiltonian are the n-photon Fock states
$|\mathbf{1}_{\lambda_1}(\mathbf{r}_1,\omega_1),...,\mathbf{1}_{\lambda_n}(\mathbf{r}_n,\omega_n)\rangle$ with the eigenvalues being the sum of individual photon energies,

$$\hat{H}_F|\mathbf{1}_{\lambda_1}(\mathbf{r}_1,\omega_1),...,\mathbf{1}_{\lambda_n}(\mathbf{r}_n,\omega_n)\rangle = \hbar\left(\sum_i^n\omega_i\right)|\mathbf{1}_{\lambda_1}(\mathbf{r}_1,\omega_1),...,\mathbf{1}_{\lambda_n}(\mathbf{r}_n,\omega_n)\rangle. \tag{2.104}$$

The notation $|\mathbf{1}_{\lambda_i}(\mathbf{r}_i,\omega_i)\rangle$ describes one photon in mode λ_i at position $\mathbf{r}_i$ and frequency ω_i.

2.1.6. Atom-field interaction in multipolar coupling

In order to describe the interaction between an atom and the electromagnetic field, the minimal coupling scheme or the multipolar coupling scheme can be applied. The minimal coupling scheme was presented for the classical Lagrangian 2.28 and Hamiltonian (2.36). In this section the multipolar coupling scheme is presented briefly. One has to pay attention to the fact that perturbation theory using the minimal coupling scheme or the multipolar coupling scheme may yield different results. The choice of the correct coupling scheme depends on the concrete system under investigation.

The multipolar coupling scheme requires one to move to different atomic and field variables via a Power-Woolley-Zienau transformation $\hat{f}' = \hat{U}\hat{f}\hat{U}^\dagger$ with unitary operator $\hat{U} = \exp\left[\frac{i}{\hbar}\int \mathrm{d}^3r\,\hat{\mathbf{P}}_A\cdot\hat{\mathbf{A}}\right]$ [13]. While the vector potential $\hat{\mathbf{A}}$ and atomic position vector $\hat{\mathbf{r}}$ remain unchanged, the conjugate momenta $\hat{\mathbf{\Pi}}$ and $\hat{\mathbf{p}}$ are transformed. However, due to the fact the the Power-Woolley-Zienau transformation is unitary, all commutation relations stay the same. The

details of the transformation will be skipped and a brief overview of the transformed operators $\hat{f}'$ is presented. A more detailed review can be found in [13; 14]. The Hamiltonians of the field F, the atom A and the atom-field coupling respectively read

$$\hat{H}'_F = \sum_{\lambda=e,m} \int \mathrm{d}^3 r \int_0^\infty \mathrm{d}\omega\, \hbar\omega \hat{\mathbf{f}}'^{\dagger}_\lambda(\mathbf{r},\omega)\cdot\hat{\mathbf{f}}_\lambda(\mathbf{r},\omega), \tag{2.105}$$

$$\hat{H}'_A = \frac{\hat{\mathbf{p}}'^2_A}{2m_A} + \sum_n E'_n |n'\rangle\langle n'|, \tag{2.106}$$

$$\begin{aligned}\hat{H}'_{AF} = &-\hat{\mathbf{d}}'\cdot\hat{\mathbf{E}}'(\hat{\mathbf{r}}'_A) + \sum_{i\in A}\frac{q_i^2}{8m_A}\left[\hat{\mathbf{r}}'_i\times\hat{\mathbf{B}}(\hat{\mathbf{r}}'_A)\right]^2 \\ &+\frac{3}{8m_A}\left[\hat{\mathbf{d}}'\times\hat{\mathbf{B}}'(\hat{\mathbf{r}}'_A)\right]^2 - \frac{1}{m_A}\hat{\mathbf{d}}'\times\hat{\mathbf{p}}'_A\cdot\hat{\mathbf{B}}'(\hat{\mathbf{r}}'_A).\end{aligned} \tag{2.107}$$

Here, $\hat{\mathbf{d}}$ is the operator valued atomic dipole moment. The atom-field interaction Hamiltonian $\hat{H}'_{AF}$ is already given in the long-wavelength approximation assuming that the atom's wave function is much smaller than the wavelength of the electromagnetic field. Note that the primed variables in general do not equal the physical variables. Also the eigenstates $|n'\rangle$ of the internal atomic Hamiltonian $\hat{H}'_A$ are not the same n-photon Fock states as before and the field ground state $|\{0'\}\rangle$ of $\hat{H}'_F$ is not the the ground state of $\hat{H}_F$. However, the atomic position $\hat{\mathbf{r}}$ remains unchanged and therefore the atomic dipole transition moment $\hat{\mathbf{d}} = e\hat{\mathbf{r}}$ remains unchanged. One great advantage of the multipolar coupling scheme is that the atom-field Hamiltonian $\hat{H}'_{AF}$ is expressed in terms of actual fields and not in terms of the scalar and vector potential $\hat{\phi}$ and $\hat{\mathbf{A}}$, respectively [13].

The terms of the interaction Hamiltonian $\hat{H}'_{AF}$ can be interpreted as follows. The first and second term are the electric and magnetic dipole interaction, respectively. The terms three and four describe the diamagnetic interaction and the last term the Röntgen interaction related to the center-of-mass motion of the particle. For non-magnetic particles, the interaction Hamiltonian in the dipole approximation can be reduced to

$$\hat{H}'_{AF} = -\hat{\mathbf{d}}'\cdot\hat{\mathbf{E}}'(\hat{\mathbf{r}}'_A) - \frac{1}{m_A}\hat{\mathbf{d}}'\times\hat{\mathbf{p}}'_A\cdot\hat{\mathbf{B}}'(\hat{\mathbf{r}}'_A). \tag{2.108}$$

The second term vanishes for atoms at rest. The dipole approximation is valid for small interactions when higher order moments do not come into play and is even suitable for the description of photoionization of highly excited atoms [32]. Writing $\hat{H}_{AF}$ in the form (2.108) has the great advantage that it can be easily extended to higher order terms by a multipole extension, if it becomes necessary. As the commutations relations remain unchanged for the primed variables and $\hat{\mathbf{d}}$ is not affected by the Power-Woolley-Zienau transformation, it is still

possible to use equation (2.98) for the electric field and write the atomic dipole moment as $\hat{\mathbf{d}} = \sum_{ij} |i\rangle\langle j|\mathbf{d}_{ij}$ with atomic states $|i\rangle$, $|j\rangle$ omitting the primes.

2.1.7. The Green's tensor $\mathrm{G}(\mathbf{r}, \mathbf{r}', \boldsymbol{\omega})$

The Green's tensor appearing in equation (2.92) is a powerful classical means to describe electromagnetic fields in the presence of media or more specific in the vicinity of macroscopic objects. It is the solution to the inhomogeneous Helmholtz equation

$$\left(\nabla \times \frac{1}{\mu(\mathbf{r},\omega)}\nabla \times -\frac{\omega^2}{c^2}\varepsilon(\mathbf{r},\omega)\right)\boldsymbol{G}(\mathbf{r},\mathbf{r}',\omega) = \boldsymbol{\delta}(\mathbf{r}-\mathbf{r}') \tag{2.109}$$

with the boundary condition

$$\boldsymbol{G}(\mathbf{r},\mathbf{r}',\omega) \to \mathbf{0} \text{ for } |\mathbf{r}-\mathbf{r}'| \to \infty. \tag{2.110}$$

In general, the product of unit vectors $\mathbf{e}_i$ and the Green's tensor $\mathbf{e}_1 \cdot \boldsymbol{G}(\mathbf{r},\mathbf{r}',\omega)\cdot\mathbf{e}_2$ can be interpreted as the propagator of a field of frequency ω from a point source at $\mathbf{r}'$ with components along $\mathbf{e}_2$ to a point $\mathbf{r}$ where the field has components along $\mathbf{e}_1$. The Schwarz reflection principle for permittivity $\varepsilon^*(\mathbf{r},\omega) = \varepsilon(\mathbf{r},-\omega^*)$ and permeability $\mu^*(\mathbf{r},\omega) = \mu(\mathbf{r},-\omega^*)$ translates directly to the Green's tensor,

$$\boldsymbol{G}^*(\mathbf{r},\mathbf{r}',\omega) = \boldsymbol{G}(\mathbf{r},\mathbf{r}',-\omega^*). \tag{2.111}$$

Other important properties are the Onsager reciprocity,

$$\boldsymbol{G}^{\mathrm{T}}(\mathbf{r},\mathbf{r}',\omega) = \boldsymbol{G}(\mathbf{r}',\mathbf{r},\omega), \tag{2.112}$$

and the integral relation

$$\sum_{\lambda=e,m}\int \mathrm{d}^3r''\, \boldsymbol{G}_\lambda(\mathbf{r},\mathbf{r}'',\omega)\cdot\boldsymbol{G}_\lambda^{*T}(\mathbf{r}',\mathbf{r}'',\omega) = \frac{\hbar\mu_0}{\pi}\omega^2 \mathrm{Im}\boldsymbol{G}(\mathbf{r},\mathbf{r}',\omega). \tag{2.113}$$

with the coefficients (2.96) and (2.97). The large-frequency limit of the Green's tensor is

$$\lim_{|\omega|\to\infty}\frac{\omega^2}{c^2}\boldsymbol{G}(\mathbf{r},\mathbf{r}',\omega) = -\boldsymbol{\delta}(\mathbf{r}-\mathbf{r}'). \tag{2.114}$$

If a system consists of multiple media, i.e. multiple macroscopic regions with different magnetoelectric properties, it is convenient to separate the Green's tensor in a bulk part $\boldsymbol{G}^{(0)}(\mathbf{r}, \mathbf{r}', \omega)$ and a scattering part $\boldsymbol{G}^{(1)}(\mathbf{r}, \mathbf{r}', \omega)$,

$$\boldsymbol{G}(\mathbf{r}, \mathbf{r}', \omega) = \boldsymbol{G}^{(0)}(\mathbf{r}, \mathbf{r}', \omega) + \boldsymbol{G}^{(1)}(\mathbf{r}, \mathbf{r}', \omega). \tag{2.115}$$

Here, the bulk Green's tensor $\boldsymbol{G}^{(0)}(\mathbf{r}, \mathbf{r}'\omega)$ accounts only for the case where the two points $\mathbf{r}$ and $\mathbf{r}'$ are in the same bulk medium and can be connected by a straight line, cf. figure 2.1 **a**. The scattering Green's tensor can be interpreted as the propagator of a field component with frequency ω from $\mathbf{r}'$ to $\mathbf{r}$ by scattering from the boundary between the two macroscopic regions (figure 2.1 **b**) or from a source at $\mathbf{r}'$ to a point $\mathbf{r}$ that lie in two regions with different magnetoelectric properties (figure 2.1 **c**). While $\boldsymbol{G}^{(1)}(\mathbf{r}, \mathbf{r}', \omega)$ is hard to compute in general, analytic expressions can be found for rather simple cases. For example, $\boldsymbol{G}^{(1)}(\mathbf{r}, \mathbf{r}', \omega)$ is known for source and field point $\mathbf{r}', \mathbf{r}$ in both the same and different layers of layered media or outside of spherical or cylindrical objects [13]. In appendix A additional properties of the Green's tensor are shown along with explicit expressions for Green's tensors used in this work.

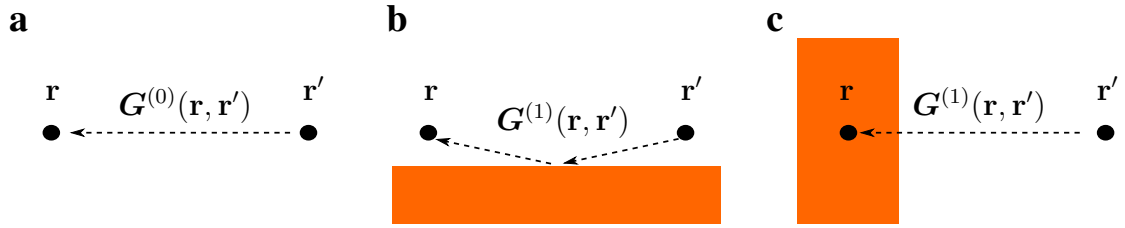

Figure 2.1.: Illustration of the Green's tensor as the propagator of the electromagnetic field from $\mathbf{r}'$ to $\mathbf{r}$. The ω dependence is left out for brevity. **a** Free-space Green's tensor $\boldsymbol{G}^{(0)}(\mathbf{r}, \mathbf{r}', \omega)$. **b** The scattering Green's tensor $\boldsymbol{G}^{(1)}(\mathbf{r}, \mathbf{r}', \omega)$ describes the propagation from $\mathbf{r}'$ to $\mathbf{r}'$ via a path that is scattered at the surface (orange). The contribution of $\boldsymbol{G}^{(0)}(\mathbf{r}, \mathbf{r}', \omega)$ is not shown. **c** If $\mathbf{r}'$ and $\mathbf{r}'$ are positioned in different media, the propagation is described by the scattering Green's tensor $\boldsymbol{G}^{(1)}(\mathbf{r}, \mathbf{r}', \omega)$.

2.2. Dispersion Forces

In classical physics, the vacuum is defined by the absence of everything including particles, currents or fields. While this is still true in quantum physics, we have seen that the fluctuation-dissipation theorem for noise polarization and magnetization, equations (2.85) and (2.86), respectively, results in non-vanishing expectation values of the fluctuations of the vacuum noise. Therefore, also fluctuations of the electric field are present in vacuum. The fluctuation-

dissipation theorem for the electric field $\hat{\mathbf{E}}$ at zero temperature is

$$\frac{1}{2}\langle\Delta\hat{\mathbf{E}}(\mathbf{r},\omega)\Delta\hat{\mathbf{E}}^{\dagger}(\mathbf{r}',\omega')+\Delta\hat{\mathbf{E}}^{\dagger}(\mathbf{r}',\omega')\Delta\hat{\mathbf{E}}(\mathbf{r},\omega)\rangle=\frac{\hbar}{2\pi}\mu_0\omega^2\mathrm{Im}\boldsymbol{G}(\mathbf{r},\mathbf{r}'\omega)\delta(\omega-\omega') \tag{2.116}$$

and contains the imaginary part of the Green's tensor $\mathrm{Im}\boldsymbol{G}$. From the definition of the bulk Green's tensor (A.9) it is straight forward to calculate the coincidence limit $\mathbf{r}' \to \mathbf{r}$,

$$\mathrm{Im}\boldsymbol{G}^{(0)}(\mathbf{r},\mathbf{r},\omega)=\frac{\omega}{6\pi c}\mathbf{I}. \tag{2.117}$$

Therefore, every object or medium is subject to the interaction with these vacuum fluctuations and in addition interactions between different objects are induced by the fluctuations.[1]

One often distinguishes between three different cases of interactions. *Casimir forces* are forces between two macroscopic bodies (Fig. (2.2**a**), *Casimir-Polder forces* act between a macroscopic body and a microscopic object, e.g. an atom or molecule, (Fig. (2.2**b**) and the *van der Waals forces* are forces between two microscopic objects (Fig. (2.2**c**).

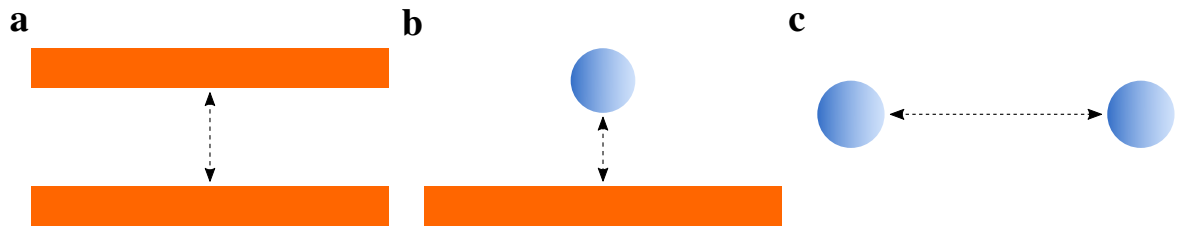

Figure 2.2.: Schematic illustration of the dispersion forces. **a** Casimir effect between two plates. **b** Casimir-Polder effect between an atom and a surface. **c** van der Waals forces between two atoms.

The big caveat, though, is that these three terms are sometimes interchanged. There are examples in the literature where atom-body interactions are referred to as Casimir forces [37] or van der Waals interactions [38; 39]. On the other hand, intermolecular interactions might be referred to as Casimir-Polder dispersion energy shifts [40]. This can be justified by the fact that all three interactions are a result of the same effect, the vacuum fluctuations. However, for clarity and to avoid ambiguity, in this thesis I will stick to the nomenclature established by Scheel and Buhmann [12] that was introduced above.

[1] While zero-point fluctuations of the quantized electromagnetic field are an excellent approach to explain the occurrence of dispersion forces, Lifshitz's calculation of the Casimir force [33] is based on the classical thermal fluctuations of charge and currents inside the media from Rytov theory [34]. There are also calculations at zero temperature that take into account the radiation reaction rather than the vacuum field fluctuations [35]. While the Casimir effect, thus, is not a result to prove the quantum nature of the electromagnetic field, it has been shown that the quantum electrodynamic and classical approaches are interchangeable [36].

2.2.1. Casimir-Polder forces

An intuitive approach to understanding Casimir-Polder interactions is to consider the vacuum fluctuations inducing a dipole moment in an atom which thereupon induces a mirror dipole moment in some macroscopic object. This situation is pictured in figure 2.3. The interaction between these two dipoles is then described by the Casimir-Polder potential U_{CP} which yields the Casimir-Polder force $\mathbf{F}_{\mathrm{CP}} = -\nabla U_{\mathrm{CP}}$. The potential U_{CP} is attractive in general [12–14; 41] but there are exceptions to this rule. One instance of repulsive Casimir-Polder interactions can be realized for atoms close to conducting materials with sharp edges [42; 43]. These repulsions are usually rather weak and there are likely better possibilities to engineer surfaces in order to achieve maximum repulsion [44]. For ground state atoms at rest, the Casimir-Polder potential U_{CP} in electric-dipole approximation is given by

$$U_{\mathrm{CP}}(\mathbf{r}_A) = \sum_{I\neq 0} \frac{\langle 0|\hat{H}_{\mathrm{int}}|I\rangle\langle I|\hat{H}_{\mathrm{int}}|0\rangle}{E_0 - E_I} \tag{2.118}$$

$$= \frac{\hbar\mu_0}{2\pi}\int_0^\infty \mathrm{d}\xi\, \xi^2 \mathrm{Tr}\left(\boldsymbol{\alpha}(i\xi)\cdot\boldsymbol{G}^{(1)}(\mathbf{r}_A,\mathbf{r}_A,i\xi)\right). \tag{2.119}$$

Here, the $\boldsymbol{\alpha}(i\xi)$ is the atomic polarizability tensor

$$\boldsymbol{\alpha}(\omega) = \lim_{\epsilon\to 0+}\frac{1}{\hbar}\sum_k\left(\frac{\mathbf{d}_{k0}\otimes\mathbf{d}_{0k}}{\omega+\omega_k+i\epsilon} - \frac{\mathbf{d}_{0k}\otimes\mathbf{d}_{k0}}{\omega-\omega_k+i\epsilon}\right) \tag{2.120}$$

containing dipole transition moments $\mathbf{d}_{0k}$ and the respective frequencies ω_k. Since the Casimir-Polder potential is the potential between a macroscopic body and an atom, only the scattering Green tensor $\boldsymbol{G}^{(1)}$ is accounted for in equation (2.119). The interaction of the atom with the free space Green tensor $\boldsymbol{G}^{(0)}$ is the atom's lamb shift ΔE_{Lamb} that is taken to be included in the atoms energy levels $|k\rangle$. For a perfectly conducting half space, the Casimir-Polder potential obeys a simple power law for surface distance r, $U_{\mathrm{CP}}(r) \sim r^{-3}$ in the nonretarded (small-distance) limit and $U_{\mathrm{CP}}(r) \sim r^{-4}$ in the retarded (long-distance) limit. Measurements have confirmed the Casimir-Polder effect for atom-surface separations in the range of $\sim 10^{-7}$ – 10^{-5} μm [41]. Another approach to determine the exact surface potential utilizes a repulsive evanescent wave potential that in combination with the Casimir-Polder potential forms a potential barrier close to the surface [45]. The position and height of the barrier are determined with a reflection experiment of an ultracold atomic cloud. From this knowledge, the exact surface potential can be extracted [46]. While the atomic reflection in the above mentioned experiment takes place at a repulsive potential barrier, Casimir-Polder potentials offer the opportunity to investigate the process of reflection of particles from purely attractive potentials

called quantum reflection. Experiments have been conducted for atoms at grazing [47; 48] or normal [49] incidence and have been proposed for more exotic systems such as antimatter [50; 51].

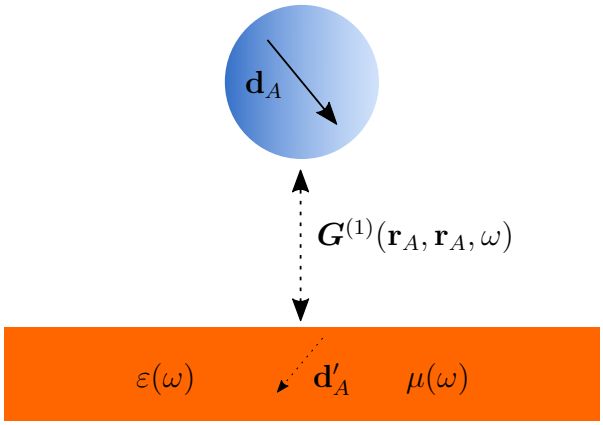

Figure 2.3.: One atom A above a surface with permittivity $\varepsilon(\omega)$ and permeability $\mu(\omega)$. The atomic dipole moment $\mathbf{d}_A$ induces a mirror dipole moment $\mathbf{d}'_A$ in the surface. For non-perfect conductors $|\mathbf{d}_A| > |\mathbf{d}'_A|$. The dashed two-headed arrow represents the exchange of virtual photons between atom and surface. Their propagation is described by the scattering Green's tensor $\boldsymbol{G}^{(1)}(\mathbf{r}_A, \mathbf{r}_A, \omega)$. The exchange of virtual photons with the surface causes the Casimir-Polder potential.

2.2.2. van der Waals interactions

Finally, the van der Waals interaction is the dispersion force between two microscopic particles such as atoms or molecules. Again, the intuitive approach is straight forward: the vacuum fluctuations of the electromagnetic field induce a dipole moment in both atoms which subsequently interact. Another equivalent way of looking at this is that the atomic dipole moments themselves fluctuate causing the interaction. The van der Waals potential can be derived by fourth order perturbation theory of the atom-field Hamiltonian in dipole approximation $\hat{H}_{iF} = -\hat{\mathbf{d}}_i \cdot \hat{\mathbf{E}}(\mathbf{r}_i)$. For two ground state atoms A and B, each atom has to undergo two interactions with the electric field in order to be excited from and return to its ground state. The energy shift is then

$$U_{\mathrm{vdW}}(\mathbf{r}_A, \mathbf{r}_B) = \sum_{I,II,III \neq 0} \frac{\langle 0|\hat{H}_{\mathrm{int}}|III\rangle\langle III|\hat{H}_{\mathrm{int}}|II\rangle\langle II|\hat{H}_{\mathrm{int}}|I\rangle\langle I|\hat{H}_{\mathrm{int}}|0\rangle}{(E_0 - E_{III})(E_0 - E_{II})(E_0 - E_I)} \tag{2.121}$$

where $\hat{H}_{\mathrm{int}}$ equals $\hat{H}_{AF}$ and $\hat{H}_{BF}$ for exactly two of the four transitions, respectively. The Green's tensor is included in the Hamiltonian $\hat{H}_{iF}$ via the expansion of the electric field (2.95). As the van der Waals interaction is a two-particle effect, both free space and scattering Green's

tensor contribute to it and $\boldsymbol{G}(\mathbf{r}_A, \mathbf{r}_B, \omega) = \boldsymbol{G}^{(0)}(\mathbf{r}_A, \mathbf{r}_B, \omega) + \boldsymbol{G}^{(1)}(\mathbf{r}_A, \mathbf{r}_B, \omega)$. Taking into account all intermediate states $|I\rangle$, $|II\rangle$ and $|III\rangle$, one arrives at

$$U_{\mathrm{vdW}}(\mathbf{r}_A, \mathbf{r}_B) = -\frac{\hbar\mu_0^2}{2\pi}\int_0^\infty \mathrm{d}\xi\, \xi^4 \mathrm{Tr}\left[\boldsymbol{\alpha}_A(i\xi)\cdot\boldsymbol{G}(\mathbf{r}_A, \mathbf{r}_B, i\xi)\cdot\boldsymbol{\alpha}_B(i\xi)\cdot\boldsymbol{G}(\mathbf{r}_B, \mathbf{r}_A, i\xi)\right]. \tag{2.122}$$

In contrast to the Casimir-Polder potential (2.119), the van der Waals potential features the atomic polarizabilities of two atoms as well as the product of two Green's tensors. Splitting the Green's tensor in a bulk and a scattering part according to equation (2.115), there are 3 terms to the potential. Interpreting electrodynamic interactions as the exchange of virtual photons, the terms can be read as (1) a photon propagating from atom A to B and back in free space $\sim \boldsymbol{G}^{(0)}\cdot\boldsymbol{G}^{(0)}$, (2) photon propagation via scattering at some surface, $\sim \boldsymbol{G}^{(1)}\cdot\boldsymbol{G}^{(1)}$, and (3) mixed terms $\sim \boldsymbol{G}^{(1)}\cdot\boldsymbol{G}^{(0)}$ where the photon is scattered by the surface in one direction and propagates freely in the other direction. Figure 2.4 provides a simple intuitive overview of the different contributions to the Casimir-Polder and van der Waals potential by scattering and free space Green's tensors. The free space van der Waals potential displays a r^{-6} dependence in the nonretarded limit and a r^{-7} dependence in the retarded limit. This leads to negligible effects at large distances but makes the van der Waals potential the dominant interparticle potential at small separations.

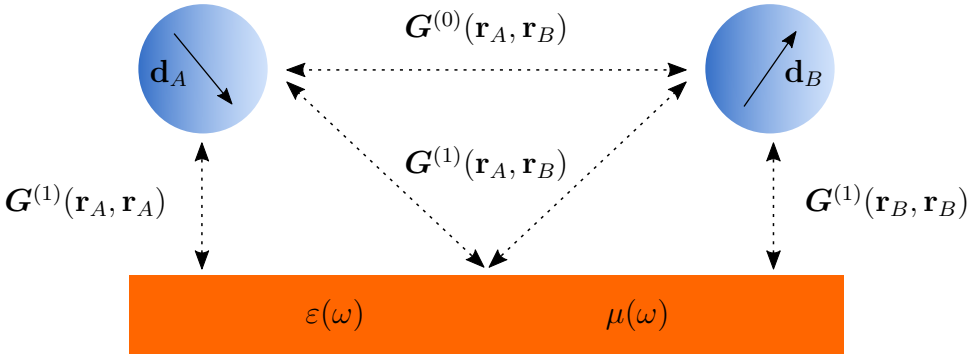

Figure 2.4.: Two atoms with dipole moments $\mathbf{d}_A$ and $\mathbf{d}_B$ above a surface with permittivity $\varepsilon(\omega)$ and permeability $\mu(\omega)$. Dashed lines represent possible paths of propagation for (virtual) photons. Atomic interactions are mediated by the free space Green's tensor $\boldsymbol{G}^{(0)}(\mathbf{r}_A, \mathbf{r}_B)$. In proximity to a surface, the scattering Green's tensor $\boldsymbol{G}^{(1)}(\mathbf{r}_A, \mathbf{r}_B)$ also contributes to the interatomic forces. In addition, both atoms induce a mirror dipole moment in the surface (not depicted) and are, thus, subject to a Casimir-Polder potential described by the scattering Green's tensor in the coincidence limit, $\boldsymbol{G}^{(1)}(\mathbf{r}_i, \mathbf{r}_i)$. The ω dependence of $\boldsymbol{G}^{(0)}$ and $\boldsymbol{G}^{(1)}$ is omitted for brevity.

2.3. Rydberg physics

The hydrogen atom is composed of a single proton and electron and due to its simplicity it is possible to solve its Schrödinger equation analytically. This results in an energy spectrum $E \sim -E_{\mathrm{Ryd}}/n^2$ with the Rydberg energy $E_{\mathrm{Ryd}} = 13.6\,\mathrm{eV}$ and principal quantum number n, that was first described in 1885 by Balmer [52]. Rydberg particles in general are highly excited particles or quasiparticles that allow a description of their energy levels by a formula similar to the hydrogen spectrum,

$$E = -\frac{E^*_{\mathrm{Ryd}}}{(n-\delta_{nlj})^2}. \tag{2.123}$$

Here, E^*_{Ryd} the Rydberg energy of the specific particle which for atoms is typically of same the order as the Rydberg energy of hydrogen. The quantum defect δ_{nlj} depends on the particle species as well as n, the angular momentum l and the total angular momentum j. The reason that highly excited particles possess a hydrogen-like energy spectrum can be understood easily. In atoms, high excitations of the outmost electron lead to a high expectation value $\langle r\rangle$ of the electron's wave function as $\langle r\rangle \sim n^2 a_0$ with the Bohr radius a_0 [1]. For high angular momentum l, the electron is in a circular Bohr orbit and therefore the electron's probability density function has negligible contributions at the atomic core. In this case, the excited atom can be described by a single electron and an effective atomic core with net charge $+1e$ consisting of the actual atomic core and the inner electron cloud. The combination of a single positively charged core and a single electron resembles the setup of the hydrogen atom. However, this approximation breaks down for smaller l when the excited electron's wave function overlaps significantly with the inner electron cloud and the core. The quantum defect δ_{nlj} accounts for these deviations from the hydrogen-like setup and allows to maintain the simple energy spectrum (2.123). Therefore, δ_{nlj} decreases with increasing angular momenta l and j and approaches a constant value for large n.

2.3.1. Properties of Rydberg atoms

As one can see from the spectrum (2.123), the binding energy scales with n^{-2} and the energy difference $\Delta E_{n,n+1}$ scales with n^{-3}. In experiments, record quantum numbers $n > 400$ can be achieved [53; 54], leading to radial expectation values of the Rydberg electrons wave function of $\langle r\rangle \sim 1.6\times 10^5 a_0 \sim 8.5\,\mu\mathrm{m}$. The large extent of the wave function consequently leads to large transition dipole moments between adjacent Rydberg states, $\langle nf|er|nd\rangle \sim n^2$, and thus

a large atomic polarizability $\boldsymbol{\alpha} \sim n^7$ [1]. As a result, Rydberg atoms interact strongly with other atoms, electromagnetic fields or surrounding media. This fact is exploited in order to use Rydberg atoms as a sensor for very accurate measurements of the strength of electric fields with frequencies in the range from $1\,\mathrm{GHz}$ to $500\,\mathrm{GHz}$ [55]. The radiative lifetime of Rydberg states that scales with n^3 benefits the experimental accessibility of the Rydberg states themselves as well as their unique features. For room temperature Rb Rydberg atoms, lifetimes of the order of $20\,\mu\mathrm{s}$ - $60\,\mu\mathrm{s}$ have been reported for moderate $n \sim 40$ [56].

2.3.2. Rydberg blockade

One intriguing result of the strong interparticle interactions is called Rydberg blockade. Rydberg atoms are excited via a laser of frequency ω_L that matches the transition frequency ω_{eg} between the ground state $|g\rangle$ and the desired Rydberg level $|e\rangle$. However, when two or more atoms are in close proximity, the interactions between them can shift the Rydberg level $|e\rangle \to |e'\rangle$ such that the transition frequency $\omega_{e'g}$ lies outside the laser linewidth $\delta\omega_L$ which inhibits a second Rydberg excitation [19]. For unpolarized atoms, the main interaction is the van der Waals potential (2.122) which can be approximated by its nonretarded limit $U_{\mathrm{vdW}} = -C_6/r^6$ due to the large transition wavelengths between Rydberg levels. The blockade radius

$$R_{\mathrm{block}} = \sqrt[6]{\frac{C_6}{\hbar\delta\omega_L}} \tag{2.124}$$

with the van der Waals-coefficient C_6 follows directly from the prerequisite that $U_{\mathrm{vdW}} \geq \hbar\delta\omega_L$. Because of the underlying interatomic potential the blockade mechanism is also referred to as van der Waals blockade [57]. The mechanism behind the Rydberg blockade is illustrated in figure 2.5 **a**. In figure **b**, the consequences for an atomic ensemble are sketched. Only a single excitation is possible in a volume with radius R_{block}.

Rydberg blockade becomes apparent in ensembles of some 10^7 cold ^{85}Rb atoms [58]. Here, the interatomic interactions permit only a single excitation in a spherical volume with the blockade radius R_{block}. In such a blockaded sphere, all atoms are in a superposition of the single excitation and the ground state. Therefore, the effective system can be described by a two-level state of a multitude of atoms and is called a superatom [59]. Moving away from the static picture of the superatom one can also take into account the propagation of the excitation, i.e. the light field, inside this ensemble of atoms. The result is the well-known quasiparticle called polariton, defined by the strong coupling of the photonic mode to the (static) superatom [22; 60].

The Rydberg blockade is the foundation for an overabundance of applications. For example, single-photon emission from an ensemble of cold ($T \approx 10\,\mu$K) ^{87}Rb atoms has been achieved by taking advantage of the Rydberg blockade [61]. Recently, Ripka *et al.* [62] accomplished similar results even at room temperature. With $R_{\mathrm{block}} \approx 1\,\mu$m, the superatom is larger than the optical wavelength which leads to well-defined directional photon emission [63].

Numerical simulations indicate the possibility to construct single-qubit and two-qubit quantum gates with high fidelity using superatoms [64]. So-called dark-state polaritons are a possible candidate of light storage [65; 66]. Overall, Rydberg blockade and related effects play an important role on the way towards quantum memory and quantum computing.

While the blockade effect becomes most apparent in an atomic ensemble, it could also be reproduced in a two-atom setup where ^{87}Rb atoms were moved with optical tweezers. Rydberg blockade could be observed for interatomic separations of $10.2\,\mu$m due to an energy shift of approximately $3\,$MHz of the $|79d\rangle$-state [67].

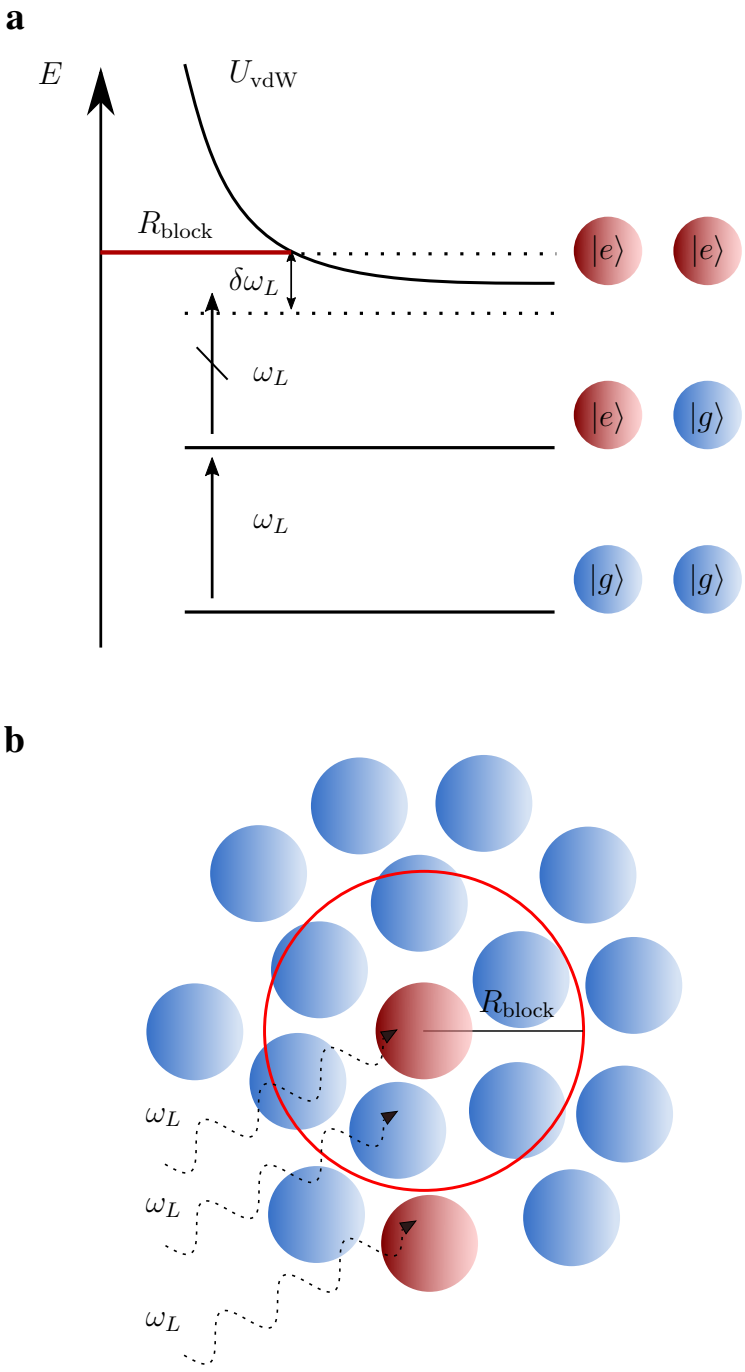

Figure 2.5.: **a** Two atoms in their ground states $|g\rangle|g\rangle$ are excited with a laser with frequency ω_L. After one laser pulse ω_L, the atoms are in a superposition state of one ground state $|g\rangle$ and one excited state $|e\rangle$. The two excited states $|e\rangle|e\rangle$ interact via the van der Waals potential U_{vdW}. For interatomic distances smaller than R_{block}, the interaction shifts the states out of the laser resonance that is defined by the linewidth $\delta\omega_L$ and the excitation is prohibited. This is called Rydberg blockade or van der Waals blockade. **b** Rydberg atom excitation in an atomic ensemble. Inside a blockade volume indicated by R_{block}, only one excitation is possible due to the Rydberg blockade.

2.3.3. Multi-particle Rydberg systems

Rydberg atoms can form a variety of bound states. One class of bound states from the low-energy scattering between a Rydberg electron and a ground state atom yielding so-called Rydberg molecules [68–72]. Rydberg molecules of the first kind are formed by a Rydberg electron with low angular momentum l (typically $l \leq 2$) and a perturbing ground state atom. In this case, the perturber is trapped in potential wells in the lobes of the Rydberg electron wave function [73]. By contrast, Rydberg molecules of the second kind possess a Rydberg electron with high l. Due to the vanishing quantum defect δ_{nlj} at high l, the electron occupies a highly degenerate subspace similar to that of the hydrogen atom. The perturbing ground state atom causes potential wells in the hydrogen-like energy levels that are deeper than those of the low-l states [68]. Wave functions of these high-l Rydberg molecules form peculiar shapes like the famous trilobite molecule [68] or the so-called butterfly [73; 74], cf. figure 2.6. While they are a fascinating species to study by themselves, Rydberg molecules can be used to investigate atom-ion scattering at low energies [75]. In addition to the two particle system of Rydberg atom and ground state atom, three-body Rydberg molecules are predicted as well [76].

A different class of molecules stems from the interaction of two Rydberg particles. When two Rydberg atoms form a bound state the resulting molecule is known as a Rydberg macrodimer. These gigantic diatomic particles with radial wave functions of several μm were experimentally confirmed both with and without external electromagnetic field [77–79] and in an optical lattice [80]. Similar to the Rydberg molecules, three-body Rydberg macrotrimers are predicted

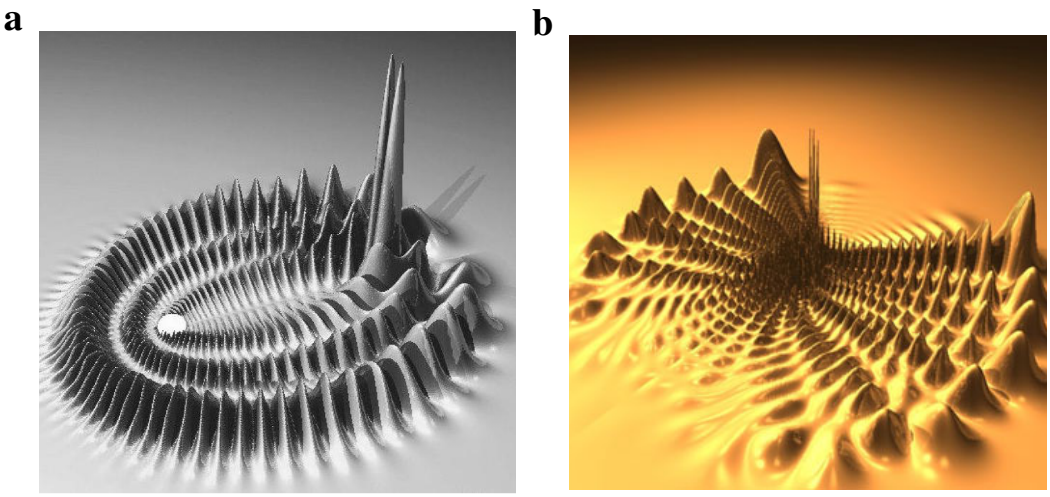

Figure 2.6.: The wave functions of **a** the trilobite molecule, taken from [68], and **b** the butterfly molecule, taken from [74].

as well [81]. In section 4.3 we show that the presence of a perfectly conducting surface suffices to alter the interatomic interactions between two Rydberg atoms in such a way that macrodimers form.

Also noteworthy are Rydberg quasimolecules that consist of two charges Z and Z', e.g. atomic cores, that share one highly excited electron [82]. When one refers to molecules that themselves are excited to a Rydberg level, one speaks of molecular Rydberg states [83].

2.3.4. Rydberg excitons

As stated above, Rydberg states have been reported for quasiparticles as well. The most famous example are the Rydberg excitons that were first observed in cuprous oxide Cu_2O in the 1950s [84] and later in other materials such as WS_2 [85] and WSe_2 [86]. Excitons are bound electron-hole pairs in semiconductors. While the Rydberg energies of excitons in Cu_2O ($E^*_{\mathrm{Ryd}} = 86\,\mathrm{meV}$) and WSe_2 ($E^*_{\mathrm{Ryd}} = 168.6\,\mathrm{meV}$) are small compared to the hydrogenic Rydberg energy, their energies are relative to the semiconductor's band gap E_{gap}. The excitonic spectrum reads

$$E_{\mathrm{exc}} = E_{\mathrm{gap}} - \frac{E^*_{\mathrm{Ryd}}}{n^{*,2}}. \tag{2.125}$$

Since $E_{\mathrm{gap,Cu_2O}} \approx 2\,\mathrm{eV}$, the excitonic states are accessible using lasers with energies in the eV-range [86; 87]. As a result of the small Rydberg energy, the maximum quantum number n_{max} before dissociation is much lower than for atomic Rydberg states where quantum numbers as large as $n \sim 500$ are obtained [54]. While in the first experiments, $n_{\mathrm{max}} = 8$ could be achieved [84], as late as in 2014 quantum numbers up to $n_{\mathrm{max}} = 25$ [87] and recently even $n_{\mathrm{max}} = 30$ [88] were reported. Temperatures of $T = 38\,\mathrm{mK}$ were necessary for the record $n_{\mathrm{max}} = 30$. In Cu_2O, a huge exciton extension of $\sim 2\,\mu\mathrm{m}$ was reported, leading to strong interactions with the crystal and a high susceptibility to any imperfections [87].

On the other hand, Rydberg excitons possess features that distinguish them from atomic Rydberg atoms and make them an interesting subject. While a single atom can be investigated in an isotropic vacuum, the rotational symmetry is broken for excitons in cubic crystals [89]. This leads to the excitation of states with higher angular momenta l with a single photon, i.e. the well-known selection rule $\Delta l = \pm 1$ for electric dipole transitions is violated. The exciton states are labelled according to the involved valence and conduction bands of the semiconductor. Thus, the two uppermost valence bands and the two lowest conduction bands of Cu_2O form four excitonic series [90]. This is in stark contrast to the Rydberg atoms where usually only the

single series of the outmost valence electron is considered. Krüger and Scheel [90] found that for interseries transitions the dipole approximation fails already at moderate $n \approx 10$. Finally, due to their containment inside crystals excitonic systems provide a means to solid state sources of single photons exploiting the effect of Rydberg blockade [91]. When considering technical applications solid state devices are often preferable to atomic solutions because of the naturally fewer moving parts.

Chapter 3.

Casimir-Polder induced Rabi oscillations

One atom in front of a macroscopic body is subject to the Casimir-Polder potential (2.119). It has been shown for excited atoms, that the Casimir-Polder interaction induces a Rabi oscillation between states as well as a decay rate in second order perturbation theory [14]. For ground state atoms in front of a perfectly conducting plate, Rabi oscillations between non-degenerate hyperfine states with low frequencies were predicted as well from second order equations of motion [92]. When an atom is positioned above a corrugated surface, a rack and pinion motion is predicted [93]. This non-contact device is powered by the lateral components of the Casimir-Polder force. While spontaneous emission of an atom is isotropic in general, for a suitably oriented dipole in close proximity to an optical nanofiber the emission pattern becomes asymmetric [94]. This leads to a net lateral force that propels the atom along the nanofiber. Lateral Casimir-Polder forces are also predicted for rotating particles in front of a plain surface [95].

Based on these observation, the question arises whether lateral Casimir-Polder forces can also be derived from fourth order equations of motions which will be investigated in this chapter. One can imagine that an atom either decays into a single hyperfine state or, starting from a single hyperfine state the occupation probability is spread out over multiple states. In both cases, the atom would gain an average momentum kick [94].

This chapter is organized as follows. As a preliminary, the atom-field Hamiltonian $\hat{H}_{AF}$ and important commutation relations are reviewed. This is followed by a discussion of the Markov approximation that is applied in the calculation. Then, a generic fourth order equation of motion is derived for an atomic operator $\hat{\sigma}_{mn}(t)$. This equation features the scattering Green's tensor $\boldsymbol{G}^{(1)}(\mathbf{r}, \mathbf{r}, \omega)$ in the coincidence limit and arbitrary atomic states. The results are then applied to an idealized ^{87}Rb atom in proximity of a plain infinite dielectric plate. A sketch of the system

can be found in figure 2.3. While for different dielectrics Rabi frequencies $\Omega_{\mathrm{Rabi}} \leq 0.3\,\mathrm{rad/s}$ can be found, no additional decay rate is introduced by fourth order processes.

3.1. Preliminaries

3.1.1. The Hamiltonian

The Hamiltonian $\hat{H}$ for an atom in an electromagnetic field is $\hat{H} = \hat{H}_A + \hat{H}_F + \hat{H}_{AF}$ with the atom Hamiltonian $\hat{H}_A$, the free field Hamiltonian $\hat{H}_F$ and the atom-field Hamiltonian $\hat{H}_{AF}$. Considering the atom at rest eliminates the kinetic term from $\hat{H}_A$ making the atomic states $|i\rangle$ eigenstates of $\hat{H}_A$, $\hat{H}_A|i\rangle = \hbar\omega_i|i\rangle$. The focus in this chapter is on the Casimir-Polder driven dynamics and, thus, the free field contribution from $\hat{H}_F$ is neglected. Second order perturbation theory with the atom-field Hamiltonian $\hat{H}_{AF}$ leads to the Casimir-Polder potential (2.119).

The electric field can be written in terms of field creation an annihilation operators $\hat{\mathbf{f}}^\dagger$ and $\hat{\mathbf{f}}$, respectively by combining equations (2.95) and (2.98),

$$\hat{\mathbf{E}}(\mathbf{r},\omega) = \sum_{\lambda=e,m} \int \mathrm{d}^3 r'\, \boldsymbol{G}_\lambda(\mathbf{r},\mathbf{r}',\omega)\cdot\hat{\mathbf{f}}_\lambda(\mathbf{r}',\omega) + \hat{\mathbf{f}}^\dagger\cdot\boldsymbol{G}^{*T}_\lambda(\mathbf{r},\mathbf{r}',\omega). \tag{3.1}$$

In dipole approximation, the atom-field interaction Hamiltonian of non-magnetic atom A at rest at position $\mathbf{r}_A$ is given by

$$\begin{aligned}\hat{H}_{AF} &= -\hat{\mathbf{d}}_A\cdot\hat{\mathbf{E}}(\mathbf{r}_A)\\ &= -\sum_{ij}\int_0^\infty \mathrm{d}\omega \sum_\lambda \int \mathrm{d}^3 r' \Big(\hat{\sigma}_{ij}(t)\mathbf{d}_{ij}\cdot\boldsymbol{G}_\lambda(\mathbf{r}_A,\mathbf{r}',\omega)\cdot\hat{\mathbf{f}}_\lambda(\mathbf{r}',\omega,t)\\ &\qquad + \hat{\mathbf{f}}^\dagger_\lambda(\mathbf{r}',\omega,t)\cdot\boldsymbol{G}^{*T}_\lambda(\mathbf{r}_A,\mathbf{r}',\omega)\cdot\mathbf{d}_{ij}\hat{\sigma}_{ij}(t)\Big).\end{aligned} \tag{3.2}$$

Here, the atomic dipole moment is $\hat{\mathbf{d}}_A = \sum_{ij}\hat{\sigma}_{ij}(t)\mathbf{d}_{ij}$. The sum runs over all atomic states i, j and $\hat{\sigma}_{ij}(t) = |i\rangle\langle j|$. As stated before, the field Hamiltonian

$$\hat{H}_F = \sum_\lambda \int \mathrm{d}^3 r \int \mathrm{d}\omega\, \hbar\omega \hat{\mathbf{f}}^\dagger(\mathbf{r},\omega,t)\cdot\hat{\mathbf{f}}(\mathbf{r},\omega,t) \tag{3.3}$$

is ignored in these considerations because the interest is focused in the atomic dynamics due to the Casimir-Polder interaction. Any background field, e.g. a laser or thermal excitations, would have to be included in $\hat{H}_F$ and would also contribute to the atom-field interactions $\hat{H}_{AF}$.

Together with the integral relation for the Green's tensor (2.113), the commutation relations for $\hat{\mathbf{f}}^{(\dagger)}$ and $\hat{\mathbf{E}}^{(\dagger)}$ can be calculated:

$$\left[\hat{\mathbf{f}}_\lambda(\mathbf{r},\omega,t),\hat{\mathbf{f}}^\dagger_{\lambda'}(\mathbf{r}',\omega',t)\right] = \delta_{\lambda\lambda'}\boldsymbol{\delta}(\mathbf{r}-\mathbf{r}')\delta(\omega-\omega'), \tag{3.4}$$

$$\left[\hat{\mathbf{E}}(\mathbf{r}_A,t),\hat{H}_{AF}(t)\right] = -\sum_{ij}\int_0^\infty \mathrm{d}\omega\,\frac{\hbar\mu_0}{\pi}\omega^2 \mathrm{Im}\boldsymbol{G}(\mathbf{r}_A,\mathbf{r}_A,\omega)\cdot\mathbf{d}_{ij}\hat{\sigma}_{ij}(t), \tag{3.5}$$

$$\left[\hat{\mathbf{E}}^\dagger(\mathbf{r}_A,t),\hat{H}_{AF}(t)\right] = \sum_{ij}\int_0^\infty \mathrm{d}\omega\,\frac{\hbar\mu_0}{\pi}\omega^2 \hat{\sigma}_{ij}(t)\mathbf{d}_{ij}\cdot\mathrm{Im}\boldsymbol{G}(\mathbf{r}_A,\mathbf{r}_A,\omega). \tag{3.6}$$

3.1.2. Markov approximation and time integral

The Markov approximation is used for the calculations in the following. In order to clarify the calculations, a short review is presented here. In a given term at a time $t_i < t$, one can split the fast oscillatory behavior from both the atomic flip operator and the electric field according to $\hat{\sigma}_{mn}(t_i)\mathbf{d}_{kl}\cdot\hat{\mathbf{E}}(\omega,t_i) = \hat{\sigma}'_{mn}(t_i)\mathbf{d}_{kl}\cdot\hat{\mathbf{E}}'(\omega,t_i)e^{i(\omega-\omega_{nm})t_i}$. As the next step, the (slow) temporal changes in $\hat{\sigma}'_{mn}$ and $\hat{\mathbf{E}}'$ are ignored under a time integral:

$$\int_{t_0}^t \mathrm{d}t_i\,\hat{\sigma}_{mn}(t_i)\mathbf{d}_{kl}\cdot\hat{\mathbf{E}}(\omega,t_i) = \int_{t_0}^t \mathrm{d}t_i\,\hat{\sigma}'_{mn}(t_i)\mathbf{d}_{kl}\cdot\hat{\mathbf{E}}'(\omega,t_i)e^{i(\omega-\omega_{nm})t_i} \tag{3.7}$$

$$\approx \hat{\sigma}'_{mn}(t)\mathbf{d}_{kl}\cdot\hat{\mathbf{E}}'(\omega,t)\int_{t_0}^t \mathrm{d}t_i\,e^{i(\omega-\omega_{nm})t_i} \tag{3.8}$$

$$= \hat{\sigma}_{mn}(t)\mathbf{d}_{kl}\cdot\hat{\mathbf{E}}(\omega,t)\int_{t_0}^t \mathrm{d}t_i\,e^{-i(\omega-\omega_{nm})(t-t_i)}. \tag{3.9}$$

Due to repeated application of the Markov approximation (3.8), nested time integrals appear in the equation of motion. These integrals are of the form

$$\begin{aligned}\int_{t_0}^t \mathrm{d}t_3\int_{t_0}^{t_3}\mathrm{d}t_2\int_{t_0}^{t_2}\mathrm{d}t_1\,e^{\mathrm{i}\Omega_1(t_2-t_1)}e^{\mathrm{i}\Omega_2(t_3-t_2)}e^{\mathrm{i}\Omega_3(t-t_3)}&\\ = -\frac{\mathrm{i}\left(1-e^{\mathrm{i}\Omega_3(t-t_0)}\right)}{\Omega_1\Omega_2\Omega_3} - \frac{\mathrm{i}\left(e^{\mathrm{i}\Omega_2(t-t_0)}-e^{\mathrm{i}\Omega_3(t-t_0)}\right)}{\Omega_1\Omega_2(\Omega_2-\Omega_3)}&\\ + \frac{\mathrm{i}\left(e^{\mathrm{i}\Omega_1(t-t_0)}-e^{\mathrm{i}\Omega_3(t-t_0)}\right)}{\Omega_1(\Omega_1-\Omega_2)(\Omega_1-\Omega_3)} + \frac{\mathrm{i}\left(e^{\mathrm{i}\Omega_2(t-t_0)}-e^{\mathrm{i}\Omega_3(t-t_0)}\right)}{\Omega_1(\Omega_1-\Omega_2)(\Omega_2-\Omega_3)}.&\end{aligned} \tag{3.10}$$

The result consists of one term $-\frac{\mathrm{i}}{\Omega_1\Omega_2\Omega_3}$ and seven others proportional to exponential functions. Letting $t_0\to-\infty$ and introducing a small imaginary part according to

$$\Omega_i \to \Omega_i + \mathrm{i}\Gamma_i, \tag{3.11}$$

the result simplifies significantly. In this limit, all exponential functions vanish and the final result is

$$\lim_{t_0\to-\infty}\int_{t_0}^{t}\mathrm{d}t_3\int_{t_0}^{t_3}\mathrm{d}t_2\int_{t_0}^{t_2}\mathrm{d}t_1\, e^{\mathrm{i}\Omega_1(t_2-t_1)}e^{\mathrm{i}\Omega_2(t_3-t_2)}e^{\mathrm{i}\Omega_3(t-t_3)} = -\frac{\mathrm{i}}{(\Omega_1+\mathrm{i}\Gamma_1)(\Omega_2+\mathrm{i}\Gamma_2)(\Omega_3+\mathrm{i}\Gamma_3)}. \tag{3.12}$$

It is important to include the convergence terms $\mathrm{i}\Gamma_i$ at this point because terms contribute differently based on their sign as it will be discussed later in section 3.3.

3.2. Derivation of the equation of motion in fourth order

Fourth order processes of a single atom can be described by three Feynman diagrams [96] that are depicted in figure 3.1. While diagram **a** depicts two subsequent second order processes and therefore is reducible, diagrams **b** and **c** are irreducible or genuine fourth order processes. The internal atom dynamics are the dynamics of the operator $\hat{\sigma}_{mn}(t) = |m\rangle\langle n|$ with two arbitrary atomic states $|m\rangle, |n\rangle$.

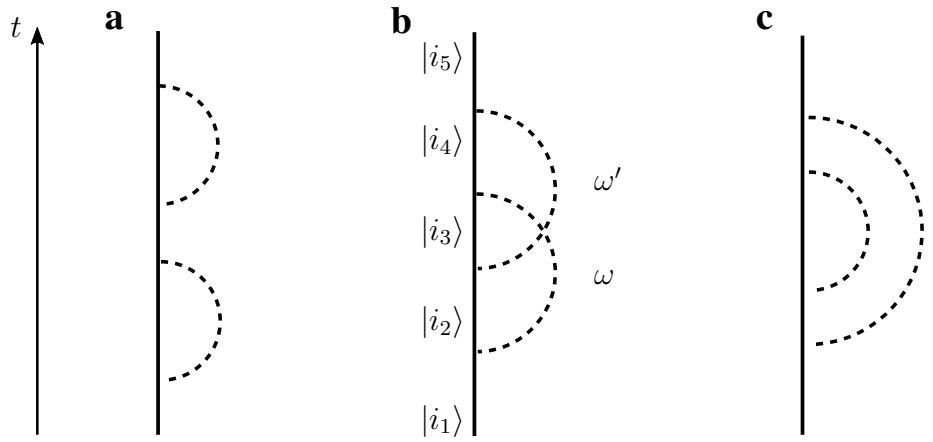

Figure 3.1.: Three contributing Feynman diagrams. Dashed lines represent photons, solid lines the atom. The arrow on the left indicates the direction of time t. Diagram **a** is reducible to two second order processes, diagrams **b** and **c** are irreducible. For diagram **b**, the atomic ket-states starting at $|i_1\rangle$ are given as an example. Every dipole transition is associated with a photon ω or ω' being emitted or absorbed. Every neighbouring pair of states is therefore dipole coupled.

Using the Liouville-Operator $\mathcal{L}(t)\hat{\sigma}_{mn}(t) = \frac{1}{\hbar}\left[\hat{H}(t), \hat{\sigma}_{mn}(t)\right]$, the Heisenberg equation of motion can be written as

$$\dot{\hat{\sigma}}_{mn}(t) = \mathrm{i}\mathcal{L}(t)\hat{\sigma}_{mn}(t) \tag{3.13}$$

with the solution

$$\hat{\sigma}_{mn}(t) = \hat{\sigma}_{mn}(t_0) + \mathrm{i}\int_{t_0}^{t} \mathrm{d}t_1 \mathcal{L}(t_1)\hat{\sigma}_{mn}(t_1). \tag{3.14}$$

The formal solution (3.14) is now inserted into the original equation of motion (3.13) leading to a second order equation

$$\dot{\hat{\sigma}}_{mn}(t) = \mathrm{i}\mathcal{L}(t)\hat{\sigma}_{mn}(t_0) - \int_{t_0}^{t} \mathrm{d}t_1\, \mathcal{L}(t)\mathcal{L}(t_1)\hat{\sigma}_{mn}(t_1). \tag{3.15}$$

Continuing these iteration, the result in fourth order is

$$\begin{aligned}\dot{\hat{\sigma}}_{mn}(t) = &+\mathrm{i}\mathcal{L}(t)\hat{\sigma}_{mn}(t_0) \\ &- \int_{t_0}^{t} \mathrm{d}t_1\, \mathcal{L}(t)\mathcal{L}(t_1)\hat{\sigma}_{mn}(t_0) \\ &- \mathrm{i}\int_{t_0}^{t} \mathrm{d}t_2 \int_{t_0}^{t_2} \mathrm{d}t_1\, \mathcal{L}(t)\mathcal{L}(t_2)\mathcal{L}(t_1)\hat{\sigma}_{mn}(t_0) \\ &+ \int_{t_0}^{t} \mathrm{d}t_3 \int_{t_0}^{t_3} \mathrm{d}t_2 \int_{t_0}^{t_2} \mathrm{d}t_1\, \mathcal{L}(t)\mathcal{L}(t_3)\mathcal{L}(t_2)\mathcal{L}(t_1)\hat{\sigma}_{mn}(t_1).\end{aligned} \tag{3.16}$$

The system consists of atomic and photonic modes. For the equation of motion of the purely atomic operator $\hat{\sigma}_{mn} = |m\rangle\langle n|$ with no background field, one can take the vacuum expectation value using the vacuum photonic state defined by $\hat{\mathbf{f}}|\{0\}\rangle = 0$ which does not affect $\hat{\sigma}_{mn}$. Taking the expectation value in equation (3.16), the odd order terms vanish since $\hat{H}_{AF}$ is linear in $\mathbf{E}(\mathbf{r}, \omega)$ and therefore in $\hat{\mathbf{f}}_\lambda(\mathbf{r}, \omega)$. Then, the equation of motion becomes

$$\begin{aligned}\langle\{0\}|\dot{\hat{\sigma}}_{mn}(t)|\{0\}\rangle = &- \int_{t_0}^{t} \mathrm{d}t_1\, \langle\{0\}|\mathcal{L}(t)\mathcal{L}(t_1)\hat{\sigma}_{mn}(t_0)|\{0\}\rangle \\ &+ \int_{t_0}^{t} \mathrm{d}t_3 \int_{t_0}^{t_3} \mathrm{d}t_2 \int_{t_0}^{t_2} \mathrm{d}t_1\, \langle\{0\}|\mathcal{L}(t)\mathcal{L}(t_3)\mathcal{L}(t_2)\mathcal{L}(t_1)\hat{\sigma}_{mn}(t_1)|\{0\}\rangle.\end{aligned} \tag{3.17}$$

Now, equation (3.17) contains only terms of second and fourth order. However, in the second order term the time argument of $\hat{\sigma}_{mn}$ is t_0 instead of t_1 which is undesirable. This can be fixed by integrating the second order equation (3.15) up to time t_3 and again taking the vacuum

expectation value [97],

$$\langle\{0\}|\hat{\sigma}_{mn}(t_3)|\{0\}\rangle = \langle\{0\}|\hat{\sigma}_{mn}(t_0)|\{0\}\rangle - \int_{t_0}^{t_3} \mathrm{d}t_2 \int_{t_0}^{t_2} \mathrm{d}t_1 \, \langle\{0\}|\mathcal{L}(t_2)\mathcal{L}(t_1)\hat{\sigma}_{mn}(t_1)|\{0\}\rangle \tag{3.18}$$

$$\Rightarrow \langle\{0\}|\hat{\sigma}_{mn}(t_0)|\{0\}\rangle = \langle\{0\}|\hat{\sigma}_{mn}(t_3)|\{0\}\rangle + \int_{t_0}^{t_3} \mathrm{d}t_2 \int_{t_0}^{t_2} \mathrm{d}t_1 \, \langle\{0\}|\mathcal{L}(t_2)\mathcal{L}(t_1)\hat{\sigma}_{mn}(t_1)|\{0\}\rangle. \tag{3.19}$$

At this point, the expectation value can be dropped in terms containing only $\hat{\sigma}_{mn}$ since $\langle\{0\}|\hat{\sigma}_{mn}(t)|\{0\}\rangle = \hat{\sigma}_{mn}(t)$. Now, expression (3.19) can be used for the term $\hat{\sigma}_{mn}(t_0)$ in the fourth order equation (3.17),

$$\dot{\hat{\sigma}}_{mn}(t) = -\int_{t_0}^{t} \mathrm{d}t_1 \, \langle\{0\}|\mathcal{L}(t)\mathcal{L}(t_1)\hat{\sigma}_{mn}(t_1)|\{0\}\rangle \tag{3.20a}$$

$$- \int_{t_0}^{t} \mathrm{d}t_3 \int_{t_0}^{t_3} \mathrm{d}t_2 \int_{t_0}^{t_2} \mathrm{d}t_1 \, \langle\{0\}|\mathcal{L}(t)\mathcal{L}(t_3)\langle\{0\}|\mathcal{L}(t_2)\mathcal{L}(t_1)\hat{\sigma}_{mn}(t_1)|\{0\}\rangle|\{0\}\rangle \tag{3.20b}$$

$$+ \int_{t_0}^{t} \mathrm{d}t_3 \int_{t_0}^{t_3} \mathrm{d}t_2 \int_{t_0}^{t_2} \mathrm{d}t_1 \, \langle\{0\}|\mathcal{L}(t)\mathcal{L}(t_3)\mathcal{L}(t_2)\mathcal{L}(t_1)\hat{\sigma}_{mn}(t_1)|\{0\}\rangle. \tag{3.20c}$$

Here, in term (3.20a) the time argument t_3 was replaced by t_1. This can be justified by the time ordering $t \geq t_3 \geq t_2 \geq t_1 \geq t_0$ which is still obeyed. The third term of the result (3.20) contains now all fourth order contributions including the reducible ones from two second order processes, also depicted in figure 3.1 **a**. These are indeed subtracted via the second term, making the expression (3.20) the sum of pure second order terms and pure fourth order terms. Since the expectation value is taken with respect to the zero photon ground state $|\{0\}\rangle$, all terms involving $\hat{\mathbf{E}}^{(\dagger)}$, i.e. $\hat{\mathbf{f}}^{(\dagger)}$, vanish.

The evaluation of equation (3.20) is lengthy but straightforward. Details are shown in appendix B.1 with the final purely fourth order result equation (B.4). Term (3.20a) consists of only 4 summands, term (3.20b) of 32 and term (3.20c) of 64. As term (3.20b) is subtracted from (3.20c), a total of 36 terms, 4 in second order and 32 in fourth order, remain. The 32 fourth order terms are represented in the diagrams in figure 3.1 **b** and **c**. From this structure, one can draw useful conclusions for the derivation. Since in (3.20b) the vacuum expectation value is taken both after second order and fourth order, it contains all terms where no $\hat{\mathbf{E}}^{(\dagger)}$ are present after second order. Conversely, all relevant terms for the pure fourth order contribution do contain 2 factors $\hat{\mathbf{E}}^{(\dagger)}(\omega)$ and $\hat{\mathbf{E}}^{(\dagger)}(\omega')$ after second order perturbation theory. Equation 3.20 is a generic result for atomic operator $\hat{\sigma}_{mn}(t)$. Specific systems can be modeled by choosing

the according atomic energy states $|m\rangle$ and $|n\rangle$, the respective transition frequencies ω_{mn} and by the choice of the according Liouville operator $\mathcal{L}(t)$ including the specific scattering Green's tensor $\boldsymbol{G}(\omega) \equiv \boldsymbol{G}^{(1)}(\mathbf{r}, \mathbf{r}, \omega)$ to describe the magnetoelectric environment.

3.3. The symmetric Λ-system in front of a dielectric half space

In this section, a Λ-system consisting of two energetically degenerate ground states $|m\rangle, |n\rangle$ and one intermediate state $|k\rangle$ is considered. As an example, a ^{87}Rb atom as in [92] with one specific intermediate state $|k\rangle$ is chosen. An exemplary set of state is

$$|m\rangle = |5^2S_{1/2}, F = 2, m_F = -1\rangle, \tag{3.21}$$

$$|n\rangle = |5^2S_{1/2}, F = 2, m_F = +1\rangle, \tag{3.22}$$

$$|k\rangle = |5^2P_{3/2}, F = 3, m_F = 0\rangle, \tag{3.23}$$

where the energetic hyperfine splitting of the ground states is neglected. The system is shown schematically in figure 3.2.

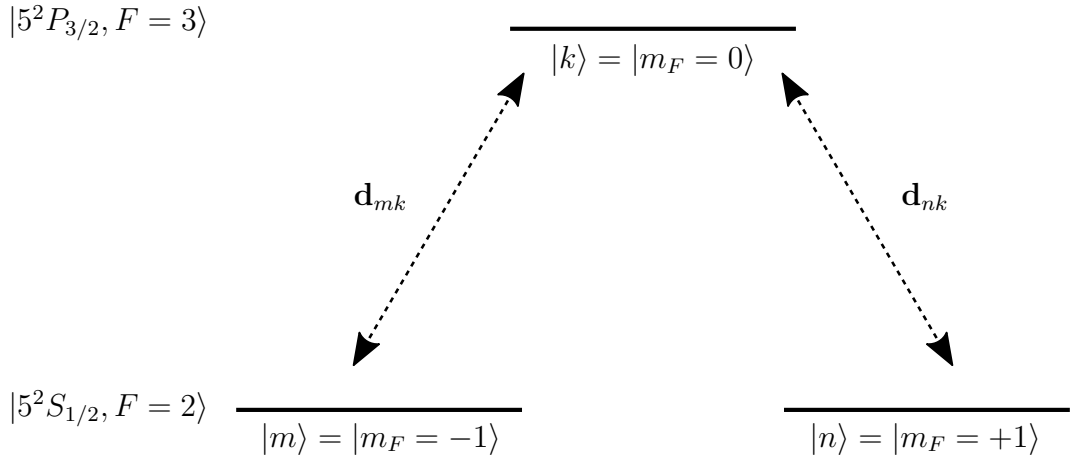

Figure 3.2.: The Λ-system. The states $|m\rangle$ and $|n\rangle$ are hyperfine ground states of ^{87}Rb. For simplicity, the energy difference between $|m\rangle$ and $|n\rangle$ is neglected. State $|k\rangle$ is one excited state from the $D_2(|5^2S_{1_2}\rangle \rightarrow |5^2P_{3/2}\rangle)$-line.

Now, it is possible to calculate a system of differential equations of the form (B.4) for the atomic operators $\hat{\sigma}_{mn}(t), \hat{\sigma}_{nn}(t), \hat{\sigma}_{nn}(t)$ and $\hat{\sigma}_{nm}(t)$. The system of the form $\dot{\hat{\boldsymbol{\sigma}}} = \boldsymbol{A} \cdot \hat{\boldsymbol{\sigma}}$ is

given by

$$\begin{pmatrix} \dot{\hat{\sigma}}_{mn}(t) \\ \dot{\hat{\sigma}}_{nn}(t) \\ \dot{\hat{\sigma}}_{mm}(t) \\ \dot{\hat{\sigma}}_{nm}(t) \end{pmatrix} = \begin{pmatrix} 0 & a_{1,nn} & a_{1,mm} & 0 \\ a_{2,mn} & 0 & 0 & a_{2,nm} \\ a_{3,mn} & 0 & 0 & a_{3,nm} \\ 0 & a_{4,nn} & a_{4,mm} & 0 \end{pmatrix} \cdot \begin{pmatrix} \hat{\sigma}_{mn}(t) \\ \hat{\sigma}_{nn}(t) \\ \hat{\sigma}_{mm}(t) \\ \hat{\sigma}_{nm}(t) \end{pmatrix}. \tag{3.24}$$

Here, two points are noteworthy. Firstly, there are no inhomogeneities in the system as external fields are neglected. And secondly, the pure fourth order equations do not contain any diagonal elements. From the equations of motion, one finds terms of the following structure:

$$\begin{aligned} a_{1,nn} = -\mathrm{i}\left(\frac{\mu_0}{\pi\hbar}\right)^2 \int_0^\infty \mathrm{d}\omega \int_0^\infty \mathrm{d}\omega' \Big\{ & \omega^2\omega'^2 \\ & \times \left[\mathbf{d}_{nk}\cdot \mathrm{Im}\boldsymbol{G}(\omega)\cdot\mathbf{d}_{km}\mathbf{d}_{km}\cdot\mathrm{Im}\boldsymbol{G}(\omega')\cdot\mathbf{d}_{mk} + \mathbf{d}_{nk}\cdot\mathrm{Im}\boldsymbol{G}(\omega)\cdot\mathbf{d}_{km}\mathbf{d}_{kn}\cdot\mathrm{Im}\boldsymbol{G}(\omega')\cdot\mathbf{d}_{nk}\right] \\ & \times \left[\frac{1}{(\omega'+\omega_{km})} + \frac{1}{(\omega-\omega_{km})}\right]\frac{1}{(\omega-\omega_{km})(\omega+\omega')}\Big\}. \end{aligned} \tag{3.25}$$

It is also important to notice, that both the system of differential equations (3.24) as well as some of the integral terms similar to (3.25) become significantly more complicated when the ground states are not degenerate and $\omega_{nm} \neq 0$. Choosing the quantization axis along $\mathbf{e}_x$, the dipole operator $\hat{\mathbf{d}}$ is $\hat{\mathbf{d}} = \hat{d}_0\mathbf{e}_x + \left(\hat{d}_- - \hat{d}_+\right)/\sqrt{2}\mathbf{e}_y + \mathrm{i}\left(\hat{d}_- + \hat{d}_+\right)/\sqrt{2}\mathbf{e}_z$ and $\mathbf{d}_{ij} = \langle i|\hat{\mathbf{d}}|j\rangle$ [92]. In this basis, one finds

$$\begin{aligned} \mathbf{d}_{ki}\cdot\boldsymbol{G}(\omega)\cdot\mathbf{d}_{jk} = {} & G_{xx}\langle k|\hat{d}_0|i\rangle\langle k|\hat{d}_0|j\rangle \\ & + (G_{zz}-G_{yy})\left(\langle k|\hat{d}_+|i\rangle\langle k|\hat{d}_-|j\rangle + \langle k|\hat{d}_-|i\rangle\langle k|\hat{d}_+|j\rangle\right)/2 \\ & + (G_{zz}+G_{yy})\left(\langle k|\hat{d}_+|i\rangle\langle k|\hat{d}_+|j\rangle + \langle k|\hat{d}_-|i\rangle\langle k|\hat{d}_-|j\rangle\right)/2. \end{aligned} \tag{3.26}$$

Here, i and j are any of the ground states m and n. For $i = j$, only terms $\sim (G_{zz} + G_{yy})$ are non-zero and for $i \neq j$, terms $\sim (G_{zz} + G_{yy})$ have to be considered. In the system under consideration, it follows from equation (3.26) that $\mathbf{d}_{mk}\cdot\mathrm{Im}\boldsymbol{G}(\omega)\cdot\mathbf{d}_{kn} = \mathbf{d}_{nk}\cdot\mathrm{Im}\boldsymbol{G}(\omega)\cdot\mathbf{d}_{km}$. For the solution of the time integral (3.12), a small imaginary part $+\mathrm{i}\Gamma_i$ was introduced in equation (3.11) and has to be considered when evaluating the integrals in equation (3.25). In order to solve the integrals in equation (3.25), the frequencies are chosen with a positive sign in the denominator so that $(-\omega + \omega_{km} + \mathrm{i}\Gamma)^{-1} = -(\omega - \omega_{km} - \mathrm{i}\Gamma)^{-1}$ is commonly used.

According to the Sokhotski-Plemelj theorem,

$$\int_0^\infty \mathrm{d}x\, \frac{f(x)}{x \pm \mathrm{i}\Gamma} = \mathcal{P}\int_0^\infty \mathrm{d}x\, \frac{f(x)}{x} \mp \mathrm{i}\pi f(0), \tag{3.27}$$

the change of sign of the imaginary part in the denominator leads to the complex conjugate result after integration. In equation (3.27) $\mathcal{P}$ denotes the Cauchy principal value. Hence, the matrix in equation (3.24) may be rewritten as

$$\boldsymbol{A} = \begin{pmatrix} 0 & a & a^* & 0 \\ a & 0 & 0 & a^* \\ -a & 0 & 0 & -a^* \\ 0 & a^* & a & 0 \end{pmatrix}, \tag{3.28}$$

with $a \equiv a_{1,nn}$. The eigenvalues of $\boldsymbol{A}$ are $\lambda_{1,2} = \pm 2\mathrm{i}\mathrm{Im}a$ and $\lambda_3 = 0$. Therefore, the system does not decay and harmonic oscillations with a constant offset can be expected. The eigenfrequencies of the system are $\Omega_\mathrm{R} = |\lambda_1| = 2|\mathrm{Im}(a)|$.

In order to evaluate a, additional information about the chosen system becomes necessary. Data for the ^{87}Rb-atom can be found in [98]. The transition frequency from the $|5^2S_{1/2}\rangle$ ground state to the $|5^2P_{3/2}\rangle$ excited state is $\omega_{km} = \omega_{kn} = 2\pi \cdot 384.230\,\mathrm{THz}$. The transition dipole moment can be decomposed into a radial part $d_{J=1/2,J'=3/2} = \langle J = 1/2||er||J' = 3/2\rangle = 3.584 \times 10^{-29}\,\mathrm{C}\cdot\mathrm{m}$ and the hyperfine angular dipole matrix elements,

$$\langle F = 2, m_F = -1|d_+|F = 3, m_F = 0\rangle = \sqrt{\frac{1}{10}} \tag{3.29}$$

$$\langle F = 2, m_F = +1|d_-|F = 3, m_F = 0\rangle = \sqrt{\frac{1}{10}}. \tag{3.30}$$

Since the angular dipole matrix elements (3.29) and (3.30) are identical, one finds also $\mathbf{d}_{kn} \cdot \mathrm{Im}\boldsymbol{G}(\omega) \cdot \mathbf{d}_{nk} = \mathbf{d}_{km} \cdot \mathrm{Im}\boldsymbol{G}(\omega) \cdot \mathbf{d}_{mk}$. The scattering Green's tensor for an infinite dielectric plate with permittivity $\varepsilon(\omega)$ for an atom at distance z from the surface is given in equation (A.16) and may be split into a frequency dependent and a frequency independent part according to

$$\boldsymbol{G}^{(1)}(\mathbf{r}, \mathbf{r}', \omega) = G(\mathbf{r}, \mathbf{r}', \omega)\tilde{\boldsymbol{G}}. \tag{3.31}$$

Here, $\tilde{\boldsymbol{G}} = \mathrm{diag}(1,1,2)$. This way, one can split the evaluation of a from equation (3.25) into separate factors. The dipole transition moments in the coefficients can be calculated as

$$\left(\mathbf{d}_{mk}\cdot\tilde{\boldsymbol{G}}\cdot\mathbf{d}_{kn}\right)\left(\mathbf{d}_{km}\cdot\tilde{\boldsymbol{G}}\cdot\mathbf{d}_{mk}\right) = \left(\mathbf{d}_{mk}\cdot\tilde{\boldsymbol{G}}\cdot\mathbf{d}_{kn}\right)\left(\mathbf{d}_{kn}\cdot\tilde{\boldsymbol{G}}\cdot\mathbf{d}_{nk}\right) \tag{3.32}$$

$$= \left(\frac{\tilde{G}_{zz}-\tilde{G}_{yy}}{2}\right)\left(\frac{\tilde{G}_{zz}+\tilde{G}_{yy}}{2}\right) \times \left(\sqrt{\frac{1}{10}}\, d_{J=1/2,J'=3/2}\right)^4 \tag{3.33}$$

$$= \frac{3}{400}\left(d_{J=1/2,J'=3/2}\right)^4. \tag{3.34}$$

The frequency integrals in (3.25) possess poles at $\omega = \omega_{km}$ and can be solved using contour integration techniques up to a point where the remaining integral can be integrated numerically. Detailed calculations are presented in appendix B.2. Using the scattering Green's tensor (A.16), the evaluated dipole moments (3.34) as well as the frequency integrals (B.12) and (B.20), the coefficient a from equation (3.25) can be numerically calculated for given material parameters and surface distance d. It is important to note that due to the product of two Green's tensors in equation (3.25), the parameter a and, thus, the eigenfrequency of the system depends on the sixth power of the surface distance, $\Omega_{\mathrm{Rabi}} \sim d^{-6}$. The dielectric surface is modeled with a Drude model permittivity

$$\varepsilon(\omega) = 1 + \frac{\omega_{\mathrm{P}}^2}{\omega(\omega+\mathrm{i}\gamma)} \tag{3.35}$$

with plasma frequency ω_{P} and damping constant γ. For platinum, the material parameters are $\omega_{\mathrm{P}} = 7.75\times10^{15}\,\mathrm{rad/s}$ and $\gamma = 1.04\times10^{14}\,\mathrm{rad/s}$ [99]. One finds $a(d = 40\,\mathrm{nm}) \approx (2.46\times10^{-3} + 5.64\times10^{-2}\mathrm{i})\,\mathrm{rad/s}$ and, thus, $\Omega_{\mathrm{Rabi}} = 2\mathrm{Im}\,a \approx 113\times10^{-3}\,\mathrm{rad/s}$. The resulting time evolution is plotted in figure 3.3.

The period of the oscillation is $\tau \approx 55.7\,\mathrm{s}$ and the corresponding Rabi frequency is $\Omega_{\mathrm{Rabi}} \approx 113\times10^{-3}\,\mathrm{rad/s}$. In table (3.1), Ω_{Rabi} is listed for a range of materials. The maximum frequency is calculated for an iron surface to be $\Omega_{\mathrm{Rabi}} = 217\,\mathrm{mrad/s}$. This is approximately by a factor 30 smaller than the second order Rabi frequency calculated for a perfect conductor [92].

In conclusion, small Rabi frequencies could be found for a ground state ^{87}Rb atom in front of a plain dielectric plate. These frequencies are typically of the order of $100\times10^{-3}\,\mathrm{rad}/s$ for an atom surface distance of $d = 40\,\mathrm{nm}$. This is about a factor 30 to 60 lower than what is expected

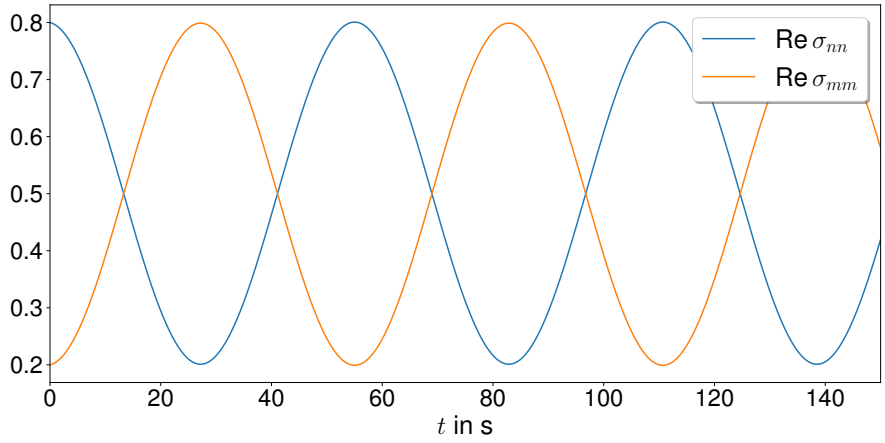

Figure 3.3.: The real parts of $\hat{\sigma}_{nn}$ and $\hat{\sigma}_{mm}$ are plotted over time. Parameters for the Green's tensor are for platinum. Surface distance is $d = 40\,\mathrm{nm}$. Starting point is $\vec{\hat{\sigma}}(0) = (0, 0.8\hat{\sigma}_{nn}, 0.2\hat{\sigma}_{mm}, 0)^T$. The oscillation between states has a frequency $\Omega_{\mathrm{Rabi}} \approx 113 \times 10^{-3}\,\mathrm{rad/s}$. Because of the purely imaginary eigenvalues of (3.24), no state can be higher populated than the highest population at $t = 0$.

Material	ω_{P} (rad/s)	γ (rad/s)	$\Omega_{\mathrm{Rabi}}(z = 40\,\mathrm{nm}) \times 10^3$ (rad/s)
Au	1.37×10^{16}	4.12×10^{13}	34.1
Al	2.25×10^{16}	1.22×10^{14}	15.4
Pd	8.36×10^{15}	2.16×10^{13}	93.7
Ag	5.77×10^{15}	1.15×10^{13}	287
Cu	1.12×10^{16}	4.41×10^{13}	49.8
Mo	1.14×10^{16}	7.86×10^{13}	48.1
Fe	6.23×10^{15}	2.79×10^{13}	217
Co	1.18×10^{16}	1.07×10^{14}	44.8
W	9.72×10^{15}	8.53×10^{13}	66.5
Ni	7.44×10^{15}	6.53×10^{13}	127
Pt	7.75×10^{15}	1.04×10^{14}	113

Table 3.1.: Fourth order Rabi frequencies Ω_{Rabi} of the ^{87}Rb atom at a distance $d = 40\,\mathrm{nm}$ from a surface. Material parameters ω_{P} and γ for the Drude model (3.35) can be found in [99].

from second order perturbation theory [92]. Thus, these fourth order effects may only play a role in extreme precision experiments. No spontaneous decay was assumed for the excited state and the Casimir-Polder interaction does not induce a decay in fourth order perturbation theory for the symmetric Λ-system. However, since the calculations were shown in detail for

the general fourth order equation (3.20) and a general result for an atomic operator $\hat{\sigma}_{mn}(t)$ was presented in equation (B.4), the foundations have been established for more complex systems. Among the most obvious more complex systems are excited atoms with a limited natural lifetime that can be modeled by a different transition frequency ω_{km} and a finite linewidth Γ_{km}. In fact, if one assumes the decay of the excited states to the ground states with a finite rate γ, the oscillation between states become weaker over time and level out [100]. Another interesting aspect to study would be the influence of a corrugated surface modeled by the respective scattering Green's tensor $\boldsymbol{G}^{(1)}(\mathbf{r}_A, \mathbf{r}_A, \omega)$ since this is the origin of the contactless rack and pinion [93]. A third addition could be the inclusion of a non-vanishing background field, e.g. through thermal excitations. That way, the expectation value in equation (3.20) would not have to be taken with respect to the vacuum field $|\{0\}\rangle$ but to some field with a finite photon number. This would also lead to additional Feynman diagrams in figure 3.1 with external lines indicating background (thermal) photons.

Chapter 4.

van der Waals interactions between Rydberg atoms

The focus of this chapter is on the van der Waals interactions between Rydberg atoms. It is well established, that the van der Waals potential (2.122) in the nonretarded limit takes the form

$$U_{\mathrm{vdW}}(r) = -\frac{C_6}{r^6}, \tag{4.1}$$

where r is the interparticle distance and C_6 is a coefficient containing all of the particles' relevant dipole transitions. There are two reasons that the potential (4.1) plays a dominant role in Rydberg atomic interactions. The nonretarded limit, i.e. the small distance limit, is fulfilled whenever the interatomic distance r is small compared to c/ω_{t},

$$r \ll \frac{c}{\omega_{\mathrm{t}}}, \tag{4.2}$$

for all relevant transition frequencies ω_{t}. Due to the close energetic spacing of adjacent Rydberg levels, (4.2) is fulfilled regularly by Rydberg atoms. The second reason is that C_6 scales with main quantum number n^{11} [19]. Naturally, for large n as they appear in Rydberg atoms C_6 reaches large values. As a consequence the van der Waals interaction between Rydberg atoms is very pronounced and has drawn the attention among the Rydberg atomic community [101–104].

This chapter is organized as follows. First, the nonretarded van der Waals interaction between excited atoms is discussed in the perturbative regime. It can be shown that for two atoms near a perfectly conducting plate both the Green's tensor and the potentials simplify significantly. As a consequence, the interaction potential between the atoms is strongly dependent on the atoms' orientation with respect to the surface [105]. In the next step, the dipole-dipole interaction Hamiltonian is extended to include multipole moments up to quadrupoles to account

higher order terms that play a role for Rydberg atoms due to the large extend of the radial wave function. Because of the complex energy level structure of Rydberg atoms, the perturbative approach is bound to fail for close distances and exact diagonalization has to be applied. In this case, the two-atom interaction between two ^{87}Rb atoms is reduced compared to the free-space potential [105]. Finally, the one atom Casimir-Polder potential is included in the Hamiltonian as well. This causes the appearance of new potential wells in the atomic pair potential that are associated with Rydberg macrodimers. A large number of closely spaced vibrational states with radial wave functions in the μm-range can be found for these molecules [106].

4.1. Nonretarded van der Waals interaction for excited atoms in the perturbative regime

For excited atoms, it is often feasible to in apply the nonretarded limit because the condition (4.2) is often fulfilled for the small transition frequencies between adjacent excited states. Two atoms A and B in their respective energy eigenstates $|k\rangle_A$ and $|l\rangle_B$ are subject to the van der Waals interaction potential that can be derived via fourth order perturbation theory as [29]

$$\begin{aligned} &U_{\mathrm{vdW}}(\mathbf{r}_A, \mathbf{r}_B) \\ &= \mathrm{i}\frac{\mu_0^2}{\hbar\pi} \sum_{m\neq k, n\neq l} \frac{1}{\omega_{A,mk} + \omega_{B,nl}} \\ &\quad \times \left\{ \left[\mathcal{P}\int_0^\infty \mathrm{d}\omega, \frac{\omega^4 \left(\omega_{A,mk} + \omega_{B,nl} + \omega\right)}{\left(\omega + \omega_{A,mk}\right)\left(\omega + \omega_{B,nl}\right)} + \mathcal{P}\int_0^{-\infty} \mathrm{d}\omega \, \frac{\omega^4 \left(\omega_{A,mk} + \omega_{B,nl} - \omega\right)}{\left(\omega - \omega_{A,mk}\right)\left(\omega - \omega_{B,nl}\right)} \right] \right. \\ &\quad \left. \times \left[\mathbf{d}_{A,km} \cdot \boldsymbol{G}(\mathbf{r}_A, \mathbf{r}_B, \omega) \cdot \mathbf{d}_{B,ln}\right]^2 \right\}. \end{aligned} \tag{4.3}$$

Here, the $\omega_{i,pq} = \omega_{i,p} - \omega_{i,q}$ and $\mathbf{d}_{i,qp} =_i \langle q|\hat{\mathbf{d}}_i|p\rangle_i$ are the transition frequency and the transition dipole moments between states $|q\rangle_i$ and $|p\rangle_i$ of atom i. $\mathcal{P}$ indicates the Cauchy principal value integral. For nonretarded interactions the zero-frequency, i.e. static, contributions to equation (4.3) dominate and in that limit the Green's tensor $\boldsymbol{G}(\mathbf{r}_A, \mathbf{r}_B, \omega)$ becomes

$$\boldsymbol{G}_0(\mathbf{r}_A, \mathbf{r}_B) = \lim_{\omega\to 0} \frac{\omega^2}{c^2} \boldsymbol{G}(\mathbf{r}_A, \mathbf{r}_B, \omega). \tag{4.4}$$

Using the frequency-independent static Green's tensor $\boldsymbol{G}_0(\mathbf{r}_A, \mathbf{r}_B)$ the potential (4.3) becomes

$$\begin{aligned} U_{\mathrm{vdW}}(\mathbf{r}_A, \mathbf{r}_B) = \mathrm{i}\frac{1}{\hbar\pi\varepsilon_0^2} \sum_{m\neq k, n\neq l} \frac{\left[\mathbf{d}_{A,km} \cdot \boldsymbol{G}_0(\mathbf{r}_A, \mathbf{r}_B) \cdot \mathbf{d}_{B,ln}\right]^2}{\omega_{A,mk} + \omega_{B,nl}} \\ \times \left[\mathcal{P}\int_0^\infty \mathrm{d}\omega, \frac{\omega_{A,mk} + \omega_{B,nl} + \omega}{(\omega + \omega_{A,mk})\,(\omega + \omega_{B,nl})}\right. \\ \left. + \mathcal{P}\int_0^{-\infty} \mathrm{d}\omega\, \frac{\omega_{A,mk} + \omega_{B,nl} - \omega}{(\omega - \omega_{A,mk})\,(\omega - \omega_{B,nl})}\right]. \end{aligned} \tag{4.5}$$

The sum $\sum_{m\neq k,n\neq l}$ runs over all atomic states m, n. Therefore, there are four contributions that can be distinguished as depicted in figure 4.1.

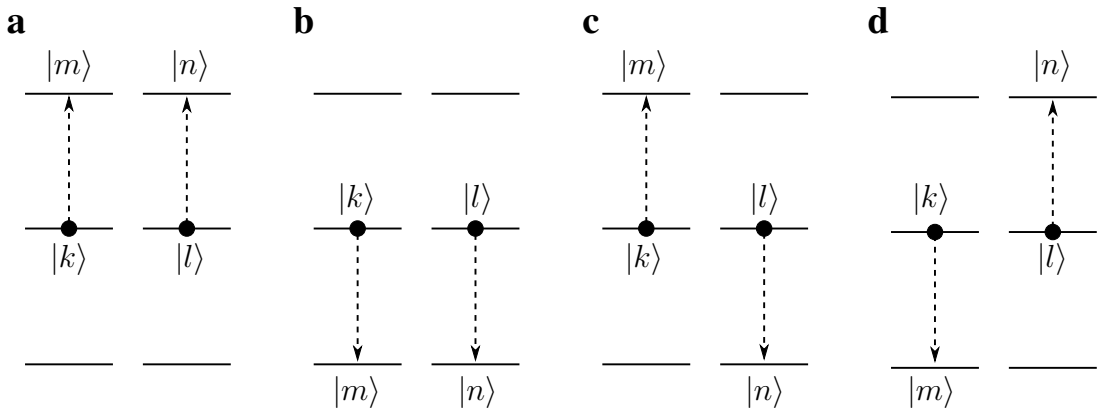

Figure 4.1.: The four different cases of transitions to upper and lower states of the sum in (4.5). The black dot represents the electron in the atomic states $|k\rangle$ and $|l\rangle$ and the dashed arrows indicate the upward and downward transitions to states $|m\rangle$ and $|n\rangle$.

In the first case, only upward transitions are considered ($m > k$ and $n > l$) so that $\omega_{A,mk}$ and $\omega_{B,lm}$ are strictly positive, cf. figure 4.1 **a**. Now, the same contour integration techniques are applied as in section B.2. Since there are no poles on the real axis, the integration can be flipped to the imaginary axis,

$$\mathcal{P}\int_0^\infty \mathrm{d}\omega\, \frac{\omega_{A,mk} + \omega_{B,nl} + \omega}{(\omega + \omega_{A,mk})\,(\omega + \omega_{B,nl})} = \mathrm{i}\int_0^\infty \mathrm{d}\xi\, \frac{\omega_{A,mk} + \omega_{B,nl} + \mathrm{i}\xi}{(\mathrm{i}\xi + \omega_{A,mk})\,(\mathrm{i}\xi + \omega_{B,nl})}, \tag{4.6}$$

$$\mathcal{P}\int_0^{-\infty} \mathrm{d}\omega\, \frac{\omega_{A,mk} + \omega_{B,nl} - \omega}{(\omega - \omega_{A,mk})\,(\omega - \omega_{B,nl})} = \mathrm{i}\int_0^\infty \mathrm{d}\xi, \frac{\omega_{A,mk} + \omega_{B,nl} - \mathrm{i}\xi}{(\mathrm{i}\xi - \omega_{A,mk})\,(\mathrm{i}\xi - \omega_{B,nl})}. \tag{4.7}$$

Therefore, the sum of these integrals can be written as

$$\begin{aligned}
&\mathcal{P}\int_0^\infty \mathrm{d}\omega\, \frac{\omega_{A,mk}+\omega_{B,nl}+\omega}{(\omega+\omega_{A,mk})\,(\omega+\omega_{B,nl})} + \mathcal{P}\int_0^{-\infty} \mathrm{d}\omega\, \frac{\omega_{A,mk}+\omega_{B,nl}-\omega}{(\omega-\omega_{A,mk})\,(\omega-\omega_{B,nl})} \\
&= \mathrm{i}\int_0^\infty \mathrm{d}\xi\, 2\mathrm{Re}\left(\frac{\omega_{A,mk}+\omega_{B,nl}+\omega}{(\omega+\omega_{A,mk})\,(\omega+\omega_{B,nl})}\right) \\
&= \mathrm{i}2\,(\omega_{A,mk}+\omega_{B,nl})\,\omega_{A,mk}\omega_{B,nl}\int_0^\infty \mathrm{d}\xi\, \frac{1}{\left(\xi^2+\omega_{A,mk}^2\right)\left(\xi^2+\omega_{B,nl}^2\right)} \\
&= \mathrm{i}\pi.
\end{aligned} \tag{4.8}$$

The second case features purely downward transitions, i.e. $m < k$ and $n < l$ as shown in figure4.1 **b**, and the integral has poles on the real axis at $\omega = \mp\omega_{A,mk} = \pm\omega_{A,km}$ and $\omega = \mp\omega_{B,nl} = \pm\omega_{B,ln}$. Therefore, the residues at those poles have to be considered. Again, with contour integration one arrives at

$$\begin{aligned}
\mathcal{P}\int_0^\infty \mathrm{d}\omega\, \frac{\omega_{A,mk}+\omega_{B,nl}+\omega}{(\omega+\omega_{A,mk})\,(\omega+\omega_{B,nl})} &= -\mathcal{P}\int_0^\infty \mathrm{d}\omega\, \frac{\omega_{A,km}+\omega_{B,km}-\omega}{(\omega-\omega_{A,km})\,(\omega-\omega_{B,ln})} \\
&= -\mathrm{i}\int_0^\infty \mathrm{d}\xi\, \frac{\omega_{A,km}+\omega_{B,km}-\mathrm{i}\xi}{(\mathrm{i}\xi-\omega_{A,km})\,(\mathrm{i}\xi-\omega_{B,ln})} \\
&\quad -\mathrm{i}\pi\frac{\omega_{B,km}}{\omega_{A,km}-\omega_{B,ln}} - \mathrm{i}\pi\frac{\omega_{A,km}}{\omega_{B,km}-\omega_{A,km}}. \\
&= -\mathrm{i}\int_0^\infty \mathrm{d}\xi\, \frac{\omega_{A,km}+\omega_{B,km}-\mathrm{i}\xi}{(\mathrm{i}\xi-\omega_{A,km})\,(\mathrm{i}\xi-\omega_{B,ln})} + \mathrm{i}\pi
\end{aligned} \tag{4.9}$$

In the same way, the second principal value integral can be transformed according to

$$\begin{aligned}
\mathcal{P}\int_0^{-\infty} \mathrm{d}\omega\, \frac{\omega_{A,mk}+\omega_{B,mk}-\omega}{(\omega-\omega_{A,mk})\,(\omega-\omega_{B,nl})} &= -\mathcal{P}\int_0^{-\infty} \mathrm{d}\omega\, \frac{\omega_{A,km}+\omega_{B,ln}+\omega}{(\omega+\omega_{A,km})\,(\omega+\omega_{B,km})} \\
&= -\mathrm{i}\int_0^\infty \mathrm{d}\xi\, \frac{\omega_{A,km}+\omega_{B,ln}+\mathrm{i}\xi}{(\mathrm{i}\xi+\omega_{A,km})\,(\mathrm{i}\xi+\omega_{B,km})} \\
&\quad +\mathrm{i}\pi\frac{\omega_{B,ln}}{-\omega_{A,km}+\omega_{B,ln}} + \mathrm{i}\pi\frac{\omega_{A,km}}{-\omega_{B,ln}+\omega_{A,km}} \\
&= -\mathrm{i}\int_0^\infty \mathrm{d}\xi\, \frac{\omega_{A,km}+\omega_{B,ln}+\mathrm{i}\xi}{(\mathrm{i}\xi+\omega_{A,km})\,(\mathrm{i}\xi+\omega_{B,km})} + \mathrm{i}\pi.
\end{aligned} \tag{4.10}$$

Thus, the sum of (4.9) and (4.10) is

$$\begin{aligned}
&\mathcal{P}\int_0^\infty \mathrm{d}\omega\, \frac{\omega_{A,mk}+\omega_{B,nl}+\omega}{(\omega+\omega_{A,mk})\,(\omega+\omega_{B,nl})} + \mathcal{P}\int_0^{-\infty} \mathrm{d}\omega\, \frac{\omega_{A,mk}+\omega_{B,mk}-\omega}{(\omega-\omega_{A,mk})\,(\omega-\omega_{B,nl})} \\
&= -\mathrm{i}\pi + 2\mathrm{i}\pi \\
&= \mathrm{i}\pi.
\end{aligned} \tag{4.11}$$

The third case of downward transitions for one atom and upward transitions for the other atom can be treated similarly. The two distinct cases are pictured in figure 4.1 **c** and **d**. Regardless of which atom undergoes the upward or downward transition, the sum of the two principal value integrals is $\mathrm{i}\pi$. The situation where A undergoes a downward transition and B an upward transition, i.e. $m < k$ and $n > l$, is discussed here. The first integral is

$$\begin{aligned}\mathcal{P}\int_0^\infty \mathrm{d}\omega\, \frac{\omega_{A,mk}+\omega_{B,nl}+\omega}{(\omega+\omega_{A,mk})\,(\omega+\omega_{B,nl})} &= \mathcal{P}\int_0^\infty \mathrm{d}\omega\, \frac{-\omega_{A,km}+\omega_{B,nl}+\omega}{(\omega-\omega_{A,km})(\omega+\omega_{B,nl})} \\ &= \mathrm{i}\int_0^\infty \mathrm{d}\xi\, \frac{-\omega_{A,km}+\omega_{B,nl}+\mathrm{i}\xi}{(\mathrm{i}\xi-\omega_{A,km})(\mathrm{i}\xi+\omega_{B,nl})} \\ &\quad + \mathrm{i}\pi\frac{\omega_{B,nl}}{\omega_{A,km}+\omega_{B,nl}},\end{aligned} \tag{4.12}$$

and similarly the second integral becomes

$$\begin{aligned}\mathcal{P}\int_0^{-\infty} \mathrm{d}\omega\, \frac{\omega_{A,mk}+\omega_{B,nl}-\omega}{(\omega+\omega_{A,mk})(\omega+\omega_{B,nl})} &= \mathcal{P}\int_0^{-\infty} \mathrm{d}\omega\, \frac{-\omega_{A,km}+\omega_{B,nl}-\omega}{(\omega-\omega_{A,km})(\omega+\omega_{B,nl})} \\ &= \mathrm{i}\int_0^\infty \mathrm{d}\xi\, \frac{-\omega_{A,km}+\omega_{B,nl}-\mathrm{i}\xi}{(\mathrm{i}\xi-\omega_{A,km})(\mathrm{i}\xi+\omega_{B,nl})} \\ &\quad + \mathrm{i}\pi\frac{\omega_{B,nl}}{\omega_{A,km}+\omega_{B,nl}}.\end{aligned} \tag{4.13}$$

The sum of (4.12) and (4.13) can be evaluated using the integral

$$\int_0^\infty \mathrm{d}x\, \frac{x^2}{(x^2+a^2)\,(x^2+b^2)} = \frac{\pi}{2(a+b)}. \tag{4.14}$$

Now, it is straightforward to show that

$$\begin{aligned}&\mathcal{P}\int_0^\infty \mathrm{d}\omega\, \frac{\omega_{A,mk}+\omega_{B,nl}+\omega}{(\omega+\omega_{A,mk})\,(\omega+\omega_{B,nl})} + \mathcal{P}\int_0^{-\infty} \mathrm{d}\omega\, \frac{\omega_{A,mk}+\omega_{B,nl}-\omega}{(\omega+\omega_{A,mk})(\omega+\omega_{B,nl})} \\ &= \mathrm{i}\pi\frac{\omega_{A,km}-\omega_{B,nl}}{\omega_{A,km}+\omega_{B,nl}} + 2\mathrm{i}\pi\frac{\omega_{B,nl}}{\omega_{A,km}+\omega_{B,nl}} \\ &= \mathrm{i}\pi.\end{aligned} \tag{4.15}$$

Naturally, the same arguments hold for an upward transition of A and a downward transition of B. Therefore, the frequency integrals in the potential (4.5) can all be carried out analytically and the potential becomes

$$U_{\mathrm{vdW}}(\mathbf{r}_A,\mathbf{r}_B) = -\frac{1}{\hbar\varepsilon_0^2}\sum_{m\neq k,n\neq l}\frac{\left[\mathbf{d}_{A,km}\cdot\boldsymbol{G}_0(\mathbf{r}_A,\mathbf{r}_B)\cdot\mathbf{d}_{B,nl}\right]^2}{\omega_{A,mk}+\omega_{B,nl}}. \tag{4.16}$$

With the nonretarded vacuum Green's tensor (A.10), the potential becomes

$$\begin{aligned} U_{\mathrm{vdW}}^{\mathrm{vac}}(\mathbf{r}_A, \mathbf{r}_B) &= -\frac{1}{(4\pi)^2 \hbar \varepsilon_0^2 r^6} \sum_{m \neq k, n \neq l} \frac{\left[\mathbf{d}_{A,km} \cdot \mathbf{d}_{B,nl} - 3(\mathbf{d}_{A,km} \cdot \mathbf{e}_{\mathbf{r}})(\mathbf{d}_{B,nl} \cdot \mathbf{e}_{\mathbf{r}})\right]^2}{\omega_{A,mk} + \omega_{B,nl}}, \\ &= -\frac{C_6}{r^6}. \end{aligned} \tag{4.17}$$

where $\mathbf{r} = \mathbf{r}_A - \mathbf{r}_B$, $r = |\mathbf{r}|$ and $\mathbf{e}_{\mathbf{r}} = \mathbf{r}/r$. Summarizing all constants and atom-specific variables by the atom-specific C_6 coefficient the potential shows the expected famous r^{-6} dependence of the nonretarded van der Waals potential. As it was shown, an explicit distinction between the non-resonant (integral) and resonant (residue) terms is not feasible in this limit.

Equation (4.16) can be simplified further when considering isotropic atoms. In that case the dipole moments can be averaged by $\mathbf{d}_{A,km}\mathbf{d}_{A,mk} = |\mathbf{d}_{A,km}|^2/3\,\mathbf{I}$ with the unitary matrix $\mathbf{I}$ and

$$\left[\mathbf{d}_{A,km} \cdot \boldsymbol{G}_0(\mathbf{r}_A, \mathbf{r}_B) \cdot \mathbf{d}_{B,nl}\right]^2 = \frac{|\mathbf{d}_{A,km}|^2}{3} \frac{|\mathbf{d}_{B,nl}|^2}{3} \mathrm{Tr}\left[\boldsymbol{G}_0(\mathbf{r}_A, \mathbf{r}_B) \cdot \boldsymbol{G}_0(\mathbf{r}_B, \mathbf{r}_A)\right]. \tag{4.18}$$

Therefore, a potential U_{vdW} for arbitrary surroundings can be given in relation to the vacuum potential by

$$\frac{U_{\mathrm{vdW}}}{U_{\mathrm{vdW}}^{\mathrm{vac}}} = \frac{\mathrm{Tr}\left[\boldsymbol{G}_0(\mathbf{r}_A, \mathbf{r}_B) \cdot \boldsymbol{G}_0(\mathbf{r}_B, \mathbf{r}_A)\right]}{\mathrm{Tr}\left[\boldsymbol{G}_0^{(0)}(\mathbf{r}_A, \mathbf{r}_B) \cdot \boldsymbol{G}_0^{(0)}(\mathbf{r}_B, \mathbf{r}_A)\right]}. \tag{4.19}$$

Note that the Green's tensor in the numerator, $\boldsymbol{G}_0 = \boldsymbol{G}_0^{(0)} + \boldsymbol{G}_0^{(1)}$, is the sum of free space Green's tensor $\boldsymbol{G}_0^{(0)}$ and scattering Green's tensor $\boldsymbol{G}_0^{(1)}$.

4.1.1. Rydberg atoms above a perfect conductor

For a perfect conductor in the xy-plain, the Green's tensor can be constructed by the method of images [107] and in the nonretarded limit is given by equation (A.17) [105]. For both parallel and perpendicular alignment of the atoms, the relevant length scale becomes interatomic distance divided by surface distance denoted by x/d and z_-/d, respectively. The results for two atoms placed parallel and perpendicular in front of a perfect conductor are plotted in figure 4.2 **a** and **b**, respectively. The interaction potential is reduced by the presence of a perfect conductor in the parallel setup and enhanced when the atoms are positioned perpendicularly above the surface. Note that for the calculations of the graphs of figure 4.2, a relative minus sign in the Green's tensor was corrected compared to the original publication [105] which leads to different plots.

In the nonretarded van der Waals limit, the potentials can be described by equation (4.17) and, thus, by their C_6 coefficient. When the atoms are in parallel alignment above the surface the potential is reduced to approximately $C_6 \approx 0.68 C_6^{\mathrm{vac}}$ at $x/d = 5$. This means a reduction of the Rydberg blockade radius (2.124) to $R_{\mathrm{block}} = \sqrt[6]{0.68 C_6} \approx 0.94 R_{\mathrm{block}}^{\mathrm{vac}}$. As this reduction is independent of the specific pair states, one can estimate whether such an effect might be visible in an experiment. Baur *et al.* [108] found a blockade radius $R_{\mathrm{block}} \approx 14\mu$m for $|100s_{1/2}, m_j = 1/2; 100s_{1/2}, m_j = -1/2\rangle$ states of ^{87}Rb. Thus, at the threshold where atomic distance equals blockade radius, $x = R_{\mathrm{block}}$, a surface distance $d \leq 2.8\,\mu$m would effectively reduce the blockade radius by $0.84\,\mu$m.

The Green's tensor for a dielectric plate can obtained from equation (A.17) by multiplying the second (scattering) terms with the Fresnel reflection coefficient r_p. The long distance limit of the potentials then becomes

$$\lim_{(x/d)\to\infty} \left.\frac{U_{\mathrm{vdW}}}{U_{\mathrm{vdW}}^{\mathrm{vac}}}\right|_{\parallel} = 1 - \frac{4r_p}{3} + r_p^2, \tag{4.20}$$

$$\lim_{(z_-/d)\to\infty} \left.\frac{U_{\mathrm{vdW}}}{U_{\mathrm{vdW}}^{\mathrm{vac}}}\right|_{\perp} = 1 + \frac{2r_p}{3} + r_p^2. \tag{4.21}$$

One can see from figure 4.2 that these limits are fulfilled for $r_p = 1$ for a perfect conductor. While at first glance the enhancement of the interaction in the perpendicular case seems dramatic in the long distance limit, this has to be put into perspective. Although for a perfect conductor the limit $\lim_{(z_-/d)\to\infty} U_{\mathrm{vdW}}/U_{\mathrm{vdW}}^{\mathrm{vac}}|_{\perp} = 8/3$ promises a drastic amplification of the potential, the absolute value of the potential will remain low due to the overall z_-^{-6} behavior.

4.1.2. Rydberg particles inside crystals with finite thickness

Rydberg excitons have been introduced in section 2.3.4. As excited states of electron-hole pairs in semiconductors they occur in a finite volume. The experiment conducted by Kazimierczuk *et al.* [87] used a Cu_2O crystal of $34\,\mu$m thickness while in the experiment by Versteegh *et al.* [88] a $840\,\mu$m thick crystal was used. Together with the the calculated exciton radius of $\langle r\rangle_{n=25} \approx 1\,\mu$m and $\langle r\rangle_{n=30} \approx 1.5\,\mu$m it is reasonable to assume that the finite thickness can play a role in the interactions. Since equation (4.19) does not impose any assumptions on the particles' species it is suitable for an educated guess regarding the influence. However, the results have to be treated carefully as the excitons' rotational symmetry and, hence, their isotropy is broken inside cubic crystals [89].

a

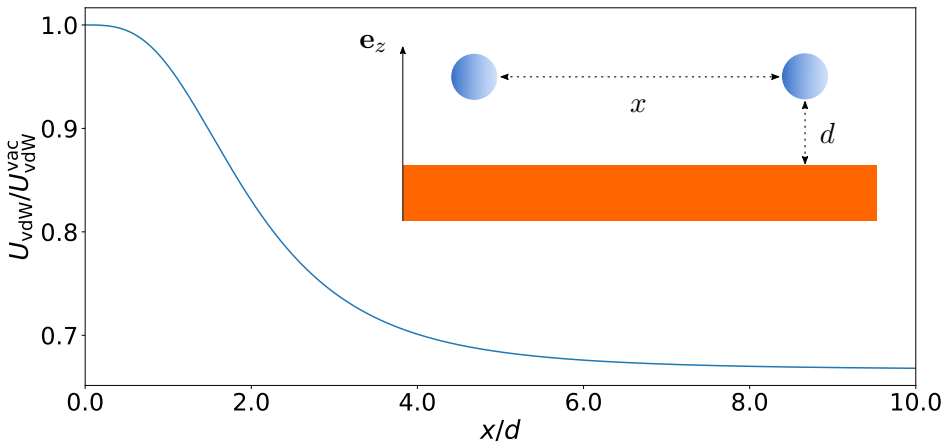

b

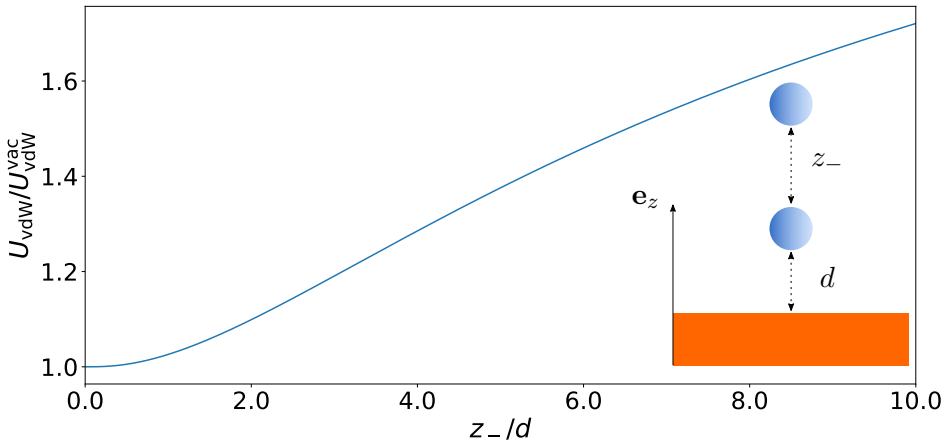

Figure 4.2.: The surface-modified potential U_{vdW} for two isotropic atoms close to a perfect mirror in relation to the free space potential $U_{\mathrm{vdW}}^{\mathrm{vac}}$. In this limit, the relevant length scale becomes **a** for parallelly aligned atoms x/d and **b** for perpendicularly aligned atoms z_-/d. The insets show the respective orientation and distances, $\mathbf{e}_z$ denotes the unit vector in z-direction.

The cuprous oxide crystal screens the interaction between two excitons and, thus, the Green's tensor $\boldsymbol{G}_0(\mathbf{r}_A, \mathbf{r}_B)$ has to be replaced by the local-field corrected one [109],

$$\boldsymbol{G}_{0,\mathrm{loc}}(\mathbf{r}_A, \mathbf{r}_B) = \left(\frac{3\varepsilon}{2\varepsilon+1}\right)^2 \frac{\boldsymbol{G}_0(\mathbf{r}_A, \mathbf{r}_B)}{\varepsilon}, \tag{4.22}$$

with the relative permittivity ε. Equation (4.22) is true in the case of $\mathbf{r}_A$ and $\mathbf{r}_B$ being in the same dielectric medium. As a simple static model for cuprous oxide Cu_2O, one can assume $\varepsilon_{\mathrm{Cu_2O}} = 7.5$. This amounts to

$$\boldsymbol{G}_{0,\mathrm{loc}}(\mathbf{r}_A, \mathbf{r}_B) \approx 0.26 \boldsymbol{G}_0(\mathbf{r}_A, \mathbf{r}_B). \tag{4.23}$$

The Fresnel reflection coefficient becomes $r_p = (\varepsilon - 1)/(\varepsilon + 1) \approx 0.76$. The Green's tensor for two points in the middle layer of a planar three-layer system is known and given by [13]

$$\begin{aligned}\boldsymbol{G}^{(1)}(\mathbf{r}, \mathbf{r}', \mathrm{i}\xi) = \int \mathrm{d}^2 q \, \frac{e^{\mathrm{i}\mathbf{q}\cdot(\mathbf{r}-\mathbf{r}')}}{8\pi^2 b} \sum_{\sigma=s,p} \times \Bigg\{ \\ + \frac{r_\sigma^- r_\sigma^+ e^{-2bd}}{1 - r_\sigma^- r_\sigma^+ e^{-2bd}} \left[\mathbf{e}_\sigma^+ \otimes \mathbf{e}_\sigma^+ e^{-b(z-z')} + \mathbf{e}_\sigma^- \otimes \mathbf{e}_\sigma^- e^{-2bd+b(z-z')}\right] \\ + \frac{1}{1 - r_\sigma^- r_\sigma^+ e^{-2bd}} \left[\mathbf{e}_\sigma^+ \otimes \mathbf{e}_\sigma^- r_\sigma^- e^{-b(z+z')} + \mathbf{e}_\sigma^- \otimes \mathbf{e}_\sigma^+ r_\sigma^+ e^{-2bd+b(z+z')}\right] \Bigg\}.\end{aligned} \tag{4.24}$$

Here, $\mathbf{q}$ is the in plane-wave vector and b is the wave vector component normal to the surfaces. The reflection coefficients r^+ (r^-) account for reflections at the top (bottom) boundary. In the nonretarded limit, $b = \sqrt{\xi^2/c^2\varepsilon(\mathrm{i}\xi) + q^2} \approx q$. The sum over the polarizations $\sigma = s, p$ reduces in the nonretarded limit to contributions from p-polarized waves. Therefore, also only the unit vectors $\mathbf{e}_p^\pm$ contribute and in the nonretarded limit

$$\mathbf{e}_p^\pm \approx -\frac{q}{\kappa} \left[\pm \cos\phi \, \mathbf{e}_x \pm \sin\phi \, \mathbf{e}_y + \mathrm{i}\mathbf{e}_z\right]. \tag{4.25}$$

with wave number κ. Now, the task is to compute the static limit of equation (4.24). Remember, that $\boldsymbol{G}_0 = \lim_{\omega\to 0} \omega^2/c^2 \boldsymbol{G} = \lim_{\kappa\to 0} \kappa^2 \boldsymbol{G}$. For the simplest case, one can assume $z = z'$ so that $\mathbf{q}\cdot(\mathbf{r} - \mathbf{r}') = qx\cos\phi$. To this end the $\mathrm{d}^2 q$ integral is transformed to polar coordinates.

Then, the $\mathrm{d}\phi$-integral can be performed:

$$\begin{aligned}
&\int_0^{2\pi} \mathrm{d}\phi\, e^{\mathrm{i}qx\cos\phi} \left[\mathbf{e}_p^+ \otimes \mathbf{e}_p^+ + \mathbf{e}_p^- \otimes \mathbf{e}_p^-\right] \\
&= \frac{2\pi q^2}{\kappa^2} \begin{pmatrix} J_0(qx) - J_2(qx) & 0 & 0 \\ 0 & J_0(qx) + J_2(qx) & 0 \\ 0 & 0 & -2J_0(qx) \end{pmatrix}, \qquad (4.26) \\
&\int_0^{2\pi} \mathrm{d}\phi\, e^{\mathrm{i}qx\cos\phi} \mathbf{e}_p^\pm \otimes \mathbf{e}_p^\mp \\
&= -\frac{\pi q^2}{\kappa^2} \begin{pmatrix} J_0(qx) - J_2(qx) & 0 & \pm 2J_1(qx) \\ 0 & J_0(qx) + J_2(qx) & 0 \\ \mp 2J_1(qx) & 0 & -2J_0(qx) \end{pmatrix}. \qquad (4.27)
\end{aligned}$$

Now, the integral over the radial part $\mathrm{d}q$ can be performed by using a power series expansion for the Bessel functions,

$$J_\nu(z) = \sum_{k=0}^{\infty} \frac{(-1)^k}{k!(k+\nu)!} \left(\frac{z}{2}\right)^{\nu+2k}. \qquad (4.28)$$

Using the expansion (4.28) and $r_- = r_+ \equiv r$, three types of integrals remain,

$$\int_0^\infty \mathrm{d}q\, \frac{q^n}{1 - r^2 e^{-2qd}} = \frac{n!}{(2d)^{n+1}} \mathrm{Li}_{n+1}(r^2), \qquad (4.29)$$

$$\int_0^\infty \mathrm{d}q\, \frac{q^n e^{-2qz}}{1 - r^2 e^{-2qd}} = \frac{n!}{(2d)^{n+1}} \Phi_{n+1}(r^2, z/d), \qquad (4.30)$$

$$\int_0^\infty \mathrm{d}q\, \frac{q^n e^{-2q(d-z)}}{1 - r^2 e^{-2qd}} = \frac{n!}{(2d)^{n+1}} \Phi_{n+1}(r^2, 1 - z/d). \qquad (4.31)$$

Here, $\mathrm{Li}_n(x)$ is the polylogarithm function and $\Phi_n(x)$ the Lerch Phi function. These function can be approximated to a high degree of precision for $n \geq 3$ by

$$\mathrm{Li}_n(r^2) \approx r^2, \qquad \Phi_n(r^2, z/d) \approx (d/z)^n. \qquad (4.32)$$

Combining this, there are two types of integrals including the Bessel functions,

$$\begin{aligned} I_m &= \int_0^\infty \mathrm{d}q \, \frac{r^2 e^{-2qd}}{1 - r^2 e^{-2qd}} q^2 J_m(qx) \\ &\approx \frac{(m+2)!}{m!} \left(\frac{x}{4d}\right)^m \frac{r^2}{(2d)^3} \, {}_2F_1\left(\frac{m+3}{2}, \frac{m+4}{2}; m+2; -\frac{x^2}{4d^2}\right), \end{aligned} \tag{4.33}$$

$$\begin{aligned} \tilde{I}_m &= \int_0^\infty \mathrm{d}q \, \frac{r e^{-2qz}}{1 - r^2 e^{-2qd}} q^2 J_m(qx) \\ &\approx \frac{(m+2)!}{m!} \left(\frac{x}{4z}\right)^m \frac{r}{(2d)^3} \, {}_2F_1\left(\frac{m+3}{2}, \frac{m+4}{2}; m+2; -\frac{x^2}{4z^2}\right), \end{aligned} \tag{4.34}$$

with the Gauss hypergeometric function ${}_2F_1$. For $z = z' = d/2$, one finds for the scattering Green's tensor in the nonretarded limit

$$4\pi\kappa^2 \boldsymbol{G}^{(1)}(\mathbf{r}, \mathbf{r}', \mathrm{i}\xi) \approx \mathrm{diag}\left(I_0 - I_2 - \tilde{I}_0 + \tilde{I}_2, I_0 + I_2 - \tilde{I}_0 - \tilde{I}_2, -2I_0 - 2\tilde{I}_0\right). \tag{4.35}$$

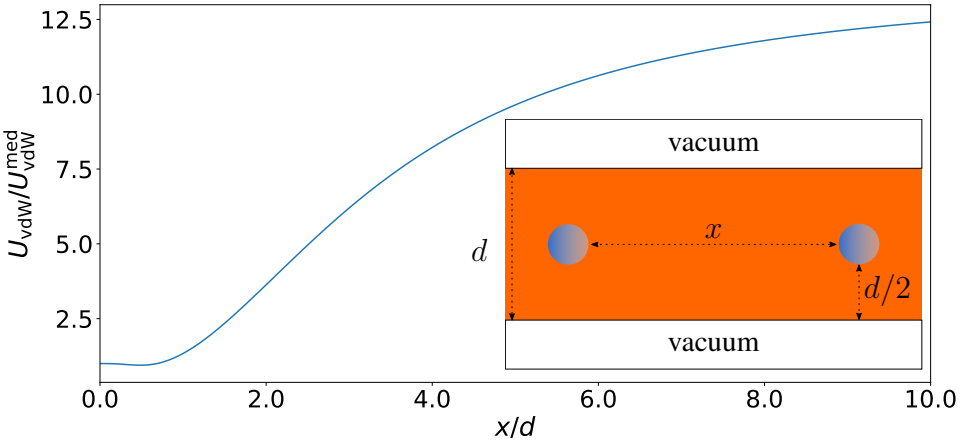

Figure 4.3.: The surface-modified potential U_{vdW} for two isotropic particles inside a crystal(orange) in relation to the free bulk potential $U_{\mathrm{vdW}}^{\mathrm{med}}$.As it is shown in the inset, the atoms are positioned at $z = z' = d/2$ with the crystal thickness d. The crystal is surrounded by vacuum. The relevant length scale is x/d.

Now, the relation between the full potential and the free space potential can be plotted according to (4.19). The only remaining length scale in this ratio is x/d, i.e. the interparticle distance x over the crystal thickness d. The results in figure 4.3 show an enhanced potential for $x/d \gtrsim 0.75$. In the experiment by Kazimierczuk *et al.* [87] a blockade radius $R_{\mathrm{block}} = 30\,\mu\mathrm{m}$ was estimated that serves as the approximate interexcitonic distance x. The Cu_2O crystal

used in the experiment had a thickness of $d = 34\,\mu$m. Therefore, the ratio $x/d \approx 0.88$ which corresponds to an increase of the interaction potential by approximately 17.5% [105]. The blockade radius R_{block} scales with $(C_6)^{1/6}$ and, thus, the relative change is less pronounced. As the measured $R_{\mathrm{block}} = 30\,\mu$m already includes all effects from the crystal, one can estimate the blockade radius inside an infinite crystal by

$$R_{\mathrm{block}}^{\mathrm{inf}} = \frac{R_{\mathrm{block}}}{(1.175)^{1/6}} \approx 29.2\,\mu\mathrm{m}. \tag{4.36}$$

4.2. Pair potentials from exact diagonalization

The results found in the perturbative regime in section 4.1 offer a relatively fast insight into the influence of surfaces the atomic pair potentials. However, (nondegenerate) perturbation theory fails when describing actual Rydberg atomic potentials since the Förster defect can become very small [57]. Furthermore, the large wave function of Rydberg states demands the inclusion of higher-order multipole moments than dipole-dipole interactions to the Hamiltonian [105; 110]. The multipole interaction Hamiltonian in the nonretarded limit can be written as

$$\begin{aligned}\hat{H}_{\mathrm{int}} = {} & \hat{\mathbf{d}}_A \cdot \boldsymbol{G}_0(\mathbf{r}_A, \mathbf{r}_B) \cdot \hat{\mathbf{d}}_B \\ & + \hat{\mathbf{d}}_A \cdot \boldsymbol{G}_0(\mathbf{r}_A, \mathbf{r}_B) \overleftarrow{\nabla}_B : \hat{\mathbf{Q}}_B + \hat{\mathbf{Q}}_A : \overrightarrow{\nabla}_A \boldsymbol{G}_0(\mathbf{r}_A, \mathbf{r}_B) \cdot \hat{\mathbf{d}}_B.\end{aligned} \tag{4.37}$$

The indices of the gradient operator indicate the argument of the Green's tensor that are subject of the derivative. $\mathbf{Q}_i = q/2\mathbf{r} \otimes \mathbf{r}$ denotes the tensorial quadrupole operator of atom i and the notation ":" indicates the Frobenius inner product, i.e. the contraction of two indices. The gradient of the free space Green's tensor in the nonretarded limit, $\boldsymbol{G}_0^{(0)}(\mathbf{r}_A, \mathbf{r}_B) = \lim_{\omega \to 0} \omega^2/c^2 \boldsymbol{G}^{(0)}(\mathbf{r}_A, \mathbf{r}_B, \omega)$, is

$$\overrightarrow{\nabla}_A \boldsymbol{G}_0^{(0)}(\mathbf{r}_A, \mathbf{r}_B) = \frac{1}{4\pi} \left\{ \frac{3}{r^4} \mathbf{I} \otimes \mathbf{e}_r - \frac{9}{r^4} \mathbf{e}_r \otimes \mathbf{e}_r \otimes \mathbf{e}_r + \frac{3}{r^3} \overrightarrow{\nabla}_A (\mathbf{e}_r \otimes \mathbf{e}_r) \right\}. \tag{4.38}$$

The last gradient can be expressed as

$$\overrightarrow{\nabla}_A (\mathbf{e}_r \otimes \mathbf{e}_r) = \overline{\mathbf{A}}_x \otimes \mathbf{e}_x + \overline{\mathbf{A}}_y \otimes \mathbf{e}_y + \overline{\mathbf{A}}_z \otimes \mathbf{e}_z \tag{4.39}$$

with

$$\overline{\mathbf{A}}_x = \begin{pmatrix} 2\frac{x}{r^2} - 2\frac{x^3}{r^4} & \frac{y}{r^2} - 2\frac{xy^2}{r^4} & \frac{z}{r^2} - 2\frac{x^2z}{r^4} \\ \frac{y}{r^2} - 2\frac{xy^2}{r^4} & -2\frac{xy^2}{r^4} & -2\frac{xyz}{r^4} \\ \frac{z}{r^2} - 2\frac{x^2z}{r^4} & -2\frac{xyz}{r^4} & -2\frac{xz^2}{r^4} \end{pmatrix}, \tag{4.40}$$

$$\overline{\mathbf{A}}_y = \begin{pmatrix} -2\frac{x^2y}{r^4} & \frac{x}{r^2} - 2\frac{xy^2}{r^4} & -2\frac{xyz}{r^4} \\ \frac{x}{r^2} - 2\frac{xy^2}{r^4} & 2\frac{y}{r^2} - 2\frac{y^3}{r^4} & \frac{z}{r^2} - 2\frac{y^2z}{r^4} \\ -2\frac{xyz}{r^4} & \frac{z}{r^2} - 2\frac{y^2z}{r^4} & -2\frac{yz^2}{r^4} \end{pmatrix}, \tag{4.41}$$

$$\overline{\mathbf{A}}_z = \begin{pmatrix} -2\frac{x^2z}{r^4} & -2\frac{xyz}{r^4} & \frac{x}{r^2} - 2\frac{xz^2}{r^4} \\ -2\frac{xyz}{r^4} & -2\frac{y^2z}{r^4} & \frac{y}{r^2} - 2\frac{yz^2}{r^4} \\ \frac{x}{r^2} - 2\frac{xz^2}{r^4} & \frac{y}{r^2} - 2\frac{yz^2}{r^4} & 2\frac{z}{r^2} - 2\frac{z^3}{r^4} \end{pmatrix}. \tag{4.42}$$

The gradient from the right with respect to $\mathbf{r}_B$ of the free space Green's tensor is

$$\boldsymbol{G}_0^{(0)} \overleftarrow{\nabla}_B = \frac{1}{4\pi} \left\{ -\frac{3}{r^4} \mathbf{e}_r \otimes \mathbf{I} + \frac{9}{r^4} \mathbf{e}_r \otimes \mathbf{e}_r \otimes \mathbf{e}_r - \frac{3}{r^3} \left(\mathbf{e}_x \otimes \overline{\mathbf{A}}_x + \mathbf{e}_y \otimes \overline{\mathbf{A}}_y + \mathbf{e}_z \otimes \overline{\mathbf{A}}_z \right) \right\}. \tag{4.43}$$

Similarly, the gradients of the scattering Green's tensor can be calculated.

$$\begin{aligned} \overrightarrow{\nabla}_A \boldsymbol{G}_0^{(1)} = \frac{1}{4\pi} \Bigg\{ & -\frac{3}{r_+^5} \begin{pmatrix} 1 & 0 & 0 \\ 0 & 1 & 0 \\ 0 & 0 & 2 \end{pmatrix} \otimes \mathbf{r}_+ + \frac{15}{r_+^7} \begin{pmatrix} x^2 & 0 & -xz_+ \\ 0 & 0 & 0 \\ xz_+ & 0 & x^2 \end{pmatrix} \otimes \mathbf{r}_+ \\ & -\frac{3}{r_+^5} \left[\begin{pmatrix} 2x & 0 & -z_+ \\ 0 & 0 & 0 \\ z_+ & 0 & 2x \end{pmatrix} \otimes \mathbf{e}_x + \begin{pmatrix} 0 & 0 & -x \\ 0 & 0 & 0 \\ x & 0 & 0 \end{pmatrix} \otimes \mathbf{e}_z \right] \Bigg\} \end{aligned} \tag{4.44}$$

$$\begin{aligned} \boldsymbol{G}_0^{(1)} \overleftarrow{\nabla}_B = \frac{1}{4\pi} \Bigg\{ & +\frac{3}{r_+^5} \tilde{\mathbf{r}}_+ \otimes \begin{pmatrix} 1 & 0 & 0 \\ 0 & 1 & 0 \\ 0 & 0 & 2 \end{pmatrix} - \frac{15}{r_+^7} \tilde{\mathbf{r}}_+ \otimes \begin{pmatrix} x^2 & 0 & -xz_+ \\ 0 & 0 & 0 \\ xz_+ & 0 & x^2 \end{pmatrix} \\ & -\frac{3}{r_+^5} \left[\mathbf{e}_x \otimes \begin{pmatrix} -2x & 0 & z_+ \\ 0 & 0 & 0 \\ -z_+ & 0 & -2x \end{pmatrix} + \mathbf{e}_z \otimes \begin{pmatrix} 0 & 0 & -x \\ 0 & 0 & 0 \\ x & 0 & 0 \end{pmatrix} \right] \Bigg\}. \end{aligned} \tag{4.45}$$

Here, $\mathbf{r}_+ = x\mathbf{e}_x + z_+\mathbf{e}_z$ and $\tilde{\mathbf{r}}_+ = x\mathbf{e}_x - z_+\mathbf{e}_z$. Note that this corrects some calculations from [105]. However, due to the choice of particle orientation and the relatively small influence of higher order moments, the further results remain qualitatively valid. In principle, higher order moments can be calculated in a straightforward manner. The expansion of the Hamiltonian (4.37) to the next higher order would include quadrupole-quadrupole terms as well as dipole-octupole terms in order to stay consistent regarding the level of truncation.

4.2.1. Diagonalization of the Hamiltonian

The next step is the diagonalization of the Hamiltonian (4.37). In free space the quantization axis can always be chosen along the interatomic axis and the total projection of the angular momentum $M = m_A + m_B$ is conserved [57]. This conservation law enables one to decompose the total matrix of states into blocks of constant M which considerably simplifies and accelerates the calculations. In the case when atoms are placed close to a surface there are two distinct axes, namely the interatomic axis and the axis normal to the surface. Hence, the quantization axis cannot be chosen along both axes simultaneously. As a consequence the conservation law regarding M breaks down and, thus, the necessary basis set becomes substantially larger. For example, Stanojevic *et al.* [111] examined two Rb atoms in the two atom state $|70p; 70p\rangle$ and included 142 closely coupled states in the calculations. Therefore, a 142×142 matrix had to be diagonalized. Breaking the symmetry and allowing a change in M, the required basis set immediately becomes a 700×700 matrix [105]. Although this increases the total number of elements by more than a factor 20, the matrix dimension remains small as, in general, for convergence of the free space pair potential basis sets of 4000 to 6000 states are mandatory [112].

An implementation of the diagonalization can be done on one's own initiative. The interaction Hamiltonian (4.37) can be expanded into a basis of states $|\psi\rangle = |n, l, j, m_j\rangle$. Here, n denotes the main quantum number, l the angular momentum, $j = l \pm 1/2$ the total angular momentum including the spin and $m_j \in [-j, j]$ is the projection of j onto the quantization axis. For Rydberg atoms, the energy spectrum can be described by equation (2.123) and the according quantum defects δ_{nlj} can be found in the literature, e.g. for rubidium in [113–117]. The radial matrix elements of dipole operator and quadrupole operator, $\langle n, l, j, m_j|\hat{r}|n', l', j', m'_j\rangle$ and $\langle n, l, j, m_j|\hat{r}^2|n', l', j', m'_j\rangle$, respectively, can be calculated using Numerov's method [118]. The dipole and quadrupole operators can be expressed in terms of spherical harmonics Y_{kq}. This allows one to use the Wigner-Eckhart theorem to calculate the angular components of the

transition moments by

$$\begin{aligned}\langle l, j, m_j | Y_{kq} | l', j', m_j' \rangle = (-1)^{j+j'-m_j+k+\frac{1}{2}} \\ \times \sqrt{\frac{(2j+1)(2j'+1)(2l+1)(2l'+1)(2k+1)}{4\pi}} \\ \times \begin{pmatrix} j & k & j' \\ -m & q & m' \end{pmatrix} \begin{pmatrix} l & k & l' \\ 0 & 0 & 0 \end{pmatrix} \begin{Bmatrix} l & j & \frac{1}{2} \\ j' & l' & k \end{Bmatrix}\end{aligned} \tag{4.46}$$

where the electron spin was set $s = s' = 1/2$ and the Wigner $3j$-symbol $\begin{pmatrix} l & l' & L \\ m & m' & M \end{pmatrix}$ and Wigner $6j$-symbol $\begin{Bmatrix} l & j & s \\ j' & l' & k \end{Bmatrix}$ were used. These remarks allow one to implement the desired Hamiltonian independently, see e.g. [105; 111; 112].

However, the task of implementing a self-made diagonalization algorithm may be obsolete as there are alternatives of well-tested and acknowledged software like ARC [119] or PAIRINTERACTION [120]. The applications of the open-source software PAIRINTERACTION include but are not limited to the calculation of the pair interaction potential between two atoms. It includes data for all alkali metal atoms and is programmed to deliver energy levels, matrix elements and Zeeman and Stark maps for individual atoms. More applications and a general overview of the program can be found on the website [121]. Together with Sebastian Weber, author of [120; 121], I have implemented the Green's tensor formalism into the PAIRINTERACTION code up to the dipole-quadrupole Hamiltonian (4.37). PAIRINTERACTION now can incorporate the influence of perfectly conducting surfaces in the pair potential. The according code can be found in appendix C.

It is then possible to use PAIRINTERACTION to measure the influence of a surface on concrete pair potentials. We consider two rubidium atoms horizontally aligned above a perfectly conducting surface. Figure 4.4 is produced with PAIRINTERACTION. A simple example how to create such figures is given in appendix C. The figure shows the effect of the surface on an atomic pair potential at atom-surface distance $d = 1\,\mu$m (red dots) compared to the free-space potential (black dots) as a function of interatomic distance x. The energy scale is relative to the $|70p_{3/2}; 70p_{3/2}\rangle$ asymptote of rubidium, i.e. $E(|70p_{3/2}; 70p_{3/2}\rangle) = 0$. One can clearly see the reduction of the interaction strength to due the presence of the surface as it was predicted in section 4.1.

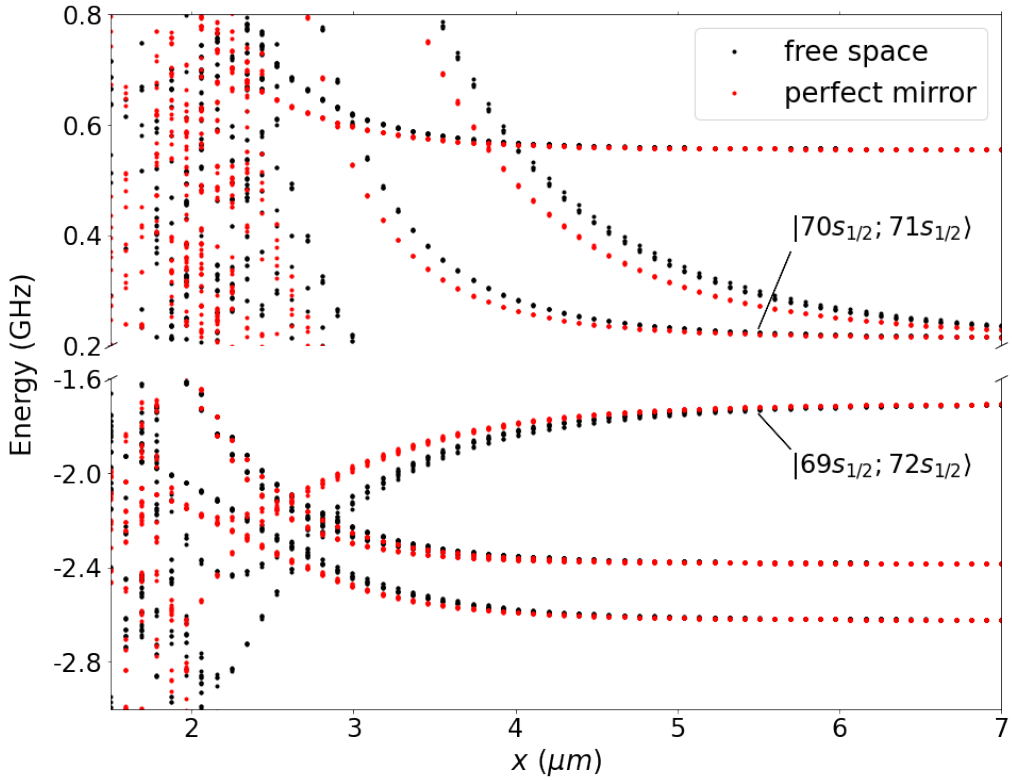

Figure 4.4.: Pair potential calculated with pairinteraction as a function of interatomic distance x with zero energy at the $|70p_{3/2}; 70p_{3/2}\rangle$ asymptote. Red dots indicate the surface-influenced potential at distance $d = 1\ \mu$m from a perfect mirror, black dots the free space potential. The pair potential of the annotated asymptotes can be approximated by a nonretarded van der Waals potential. At small distances, the *spaghetti*-type region of the pair potential can be seen. Note that the scaling of the y-axis changes for better readability.

The $|69s_{1/2}, m_j = 1/2; 72s_{1/2}, m_j = 1/2\rangle$ and $|70s_{1/2}, m_j = 1/2; 71s_{1/2}, m_j = 1/2\rangle$ asymptotes of rubidium are analyzed further. In the case of horizontally aligned atoms, all distances can be summarized in the single length scale x/d with interatomic distance x and surface distance d. For these specific asymptotes, the more complex pair potential can be approximated by the nonretarded van der Waals potential 4.17. The dependence of C_6 from the ration x/d rather than just from the surface distance d seems counterintuitive since in free space, C_6 is not a function of interatomic distance x. However, since the relative influence of the surface varies with x/d and the potential is not a true nonretarded van der Waals potential, C_6 can be interpreted to vary also with x. Thus, from the pair potential and the respective energy shift ΔE, the van der Waals C_6 coefficient can be extracted by $|C_6| = |\Delta E|x^6$. The absolute results for the $|69s_{1/2}; 72s_{1/2}\rangle$ and $|70s_{1/2}; 71s_{1/2}\rangle$ asymptotes are plotted in figure 4.5 **a**. In figure 4.5 **b** the relative change of the C_6 coefficients with respect to the vacuum coefficient C_6^{vac} is plotted for the two asymptotes together with the analytically obtained reduction of the C_6 coefficient. In addition, also the relative change of C_6 is shown for the $|100s_{1/2}, m_j = 1/2; 100s_{1/2}, m_j = -1/2\rangle$ asymptote from [108].

It becomes obvious, that the qualitative behavior is predicted well by perturbation theory and that in case of the $|70s_{1/2}; 71s_{1/2}\rangle$ pair state (solid orange line) and the $|100s_{1/2}; 100s_{1/2}\rangle$ pair state (red dotted line) even the quantitative agreement with the analytical results (dashed green line) is excellent. This shows that the potentials of these two pair states are dominated by the nonretarded van der Waals interaction and that other terms play a more prominent role for the $|69s_{1/2}; 72s_{1/2}\rangle$ asymptote.

For $x/d \approx 5$ the dispersion coefficient C_6 is reduced to approximately $0.75C_6^{\text{vac}}$ for the $|69s_{1/2}; 72s_{1/2}\rangle$ states and to $0.68C_6^{\text{vac}}$ for the $|70s_{1/2}; 71s_{1/2}\rangle$ and $|100s_{1/2}; 100s_{1/2}\rangle$ pair states. Although the reduction of C_6 is significant for $x/d \gtrsim 2$, the effect on the Rydberg blockade radius $R_{\text{block}} = \sqrt[6]{|C_6|/\hbar\delta\omega_L}$ is less pronounced due to the $(C_6)^{1/6}$ power law. The resulting decrease of the blockade radius is approximately 5% for the $|69s_{1/2}; 72s_{1/2}\rangle$ asymptote and 6% for the $|70s_{1/2}; 71s_{1/2}\rangle$ and $|100s_{1/2}; 100s_{1/2}\rangle$ asymptotes at $x/d = 5$. As the $|100s_{1/2}; 100s_{1/2}\rangle$ asymptote agrees well with the analytical results in figure 4.5 **b**, the assessment of the change of the blockade radius R_{block} in section 4.1.1 could be validated.

All in all, the change of the $C_6 \equiv C_6(x/d)$ coefficient was calculated using PAIRINTERACTION for different two-atom state asymptotes for horizontally aligned atoms above a perfectly conducting surface with interatomic distance x and surface distance d. It was found that the numerically extracted C_6 shows the same qualitative behavior as it was expected from perturbation theory. The pronounced change of C_6 for $x/d \gtrsim 2$ suggests the possibility of macroscopic tuning devices for interatomic interactions as described in section 4.1.1.

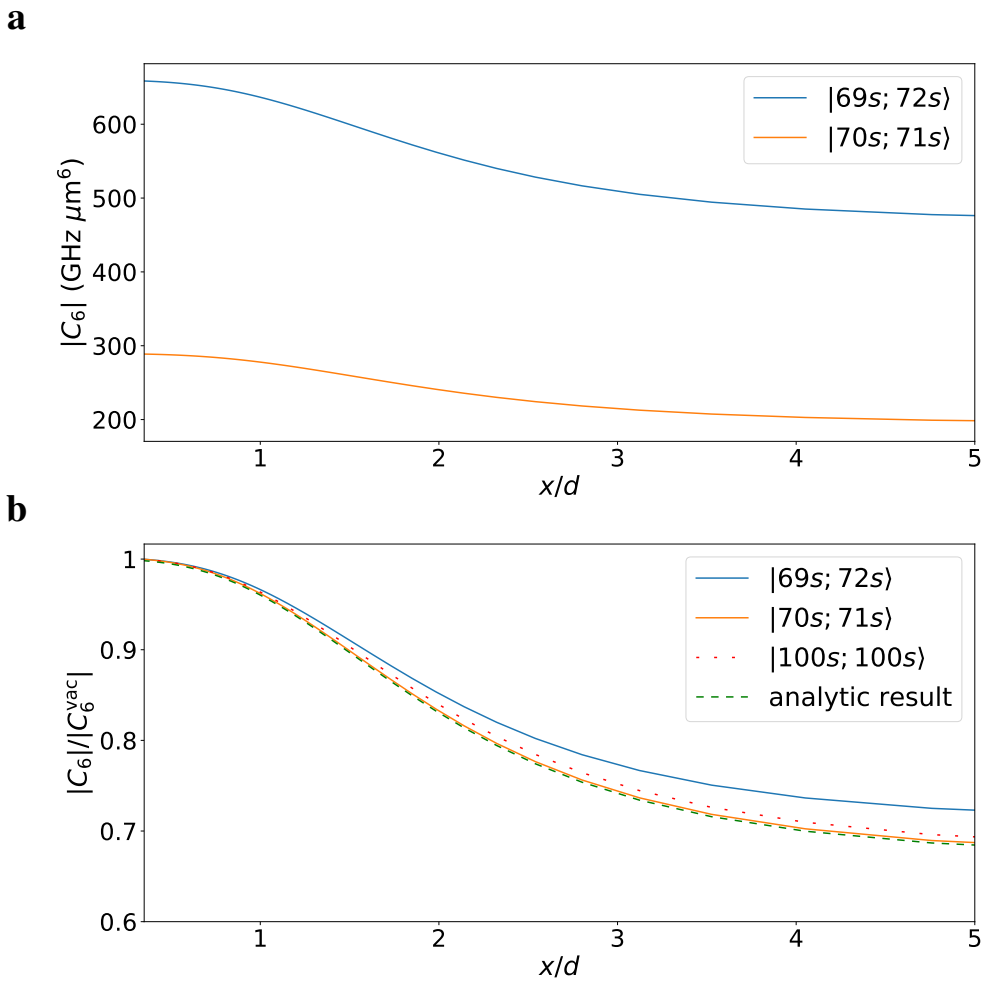

Figure 4.5.: The behavior of the dispersion coefficients C_6 as a function of interatomic distance by surface distance, x/d, for atoms horizontally aligned above a perfectly conducting plate. Plotted for two Rb asymptotes, $|69s_{1/2}; 72s_{1/2}\rangle$ and $|70s_{1/2}; 71s_{1/2}\rangle$. **a** Absolute value $|C_6|$. **b** C_6 normalized by the respective vacuum coefficient C_6^{vac}. The curves show the same qualitative behavior that was predicted by the analytical calculations in the perturbative regime. The red dotted line shows the relative C_6 of the $|100s_{1/2}; 100s_{1/2}\rangle$ asymptote. The green dashed line shows the analytic result plotted in figure 4.2 **a** as a comparison.

4.3. Surface-induced Rydberg macrodimers

So far in this thesis, a single atom in front of a surface was considered in chapter 3 and the influence of a surface to the interatomic pair potential was calculated both in the perturbative regime in section 4.1 and numerically in section 4.2. When the shift in the pair interaction was discussed due to the addition of the Green's tensor, the single atom Casimir-Polder potential

was neglected. This can be explained in terms of the system's Hamiltonian,

$$\hat{H} = \hat{H}_A + \hat{H}_B + \hat{H}_{\mathrm{int}}. \tag{4.47}$$

The pair potential is the result of the interaction Hamiltonian $\hat{H}_{\mathrm{int}}$ and varies with surface distance d so that $\hat{H}_{\mathrm{int}} = \hat{H}_{\mathrm{int}}(d)$. In the previous section regarding the interaction, the single atom Hamiltonians $\hat{H}_i$ for the atoms $i = A, B$ were considered static with respect to the surface distance, $\hat{H}_i \neq \hat{H}_i(d)$. Thus, the reasonable next step and the goal of this section is the incorporation of the Casimir-Polder potential in $\hat{H}_A$ and $\hat{H}_B$ to fully describe the surface dependent pair potential. It will be shown that this description leads to the formation of potential wells that feature bound states of two Rydberg atoms. These so-called macrodimers are an interesting and highly sensitive species of molecules that might provide a tool for measuring weak electric fields [77]. One obvious example of such weak fields would be the surface-modified interactions between Rydberg atoms that lead to the formation of the dimers to begin with as we will show. Therefore, the answer whether or not macrodimers form above a surface might allow one to characterize its magnetoelectric properties.

As before, the system of interest consists of two rubidium atoms in horizontal alignment above a perfectly conducting half space. The interaction Hamiltonian is again taken in the dipole-quadrupole form of equation (4.37). The Green's tensor of the system is given by equation (A.17) for a perfectly conducting half space in the nonretarded limit. The unperturbed energy spectrum of a single atom is given by the Rydberg series

$$E_{nlj} = -\frac{E^*_{\mathrm{Ryd}}}{(n - \delta_{nlj})^2}, \tag{4.48}$$

where E^*_{Ryd} is the Rydberg energy of the specific atom, i.e. rubidium, n is the main quantum number and δ_{nlj} the quantum defect that accounts for deviations from the hydrogenic spectrum. The quantum defect is a function of n, the angular momentum quantum number l and the total angular momentum quantum number j. Now, the Casimir-Polder potential for the individual atoms has to be considered. For an atom i in an excited state $|k\rangle$ at position $\mathbf{r}_i$, the Casimir-Polder potential in the nonretarded limit is given by [14]

$$U_k(\mathbf{r}_i) = -\frac{\langle \hat{\mathbf{d}} \cdot \boldsymbol{G}_0^{(1)}(\mathbf{r}_i, \mathbf{r}_i) \cdot \hat{\mathbf{d}} \rangle_k}{2\varepsilon_0} \tag{4.49}$$

with the atomic dipole transition operator $\hat{\mathbf{d}}$. The expectation value in the numerator refers to the atomic state $|k\rangle$ and is given by

$$\langle|\hat{\mathbf{d}}|^2\rangle_k = \sum_{k'} |\hat{\mathbf{d}}_{kk'}|^2. \tag{4.50}$$

We restrict the calculation of the Casimir-Polder potential to dipole terms. While there are contributions from higher-order terms, the atomic selection rules do not allow dipole-quadrupole contributions to the potential. Terms from next higher order would include quadrupole-quadrupole as well as dipole-octupole terms as it was the case for the interaction potential (4.37). The relative contribution of multipole moments can be estimated by the ratio of the radial expectation value of the wave function and the surface distance, $(\langle R\rangle/d)^\kappa$ [122]. Here, $\kappa = 2$ corresponds to dipole-dipole interactions, $\kappa = 3$ corresponds to dipole-quadrupole interactions and so forth. For a Rydberg atom in state with $n = 50$ at a surface distance $d = 2\,\mu$m, the ratio is approximately

$$\begin{aligned}\left(\frac{\langle R\rangle}{d}\right)^\kappa &= \left(\frac{a_0 n^2}{d}\right)^\kappa \\ &= \left(\frac{5.29\times10^{-11}\,\mathrm{m}\times 50^2}{2\times10^{-6}\mathrm{m}}\right)^\kappa \\ &\approx (0.067)^\kappa.\end{aligned} \tag{4.51}$$

This shows that higher-order terms beyond dipole-quadrupole terms can be safely neglected. Contrary to the interaction potential (4.37), the Casimir-Polder potential only depends on the scattering Green's tensor $\boldsymbol{G}_0^{(1)}$. The free-space contribution from $\boldsymbol{G}_0^{(0)}$ gives rise to the vacuum Lamb shift [13] and is already included in the atomic energy spectra (4.48). The scattering Green's tensor for a perfectly conduction half-space in the nonretarded limit can be taken from the second line of (A.17),

$$\boldsymbol{G}_0^{(1)}(\mathbf{r}_A,\mathbf{r}_B) = \frac{1}{4\pi}\left[\frac{1}{\rho_+^3}\begin{pmatrix}1&0&0\\0&1&0\\0&0&2\end{pmatrix} - \frac{3}{\rho_+^5}\begin{pmatrix}x^2&0&-xz_+^2\\0&0&0\\xz_+^2&0&x^2\end{pmatrix}\right], \tag{4.52}$$

where $x = x_A - x_B$, $z_+ = z_A + z_B$ and $\rho_+^2 = x^2 + z_+^2$. Now, the single atom contribution can be easily derived by setting $x = 0$ and $z_+ = 2z_A = 2d$. Then, the Casimir-Polder potential (4.49)

becomes [13]

$$U_k(d) = -\frac{\langle \hat{\mathbf{d}}^{\parallel 2} + 2\hat{\mathbf{d}}^{\perp 2} \rangle}{64\pi\varepsilon_0 d^3}. \tag{4.53}$$

Here, the transition dipole moment $\hat{\mathbf{d}}$ was decomposed into components parallel to the surface, $\hat{\mathbf{d}}^{\parallel}$, and components perpendicular to the surface, $\hat{\mathbf{d}}^{\perp}$. Combining the Rydberg spectrum (4.48) and the Casimir-Polder potential (4.53), the energy of a single atom in state $|k\rangle = |nlj\rangle$ is given by

$$E_{nlj}(d) = E_{nlj} + U_{nlj}(d). \tag{4.54}$$

The most pronounced effects for the surface are expected for the pair potential of energetically closely spaced dipole-coupled pair states. A suitable set of pair states is $\left\{|51s_{1/2}; 53s_{1/2}\rangle, |51p_{1/2}; 52p_{1/2}\rangle\right\}$ with an energy difference between the unperturbed states of only $\Delta E = 83\,\mathrm{MHz}$. For close distances between the atoms, the electron wave functions start to overlap and the Hamiltonian in the multipole form (4.37) cannot be applied. This minimal distance can be assessed by the LeRoy radius R_{LR},

$$R_{\mathrm{LR}} = 2\left(\sqrt{\langle r^2\rangle_A} + \sqrt{\langle r^2\rangle_B}\right). \tag{4.55}$$

For the $|51p_{1/2}; 52p_{1/2}\rangle$ state, one obtains $R_{\mathrm{LR}} \approx 0.8\,\mu$m. As the calculations are restricted to a minimum interatomic distance $R \gtrsim 1.2\,\mu$m later on it can be safely assumed that the wave functions do not overlap.

The Hamiltonian (4.37) and the Casimir-Polder potential (4.53) have been added to the PAIRINTERACTION package in order to calculate the pair potentials. It is important to check whether the pair potential is convergent with respect to the number of included states [123]. The software PAIRINTERACTION allows one to restrict the included energies of all potential pair states. Starting from the single-atom states $|51p_{1/2}, m_j = 1/2\rangle$ and $|52p_{1/2}, m_j = 1/2\rangle$, the single-atom states $|n', l', j', m_j'\rangle$ that form the basis of the Hamiltonian diagonalization are restricted to

$$\begin{aligned} n' &\in [49, 53], \\ l' &\in [0, 3], \\ E' &\in \left[E\left(|51p_{1/2}\rangle\right) - 40\,\mathrm{GHz}, E\left(|52p_{1/2}\rangle\right) + 40\,\mathrm{GHz}\right]. \end{aligned}$$

From this set of single-atom states all pair states with $E'_{\mathrm{pair}} \in [E_{0,\mathrm{pair}} - 10\,\mathrm{GHz}, E_{0,\mathrm{pair}} + 10\,\mathrm{GHz}]$ form the basis of the pair states where $E_{0,\mathrm{pair}} = E\left(|51s_{1/2}; 53s_{1/2}\rangle\right)$. Using this basis set, the pair potential is fully converged.

Figure 4.6 **a** shows the unperturbed pair potential and **b** shows the pair potential at surface distance $d = 3\,\mu$m. In both the unperturbed potential and the surface-influenced potential, the highest branches of the $|51s_{1/2}; 53s_{1/2}\rangle$ asymptote and the lowest branches of the $|51p_{1/2}; 52p_{1/2}\rangle$ asymptote undergo an avoided crossing at $R \approx 3.2\,\mu$m indicated by the color mixing of blue and red to purple in figure 4.6 **a** and **b**. At interatomic distance $R \approx 2.8\,\mu$m, a new avoided crossing appears in the surface-perturbed pair potential between the $|51s_{1/2}; 53s_{1/2}\rangle$ asymptote and the $|51p_{1/2}; 52p_{1/2}\rangle$ asymptote and potential wells form. The avoided crossing has an energy gap $\Delta_{\mathrm{ac}} \approx 13.2\,\mathrm{MHz}$. In figure 4.6 **c**, a close-up of the avoided crossing region is shown. It can be seen that there are two distinct potential branches that will be referred to as upper and lower branch as it is indicated in the figure. The potential wells possess a depth of up to $\sim 63\,$MHz and can be associated with bound Rydberg macrodimer states. While these potential wells are shallower than those of the low-l Rydberg molecules described in [68] their large width allows for a great number of vibrational states as it will be shown in the following.

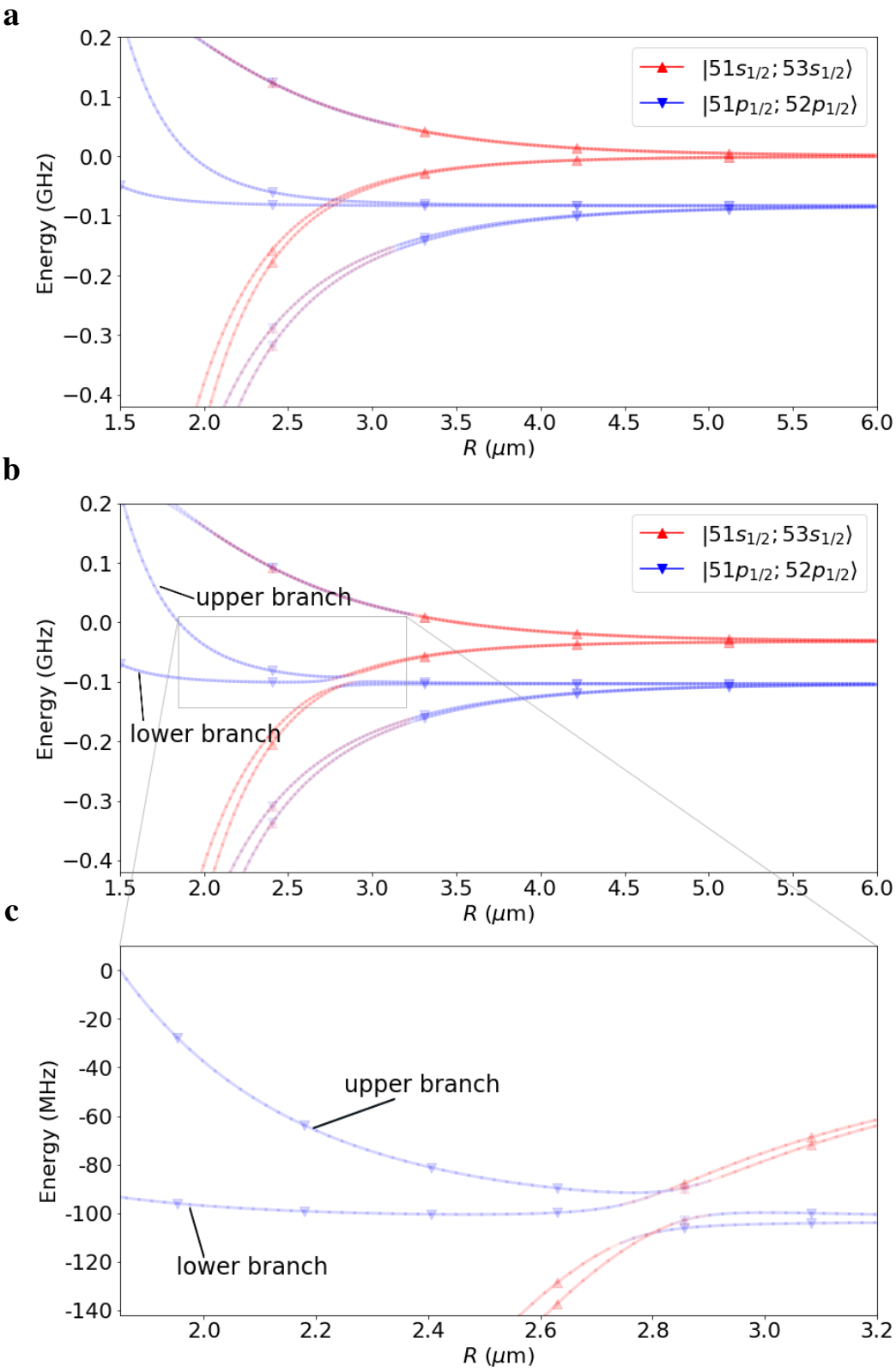

Figure 4.6.: Pair potential for two rubidium atoms calculated with PAIRINTERACTION. Energies are relative to the $|51s_{1/2};53s_{1/2}\rangle$ asymptote at infinite interatomic distance. Potential curves of the $|51s_{1/2};53s_{1/2}\rangle$ ($|51p_{1/2};52p_{1/2}\rangle$) asymptote are plotted in red (blue) with upward (downward) triangles. **a** The pair potential in free space. **b** The pair potential at a surface distance $d = 3\,\mu$m. **c** Zoom-in on the avoided crossing region. Figure adapted from [106].

An intriguing feature of the potential wells is that they only form for surface distance $d \lesssim 4\,\mu$m and become shallower for decreasing d as depicted in figure 4.7. For $d \lesssim 1.5\,\mu$m, no potential minimum can be found anymore rendering bound states impossible. Thus, the Rydberg macrodimers are only predicted in a relatively small window of $1.5\,\mu\text{m} \lesssim d \lesssim 4\,\mu$m.

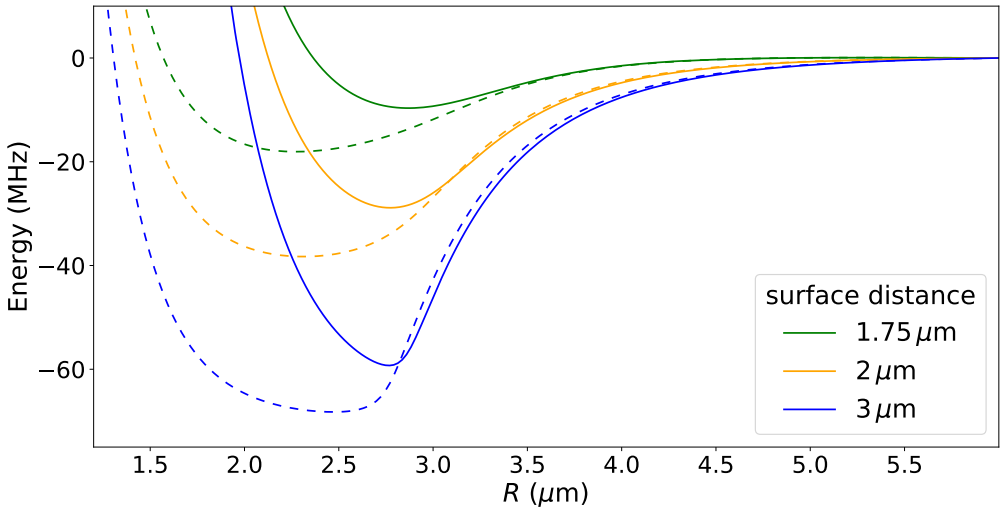

Figure 4.7.: The potential of the upper (lower) branch are plotted with solid (dashed) lines for surface distances $d = 1.75,\ 2$, and $3\,\mu$m from top to bottom. The energetic zero is taken for each potential as its respective long interatomic distance limit. The potentials wells become shallower with decreasing d and vanish eventually.

4.3.1. Rotational and electronic timescales

Dipole-quadrupole interactions as discussed here also produce rotational-electronic interactions [124]. However, due to the involved rotational and electronic timescales the rotational states can be safely ignored as it was the case in previous studies [125]. In order to estimate the rotational timescale τ we model the macrodimer state by a classical dumbbell. Then, $\tau = 2\pi\langle R\rangle/(2v)$ with the relative velocity $v \approx \sqrt{k_\text{B}T/m_\text{Rb}}$ at temperature T. The temperature of a cold atom cloud can be reduced by evaporative cooling to approximately $T \approx 40\,\mu$K [126] and the macrodimer distance is extracted from the wave functions as $\langle R\rangle(\nu = 0) \approx 2.7\,\mu$m for the upper potential branch. This yields $\tau \approx 140\,\mu$s as the rotational time scale. The Casimir-Polder potential, in addition to the energy shift, also modifies the decay rate Γ of an excited atom [12; 99]. At low temperature, when absorption and emission of thermal photons do not play a role in the atomic dynamics, the rate of spontaneous decay rate Γ_d in proximity to

a surface and the free-space decay rate Γ_0 is given by [99]

$$\frac{\Gamma_d}{\Gamma_0} = \frac{3}{8}\sum_{k<n}\left(1+\frac{|d_{nk,z}|^2}{|\mathbf{d}_{nk}|^2}\right)\left(\frac{c}{\omega_{nk}d}\right)^3 \frac{\mathrm{Im}\varepsilon(\omega_{nk})}{|\varepsilon(\omega_{nk})+1|^2}. \tag{4.56}$$

Here, $\mathbf{d}_{nk}$ and $d_{nk,z}$ are the dipole transition moment between states $|k\rangle$ and $|n\rangle$ and its z-component, respectively, and ω_{kn} is the transition frequency between the states. As this model depends on the imaginary part of the permittivity, $\mathrm{Im}\varepsilon(\omega)$, the idealized assumption of a perfectly conducting surface must be disregarded. Using the Drude model (3.35) and with plasma frequency ω_p and damping constant γ for gold from [99] as well as a typical Rydberg state with $n = 50$, one finds an enhancement factor of $\Gamma_d/\Gamma_0 \approx 10$ at $d = 3\,\mu$m. The free-space lifetime of the rubidium $|50p_{1/2}\rangle$ state has been calculated to be $\approx 260\,\mu$s [127] leading to a surface-induced shorter life time of $\tau_d \approx 26\,\mu$s. Therefore, the product of the rotational lifetime and the surface-induced decay rate is $\tau\Gamma_d \gtrsim 5 > 1$ meaning that the rotational time scale is much longer than that associated with the electronic decay of the Rydberg states. This assertion is reinforced by reports of shorter lived Rydberg macrodimer states for $62s_{1/2}$ cesium atoms with vibrational lifetimes of $3-6\,\mu$s [128].

4.3.2. Vibrational macrodimer states

The potential wells that form for a surface distance $d \lesssim 4\,\mu$m in both the upper and lower potential branch are associated with Rydberg macrodimer states with vibrational quantum number ν. The contribution to the potential well from the pair states shifts from the $|51s_{1/2}; 53s_{1/2}\rangle$ asymptote at large atomic separations to mainly $|51p_{1/2}; 52p_{1/2}\rangle$ at separations $R \lesssim 2.8\,\mu$m as it can be seen by the color code from figures 4.6 **b** and **c**. This mixing of states along the potential well ensures that bound states, i.e. the macrodimers, may only exist in the adiabatic limit. In figure 4.8 the potential branches are plotted for $d = 3\,\mu$m along with the vibrational wave functions for $\nu = 0, 20, 60$ and 150 for the upper branch and $\nu = 0$ for the lower branch. The potential minima are at $E_{\mathrm{min,ub}} \approx -59.3\,$MHz for the upper potential branch and at $E_{\mathrm{min,lb}} \approx -68.2\,$MHz for the lower branch. Numerov's method [118] is used to calculate the wave functions and energies of the macrodimer states. At $d = 3\,\mu$m, there are vibrational states with a maximum quantum number $\nu_{\max} = 160$ in the upper branch and for the lower branch one finds $\nu_{\max} = 227$.

Because of the small energy gap of the avoided crossing, $\Delta_{\mathrm{ac}} \approx 13.2\,\mathrm{MHz}$, the macrodimer states might be subject to the so-called Landau-Zener predissociation [129–131]. The parameters defining the dissociation can be extracted from the adiabatic P-matrix coupling [131]. The

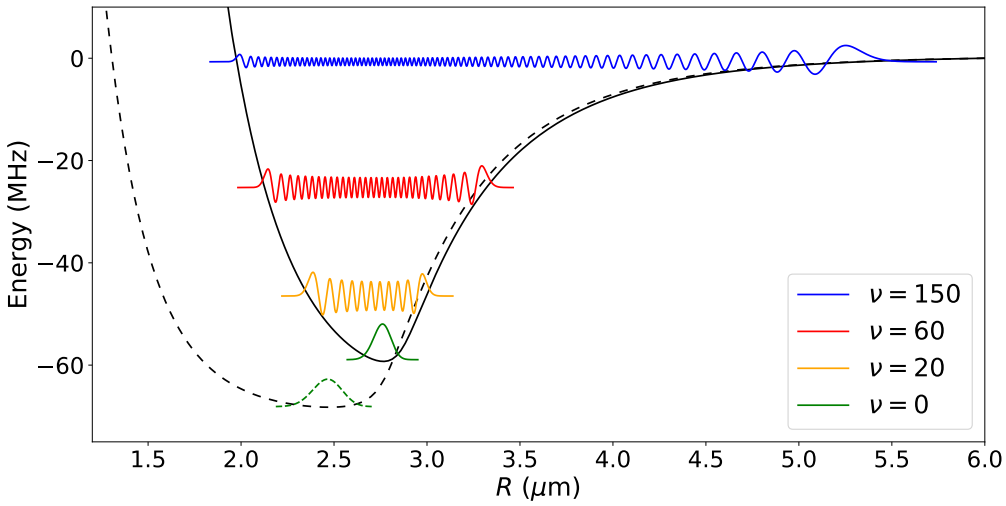

Figure 4.8.: Potential branches for $d = 3\,\mu$m. Vibrational wave functions are plotted for $\nu = 150, 60, 20, 0$ for the upper branch from top to bottom. For the lower branch, only the wave function at $\nu = 0$ is indicated. The shape of the wave functions suggest a smaller radial expectation value $\langle R \rangle$ for $\nu = 20$ than for $\nu = 0$ due to the anharmonicity of the potential. Figure adapted from [106].

P matrix is defined by the off-diagonal elements of the derivative of the interaction potential,

$$P_{12}(R) = \frac{\langle \chi_1 | (\partial/\partial R) V(R) | \chi_2 \rangle}{E_1(R) - E_2(R)}, \tag{4.57}$$

with the two atomic states $|\chi_1\rangle$ and $|\chi_2\rangle$ of the potential branch and their respective energies $E_1(R)$ and $E_2(R)$. The value of $P_{12}(R)$ peaks when the energy difference $E_1(R) - E_2(R)$ is minimum, i.e. at the avoided crossing with $E_1(R) - E_2(R) = \Delta_{\mathrm{ac}}$. The probability P_{LZ} for a nonadiabatic transition from state $|\chi_1\rangle$ to $|\chi_2\rangle$ is determined by the maximum of P_{12} and is given by

$$P_{\mathrm{LZ}} = \exp\left(-\frac{\pi^2 \Delta_{\mathrm{ac}}^2}{h v \left| \frac{\partial E_1}{\partial R} - \frac{\partial E_2}{\partial R} \right|} \right). \tag{4.58}$$

Here, v is the effective relative velocity in the lowest bound macrodimer state with a maximum that can be estimated by $v = \sqrt{2E(\nu = 0)/m}$. The derivatives $\partial E_i/\partial R$ are taken from the unperturbed potential, see figure 4.6 **a**. As equation (4.58) describes the probability of dissociation, the probability that the macrodimer will not dissociate is given by $1 - P_{\mathrm{LZ}}$. This can be matched to an exponential decay, $e^{-t^*/\tau} = 1 - P_{\mathrm{LZ}}$. Taking $t^* = h/E(\nu = 0)$ as one oscillation period of the macrodimer ground state, the resulting lifetime is $\tau = 2.83\,$ms. As

the surface-modified Rydberg state lifetime was estimated to be $\approx 25\,\mu$s in section 4.3.1, the Landau-Zener predissociation can be safely neglected.

At surface distance $d = 3\,\mu$m, the lowest bound macrodimer state has an energy $E_{\mathrm{min,ub}} = E_{\mathrm{ub}}(\nu = 0) \approx -59\,\mathrm{MHz}$ in the upper potential branch and $E_{\mathrm{lb}}(\nu = 0) \approx -68\,\mathrm{MHz}$ in the lower branch as pictured in figure 4.9. For smaller surface distances, the potential wells become shallower and, thus, the maximum binding energy decreases. The energy spacing between adjacent states $\Delta E_{\nu,\nu+1}$ is in the range of a few hundred kHz as shown in figure 4.10. The spacing is larger for the upper potential branch because of its narrower shape compared to the lower branch as it can be seen in figure 4.7. For large ν, the energy spacing shrinks and the states form a quasi-continuum. It is noteworthy that $\Delta E_{\nu,\nu+1}$ decreases monotonously with ν for the upper branch while in the lower branch it shows a maximum at $\nu = 24, 55$ and 74 for surface distances $d = 1.75, 2$,and $3\,\mu$m. This is caused by the very wide minimum region of that branch.

Taking the mean interatomic distance $\langle R\rangle = \langle\psi|R|\psi\rangle$ of the macrodimer shows the large extend of these states. For $\nu = 0$, the interatomic distance is in the range of $\langle R\rangle \approx 2.87\,\mu$m for the upper potential branch and $\langle R\rangle \approx 2.27\,\mu$m for the lower potential branch depending on surface distance d as depicted in figure 4.11. At a surface distance $d \gtrsim 2\,\mu$m, the highest excited macrodimer states reach values of $\langle R\rangle \approx 5\,\mu$m. Again, the peculiar shape of the potential wells comes into play. Due to the anharmonicity of the potential wells, the minimum $\langle R\rangle$ is achieved for excited states with $\nu = 23(44)$ for the upper (lower) branch at $d = 3\,\mu$m. The overall smallest state is $\langle R\rangle_{\mathrm{lb}}(\nu = 44) \approx 2.24\,\mu$m. The minimum of the radial expectation value being at $\nu > 0$ does not come unexpected. This behavior is already suggested by the wave functions plotted in figure 4.8 that suggest a smaller $\langle R\rangle$ for $\nu = 20$ than for $\nu = 0$ in the upper potential branch. For smaller surface distances, the minimum of the mean interatomic distance moves to smaller ν and ultimately to the vibrational ground state of the macrodimer for $d \gtrsim 2\,\mu$m.

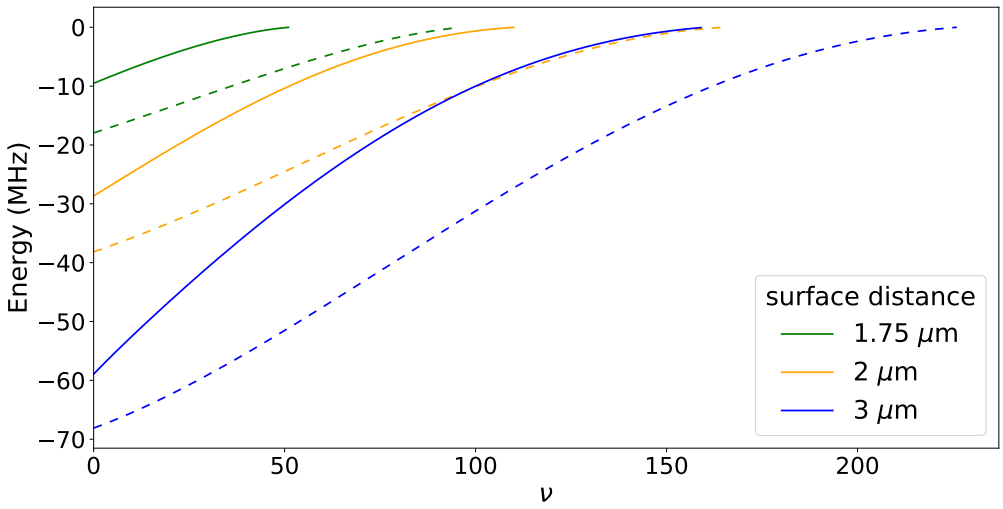

Figure 4.9.: The energy spectra of the bound macrodimer states over vibrational quantum number ν are plotted with solid (dashed) lines for the upper (lower) potential branch. For both branches, surface distances $d = 1.75, 2, 3\,\mu$m are plotted from top to bottom. Figure adapted from [106].

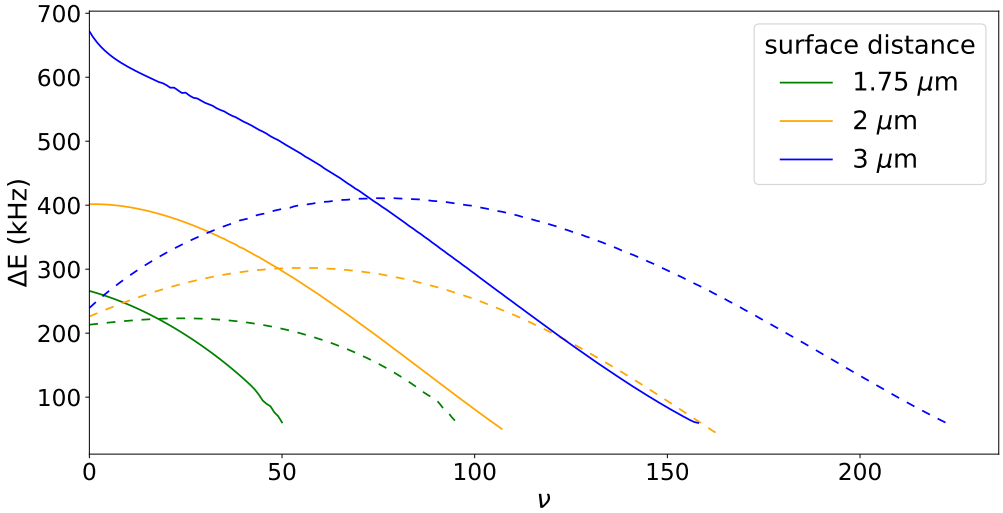

Figure 4.10.: The energy difference $\Delta E_{\nu,\nu+1}$ between adjacent vibrational macrodimer states vs vibrational quantum number ν. Solid (dashed) lines represent the upper (lower) potential branch. Figure adapted from [106].

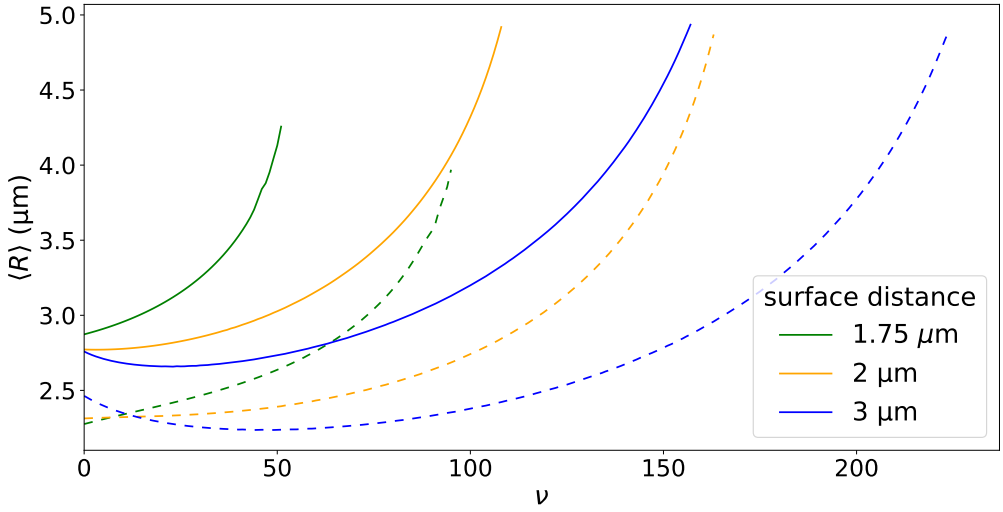

Figure 4.11.: The radial expectation value $\langle R \rangle$ of the macrodimer wave function over vibrational quantum number ν. Solid (dashed) lines represent the upper (lower) potential branch. Figure adapted from [106].

4.3.3. Rydberg molecular crystals

From the theory of atomic gases it is well-known that interatomic potentials which feature a short-range repulsive part and a long-range attractive part may lead to the formation of molecular crystals [132]. Thus, we will briefly discuss the possibility and parameters of the crystal formation for the rubidium Rydberg atoms that were discussed. The upper branch of the pair potential at $d = 2\,\mu$m, cf. figure 4.7, can be roughly approximated by a Lennard-Jones (12,6) potential of the form

$$V(R) = 4\epsilon \left[\left(\frac{\sigma}{R} \right)^{12} - \left(\frac{\sigma}{R} \right)^{6} \right]. \tag{4.59}$$

While this approximation is rather poor for small separations it fits well for larger separations past the potential minimum due to its behavior that corresponds to the van der Waals R^{-6} potential. For small separations, the R^{-12} term overestimates the potentials repulsion. However, the Lennard-Jones (12,6) potential allows one to easily fit the parameters ϵ and σ to the actual pair potential and then extract the parameters of the corresponding 2-dimensional crystal analytically. For a hexagonal lattice, one can compute the lattice sums $A_6 = 6.22$ and

$A_{12} = 6.00$ and finds for the equilibrium distance R_{eq} and cohesive energy E_{eq} [132]

$$R_{\mathrm{eq,ub}} = \left(\frac{2A_{12}}{A_6}\right)^{1/6} \sigma \approx 2.75\,\mu\mathrm{m} \tag{4.60}$$

$$E_{\mathrm{eq,ub}} = -\frac{\epsilon A_6^2}{2A_{12}} \approx 93\,\mathrm{MHz}. \tag{4.61}$$

The equilibrium distance is of the order of the expected ground state macrodimer distance ($\langle R\rangle(d = 2\,\mu\mathrm{m}) \approx 2.77\,\mu\mathrm{m}$) but the equilibrium cohesive energy is greater than the ground state energy by a factor of approximately 3.2, $E_{\mathrm{eq,ub}} = 3.2E_{\mathrm{ub}}(d = 2\,\mu\mathrm{m}, \nu = 0)$. Therefore, these results suggest that it is possible for crystals to form in an atomic ensemble near a surface. In context of a recent study of macrodimer excitation in optical lattices [80] one may add that such a lattice structure might be achievable solely by the surface-modified pair potential without additional external fields.

4.3.4. Possible experimental challenges and applications

Having discussed the theory of vibrational macrodimer states that form as a result of surface-modified pair potentials, a few comments regarding the experimental realization of such states conclude this chapter without intending to be exhaustive. The narrow energy spacing between the adjacent macrodimer states pictured in figure 4.10 requires excitation lasers with narrow linewidth. Legaie *et al.* [133] report on a sub-kilohertz linewidth laser used to excite Rydberg states of cesium. The combined energy shift from the pair potential and the Casimir-Polder shift from the unperturbed pair state is $\Delta E_{\mathrm{max}} \lesssim 170\,\mathrm{MHz}$ at the potential well minimum. The Casimir-Polder induced energy difference for the $|51s_{1/2}; 53s_{1/2}\rangle$ asymptote at $d = 1.75\,\mu$m compared to $d = 2\,\mu$m is approximately $\Delta E \sim 50\,$MHz. Therefore, selected excitation of atoms at a given surface distance at sub-micron precision is possible with common technology [58].

With atoms at short distances from a surface, unintentional adsorption of atoms to the surface will be a major challenge [134–136]. The electric field generated by the adsorbates reaches a strength of $1\mathrm{V/cm}$ at a distance of $30\,\mu$m from a copper surface for some $\sim 10^8$ adsorbed atoms [137]. This presumably hinders the observation of the effect described here, as these fields are significantly larger than those electric fields that have been used to create macrodimers in previous studies and are typically in the range of $0.1\,\mathrm{V/cm}$ [125]. Therefore, the adsorbate electric field has to be kept minimal in order to observe the surface-induced macrodimers in an experiment. One way to achieve this is to exploit the negative electron

affinity that is induced by rubidium atoms adsorbed to a quartz surface [138]. It was shown analytically in section 4.1.1 that for horizontally aligned atoms the interaction potential is reduced compared to the free-space potential. The relative potential strength 4.20 reaches a minimum at $r_p = 2/3$. Since the reduction of the potential strength contributes to the formation of the avoided crossing, non-perfect conductors may actually be the more suitable choice for the experiment. In general, all (stray) electric fields will have to be considered carefully in an experiment due to the relatively small macrodimer binding energy.

While it was stated above that macrodimers might be used to investigate the magnetoelectric properties of a given surface, the calculations are presented here only for a perfectly conducting plate. Thus, an experiment referring to these results can only assess to what degree a surface can be considered a perfect conductor. Repeating these calculations for example for dielectric materials or differently shaped objects such as spheres or nanotubes can be done by implementing the specific scattering Green's tensor to PAIRINTERACTION. A comparison of these results could yield further information and enable one to assess surface properties more accurately . However, whether macrodimers can be observed or not might give some indication regarding the specific location of an experiment. One instance where this might be a valid question are quantum reflection experiments [47–51]. The reflection at an attractive potential like the Casimir-Polder potential has been often attributed to a *badlands* region that is typically far from the strongly attractive part of the potential [139]. More recent studies emphasize the impact of the potential's short-range properties [140; 141]. Using the fact that bound macrodimers are only predicted in the small window surface distance $1.5\,\mu\mathrm{m} \lesssim d \lesssim 4\,\mu$m the observation of rubidium macrodimers in a quantum reflection experiment would indicate whether the quantum reflection process might be attributed to a certain region.

Chapter 5.

Summary and outlook

In this thesis, we have investigated surface-modified interactions between Rydberg atoms as well as surface-induced atom dynamics working our way from simple to more complex systems.

The simplest system one can imagine that includes a number of atoms and a surface is a single atom above a plain surface. In that case, the atom is subject to the Casimir-Polder potential that also affects the internal atom dynamics. We derived the equation of motion for an atomic operator $\hat{\sigma}_{mn}(t)$ in fourth order from the Heisenberg equation of motion without an external field. In order to evaluate the emerging time integrals the Markov approximation was applied. The results were then applied to a symmetric Λ-system based on the ^{87}Rb ground states. The resulting Rabi frequency between the $|5s_{1/2}, F = 2, m_F = \pm 1\rangle$ states was found to be of the order of a few hundred mrad/s at an atom-surface distance of $40\,\mathrm{nm}$ depending on the choice of the surface. These frequencies are approximately 30 to 60 times lower than those expected from second order perturbation theory [92]. Perhaps a little surprisingly the Casimir-Polder potential itself does not induce a decay rate or, in other terms, does not lead to the equal occupation of the ground states over time. In order to describe such an effect, finite lifetimes of excited states would have to be included in the calculations as the work by Reiter and Sørensen [100] suggests. While the described effects are rather small, the foundations were laid for more advanced systems. Most promising seems the inclusion of the finite lifetimes as stated above. One could either implement the finite lifetime for the intermediate state only or consider a system of (Rydberg) excited states with finite decay rates for all states. Excited states are also likely to show fast dynamics at larger surface distance [92]. Other additions to the system might be the choice of a asymmetric Λ-system with non-degenerate ground states or a structured surface. The latter suggestion is informed by the fact that corrugated surfaces

are one origin of lateral Casimir-Polder forces referred to as the contactless rack and pinion effect [93].

Chapter 4 focused on the atomic interactions between Rydberg atoms in proximity to macroscopic objects. These interactions are commonly referred to in the dipole-dipole limit as van der Waals interactions. First, these interactions were studied in the perturbative regime for two atoms above a perfect conductor and the effect of surface was calculated relative to the free-space potential. It was shown that for horizontally aligned atoms the surface leads to an effective reduction of the potential while for two atoms perpendicularly arranged above a surface the interaction strength is enhanced. These calculations allow to estimate whether effects of a surface might be visible in form of modified Rydberg blockade in experiments. At reasonable length scales the blockade radius R_{block} is reduced by approximately 6%. For high Rydberg states with $n = 100$ and unperturbed $R_{\mathrm{block}}^{\mathrm{vac}} = 14\,\mu$m [108] this translates to an effective reduction of R_{block} by $0.84\,\mu$m at surface distance $d \lesssim 2.8\,\mu$m. The interaction between two particles inside a crystal with finite permittivity ε is also enhanced [105]. The latter system can be seen as a simple model for interacting Rydberg excitons inside a semiconductor as described in [87].

Moving beyond perturbation theory the interaction Hamiltonian $\hat{H}_{\mathrm{int}}$ has to be diagonalized with respect to atomic pair states $|n, l, j, m_j; n', l', j', m_j'\rangle$. While perturbation theory yields reasonably good results, more accurate treatment becomes necessary for Rydberg atoms due to the large extend of their wave functions and large polarizability. By implementing the Green's tensor formalism into the PAIRINTERACTION we could confirm the results from perturbation theory qualitatively. Furthermore, it was possible to define the influence of the perfect conductor on the interatomic pair potential more precisely for different asymptotes of rubidium Rydberg states.

Finally, the single-atom Casimir-Polder potential was included in the calculation of the pair potential via PAIRINTERACTION leading to an additional energy shift that naturally varies for different pair states. For states of the $|51s_{1/2}; 53s_{1/2}\rangle$ and $|51p_{1/2}; 52p_{1/2}\rangle$ asymptotes, the surface-modified potential leads to the formation of an avoided crossing between the states. As a consequence potential wells form that can be associated with bound Rydberg-Rydberg states, so-called Rydberg macrodimers [106]. The potential wells only exist in a relatively narrow window of distance d from the surface with $1.5\,\mu\mathrm{m} \lesssim d \lesssim 4\,\mu\mathrm{m}$. Depending on the distance from the surface, the macrodimers have up to ~ 227 vibrational states characterized by quantum number ν. The ground state binding energies are in the range of $|E(\nu = 0)| \lesssim 68\,\mathrm{MHz}$ and the mean interatomic distance of the vibrational ground states is in the range of $\langle R\rangle \gtrsim 2.3\,\mu$m.

Using a rough analytic approximation of the pair potential in form of a Lennard-Jones (12,6) potential, the formation of surface-induced two-dimensional molecular crystals is predicted.

The effects described in this work can be of importance in high precision experiments. As it was established in the introduction, Rydberg atoms are commonly used as sensors for electric fields [2–10]. When these sensors are located in an environment at close distance to a surface the additional contributions to the level shifts and internal dynamics have to be taken into account to increase precision. Recently, Hollerith *et al.* [142] were able to identify and characterize molecular symmetries in systems of Rydberg macrodimers by shaping the pair potential at a high level of control using magnetic fields. The tunability of the potential exceeds that of conventional molecular platforms. Four-body interactions between four Rydberg atoms might lead to the observation of pairs of macrodimers [143]. These states are predicted for maximum coupling rates. Thus, together with the tuning of the interatomic potentials with magnetic fields [142] or microwave fields [144], the influence of the surface-modified interactions described in this thesis provides an additional tunable parameter in order to maximize coupling rates in the search of macrodimer pairs.

The implementation of the Green's tensor formalism into PAIRINTERACTION paves the way for future work. While the formalism is restricted to a perfectly conducting plate at the moment, this is already a good approximation for Rydberg atoms close to superconducting circuits that are proposed for qubit gates [145]. In addition, the acquired knowledge will help to implement additional Green's tensors in the future. That would allow fast and detailed calculations of Rydberg pair potentials in more complex geometries like waveguides [146; 147] or close to surfaces of finite thickness [148].

Appendix A.

The Green's Tensor

The Green's tensor $\boldsymbol{G}(\mathbf{r}, \mathbf{r}', \omega)$ was introduced in chapter 2 as the solution of the Helmholtz equation (2.109). The spatial boundary condition (2.110), the Schwarz reflection theorem (2.111) and the Onsager reciprocity (2.112) are very useful relations that often allow simplifications of equations. Additionally, the high frequency limit is

$$\lim_{|\omega|\to\infty} \frac{\omega^2}{c^2}\boldsymbol{G}(\mathbf{r}, \mathbf{r}', \omega) = -\boldsymbol{\delta}(\mathbf{r} - \mathbf{r}'). \tag{A.1}$$

Another important relation is the integral relation (2.113) that will be derived in the following. Starting from the Helmholtz equation for $\boldsymbol{G}(\mathbf{s}, \mathbf{r}', \omega$,

$$\left[\nabla_s \times \frac{1}{\mu(\mathbf{s}, \omega)}\nabla_s \times -\frac{\omega^2}{c^2}\varepsilon(\mathbf{s}, \omega)\right] \boldsymbol{G}(\mathbf{s}, \mathbf{r}', \omega) = \boldsymbol{\delta}(\mathbf{s} - \mathbf{r}'), \tag{A.2}$$

one multiplies (A.2) with $\boldsymbol{G}^*(\mathbf{r}, \mathbf{s}, \omega)$ from left and integrates over $\mathrm{d}^3 s$. After applying partial integration together with the boundary condition (2.110), one arrives at

$$\begin{aligned} &- \int \mathrm{d}^3 s\, \boldsymbol{G}^*(\mathbf{r}, \mathbf{s}, \omega) \times \overleftarrow{\nabla}_s \cdot \frac{1}{\mu(\mathbf{s}, \omega)}\nabla_s \times \boldsymbol{G}(\mathbf{s}, \mathbf{r}', \omega) \\ &- \int \mathrm{d}^3 s\, \frac{\omega^2}{c^2}\varepsilon(\mathbf{s}, \omega)\boldsymbol{G}^*(\mathbf{r}, \mathbf{s}, \omega) \cdot \boldsymbol{G}(\mathbf{s}, \mathbf{r}', \omega) = \boldsymbol{G}^*(\mathbf{r}, \mathbf{r}', \omega). \end{aligned} \tag{A.3}$$

As the next step, one takes the complex conjugate of the left inverse of (A.2) for $\boldsymbol{G}(\mathbf{r}, \mathbf{s}, \omega)$,

$$\boldsymbol{G}^*(\mathbf{r}, \mathbf{s}, \omega)\left[\times \overleftarrow{\nabla}_s \frac{1}{\mu^*(\mathbf{s}, \omega)} \times \overleftarrow{\nabla} - \frac{\omega^2}{c^2}\varepsilon^*(\mathbf{s}, \omega)\right] = \boldsymbol{\delta}(\mathbf{r} - \mathbf{s}). \tag{A.4}$$

Now, one multiplies equation (A.4) from the right with $\boldsymbol{G}(\mathbf{s},\mathbf{r}',\omega)$ and integrates over $\mathrm{d}^3 s$. Using partial integration as above, the result is

$$\begin{aligned} &-\int \mathrm{d}^3 s\, \boldsymbol{G}^*(\mathbf{r},\mathbf{s},\omega) \times \overleftarrow{\nabla}_s \cdot \frac{1}{\mu^*(\mathbf{s},\omega)} \nabla_s \times \boldsymbol{G}(\mathbf{s},\mathbf{r}',\omega) \\ &-\int \mathrm{d}^3 s\, \frac{\omega^2}{c^2} \varepsilon^*(\mathbf{s},\omega) \boldsymbol{G}^*(\mathbf{r},\mathbf{s},\omega) \cdot \boldsymbol{G}(\mathbf{s},\mathbf{r}',\omega) = \boldsymbol{G}(\mathbf{r},\mathbf{r}',\omega). \end{aligned} \tag{A.5}$$

Now, subtracting equation (A.3) from (A.5) leads to

$$\begin{aligned} &-\int \mathrm{d}^3 s\, \boldsymbol{G}^*(\mathbf{r},\mathbf{s},\omega) \times \overleftarrow{\nabla}_s \cdot \frac{\mathrm{Im}\mu(\mathbf{s},\omega)}{|\mu(\mathbf{s},\omega)|^2} \nabla_s \times \boldsymbol{G}^(\mathbf{s},\mathbf{r}',\omega) \\ &+\int \mathrm{d}^3 s\, \frac{\omega^2}{c^2} \mathrm{Im}\varepsilon(\mathbf{s},\omega) \boldsymbol{G}^*(\mathbf{r},\mathbf{s},\omega) \cdot \boldsymbol{G}(\mathbf{s},\mathbf{r}',\omega) = \mathrm{Im}\boldsymbol{G}(\mathbf{r},\mathbf{r}',\omega). \end{aligned} \tag{A.6}$$

When inserting the coefficients (2.96) and (2.97) into (A.6), the final integral relation (2.113) can be obtained,

$$\sum_{\lambda=e,m} \int \mathrm{d}^3 r''\, \boldsymbol{G}_\lambda(\mathbf{r},\mathbf{r}'',\omega) \cdot \boldsymbol{G}_\lambda^{*T}(\mathbf{r}',\mathbf{r}'',\omega) = \frac{\hbar\mu_0}{\pi} \omega^2 \mathrm{Im}\boldsymbol{G}(\mathbf{r},\mathbf{r}',\omega). \tag{A.7}$$

When considering problems with multiple regions of different magnetoelectric properties, it is useful to separate the Green's tensor into a bulk part $\boldsymbol{G}^{(0)}(\mathbf{r},\mathbf{r}',\omega)$ and a scattering part $\boldsymbol{G}^{(1)}(\mathbf{r},\mathbf{r}',\omega)$ according to (2.115). The bulk and scattering Green's tensors obey the simplified Helmholtz equation

$$\left(\nabla \times \nabla \times -k_j^2\right) \boldsymbol{G}(\mathbf{r},\mathbf{r}',\omega) = \mu_j(\omega) \boldsymbol{\delta}(\mathbf{r}-\mathbf{r}') \tag{A.8}$$

with $k_j^2 = \varepsilon_j(\omega)\mu_j(\omega)\omega^2/c^2$. The index j accounts for different regions V_j with set permittivity ε_j and permeability μ_j. The bulk tensor is the solution to equation (A.8) with $\mathbf{r},\mathbf{r}'$ in the same medium V_j described by permittivity $\varepsilon(\omega)$ and permeability $\mu(\omega)$ and is given by

$$\boldsymbol{G}^{(0)}(\mathbf{r},\mathbf{r}',\omega) = -\frac{\mu(\omega)}{3k^2}\boldsymbol{\delta}(\boldsymbol{\rho}) - \frac{\mu(\omega)e^{\mathrm{i}k\rho}}{4\pi k^2\rho^3}\left[\left(1-\mathrm{i}k\rho-k^2\rho^2\right)\boldsymbol{I} - \left(3-3\mathrm{i}k\rho-k^2\rho^2\right)\frac{\boldsymbol{\rho}\otimes\boldsymbol{\rho}}{\rho^2}\right]. \tag{A.9}$$

Here, $\boldsymbol{\rho} = \mathbf{r}-\mathbf{r}'$, $\rho = |\boldsymbol{\rho}|$ and $k = \sqrt{\varepsilon(\omega)\mu(\omega)}\omega/c$. In the nonretarded limit, i.e. $\omega\rho/c \ll 1$, and in vacuum, $\varepsilon(\mathbf{r},\omega) = \mu(\mathbf{r},\omega) = 1$, $\boldsymbol{G}^{(0)}(\mathbf{r},\mathbf{r}',\omega)$ simplifies significantly,

$$\boldsymbol{G}^{(0)}(\mathbf{r},\mathbf{r}',\omega) = -\frac{c^2}{3\omega^2}\boldsymbol{\delta}(\boldsymbol{\rho}) - \frac{c^2}{4\pi\omega^2\rho^3}\left(\boldsymbol{I} - 3\frac{\boldsymbol{\rho}\otimes\boldsymbol{\rho}}{\rho^2}\right). \tag{A.10}$$

Given equation (A.10), one can easily reproduce the well-known short-distance static limit of the atomic dipole interaction [149],

$$\begin{aligned} V_{dd} &= \lim_{\omega\to 0} -\frac{1}{\varepsilon_0}\frac{\omega^2}{c^2}\mathbf{d}_1\cdot\boldsymbol{G}^{(0)}(\mathbf{r}_1,\mathbf{r}_2,\omega)\cdot\mathbf{d}_2 \\ &= \frac{1}{4\pi\varepsilon_0}\left(\frac{\mathbf{d}_1\cdot\mathbf{d}_2}{\rho^3}-\frac{3(\mathbf{d}_1\cdot\boldsymbol{\rho})(\mathbf{d}_2\cdot\boldsymbol{\rho})}{\rho^5}\right) \end{aligned} \tag{A.11}$$

The retarded long-distance limit, $\omega\rho/c \gg 1$, leads to a ρ^{-1} dependence of the bulk Green tensor,

$$\lim_{\omega\rho/c\gg 1}\boldsymbol{G}^{(0)}(\mathbf{r},\mathbf{r}',\omega) = \frac{e^{\mathrm{i}\omega\rho/c}}{4\pi\rho}\left(\boldsymbol{I}-\frac{\boldsymbol{\rho}\otimes\boldsymbol{\rho}}{\rho^2}\right) \tag{A.12}$$

The scattering Green's tensor $\boldsymbol{G}^{(1)}(\mathbf{r},\mathbf{r}',\omega)$ is solution of the Helmholtz equation (A.8) in absence of the $\boldsymbol{\delta}$-inhomogeneity,

$$\left(\nabla\times\nabla\times-k_j^2\right)\boldsymbol{G}^{(1)}(\mathbf{r},\mathbf{r}',\omega)=\mathbf{0}. \tag{A.13}$$

It can be viewed as the propagator of a field with frequency ω from $\mathbf{r}'$ to $\mathbf{r}$ while taking into account the environment of $\mathbf{r}$ and $\mathbf{r}'$. It's low and high frequency limits are

$$\lim_{|\omega|\to 0}\frac{\omega^2}{c^2}\boldsymbol{G}^{(1)}(\mathbf{r},\mathbf{r}',\omega)=\mathbf{0}, \tag{A.14}$$

$$\lim_{|\omega|\to\infty}\frac{\omega^2}{c^2}\boldsymbol{G}^{(1)}(\mathbf{r},\mathbf{r}',\omega)=\mathbf{0}. \tag{A.15}$$

In this thesis, important special cases are the scattering Green's tensor of a dielectric plate in the nonretarded limit and in the coincidence limit $\mathbf{r}=\mathbf{r}'$ [14],

$$\boldsymbol{G}^{(1)}(\mathbf{r},\mathbf{r},\omega) = \frac{c^2}{32\pi\omega^2 z^3}\frac{\varepsilon(\omega)-1}{\varepsilon(\omega)+1}\begin{pmatrix}1&0&0\\0&1&0\\0&0&2\end{pmatrix}, \tag{A.16}$$

and the two-point Green's tensor for a perfectly conducting plate in the nonretarded limit [105],

$$\begin{aligned}\boldsymbol{G}_0(\mathbf{r}_A,\mathbf{r}_B) = -\frac{1}{4\pi}&\left[\frac{1}{\rho^3}\begin{pmatrix}1&0&0\\0&1&0\\0&0&1\end{pmatrix} - \frac{3}{\rho^5}\begin{pmatrix}x^2&0&xz_-\\0&0&0\\xz_-&0&z_-^2\end{pmatrix}\right]\\ &+\frac{1}{4\pi}\left[\frac{1}{\rho_+^3}\begin{pmatrix}1&0&0\\0&1&0\\0&0&2\end{pmatrix} - \frac{3}{\rho_+^5}\begin{pmatrix}x^2&0&-xz_+\\0&0&0\\xz_+&0&x^2\end{pmatrix}\right].\end{aligned} \tag{A.17}$$

Here, for two points at $\mathbf{r}_A$ and $\mathbf{r}_B$ in the xz-plane, $x = x_A - x_B$, $z_\pm = z_A \pm z_B$, $\rho = x^2 + z_-^2$ and $\rho_+^2 = x^2 + z_+^2$. The first line of equation (A.17) is the free space part and the second line the scattering contribution from the plate.

Appendix B.

Additional calculations for Casimir-Polder induced Rabi oscillations

B.1. Fourth order equation of motion for $\hat{\sigma}_{mn}$

In section 3.2 the equation of motion (3.20) was derived with the Liouville operator $\mathcal{L}(t)$. Here, the derivation is shown explicitly for an atomic operator $\hat{\sigma}_{mn}(t) = |m\rangle\langle n|$. In order to simplify the notation, the notation $f_{ij}(\Omega) = e^{\mathrm{i}\Omega(t_i - t_j)}$ and $f_{t3}(\Omega) = e^{\mathrm{i}\Omega(t-t_3)}$ is used. Prefactors are left out for brevity and have to be included according to the commutation relations (3.4) to (3.6).

In first order, the equation of motion reads

$$\begin{aligned}\dot{\hat{\sigma}}_{mn}(t_1) \sim \sum_k \left(\hat{\sigma}_{mk}(t_1)\mathbf{d}_{nk} - \hat{\sigma}_{kn}(t_1)\mathbf{d}_{km}\right) \cdot \mathbf{E}(\omega, t_1) \\ + \mathbf{E}^{\dagger}(\omega, t_1) \cdot \left(\mathbf{d}_{nk}\hat{\sigma}_{mk}(t_1) - \mathbf{d}_{km}\hat{\sigma}_{kn}(t_1)\right).\end{aligned} \tag{B.1}$$

For second order, the Markov approximation (3.8) has to be applied once:

$$
\begin{aligned}
\dot{\hat{\sigma}}_{mn}(t_2) \sim \int_{t_0}^{t_2} \mathrm{d}t_1 \sum_{kl} \times \Big\{ & \\
& + \left(\hat{\sigma}_{ml}(t_2)\mathbf{d}_{kl} - \hat{\sigma}_{lk}(t_2)\mathbf{d}_{lm}\right) \cdot \mathbf{E}(\omega', t_2)\mathbf{d}_{nk} \cdot \mathbf{E}(\omega, t_2) f_{21}(-\omega + \omega_{km}) \\
& + \mathbf{E}^{\dagger}(\omega', t_2) \cdot \left(\mathbf{d}_{kl}\hat{\sigma}_{ml}(t_2) - \mathbf{d}_{lm}\hat{\sigma}_{lk}(t_2)\right) \mathbf{d}_{nk} \cdot \mathbf{E}(\omega, t_2) f_{21}(-\omega + \omega_{km}) \\
& - \left(\hat{\sigma}_{kl}(t_2)\mathbf{d}_{nl} - \hat{\sigma}_{ln}(t_2)\mathbf{d}_{lk}\right) \cdot \mathbf{E}(\omega', t_2)\mathbf{d}_{km} \cdot \mathbf{E}(\omega, t_2) f_{21}(-\omega + \omega_{nk}) \\
& - \mathbf{E}^{\dagger}(\omega', t_2) \cdot \left(\mathbf{d}_{nl}\hat{\sigma}_{kl}(t_2) - \mathbf{d}_{lk}\hat{\sigma}_{ln}(t_2)\right) \mathbf{d}_{km} \cdot \mathbf{E}(\omega, t_2) f_{21}(-\omega + \omega_{nk}) \\
& + \mathbf{E}^{\dagger}(\omega, t_2) \cdot \mathbf{d}_{nk} \left(\hat{\sigma}_{ml}(t_2)\mathbf{d}_{kl} - \hat{\sigma}_{lk}(t_2)\mathbf{d}_{lm}\right) \cdot \mathbf{E}(\omega', t_2) f_{21}(\omega + \omega_{km}) \\
& + \mathbf{E}^{\dagger}(\omega, t_2) \cdot \mathbf{d}_{nk} \mathbf{E}^{\dagger}(\omega', t_2) \cdot \left(\mathbf{d}_{kl}\hat{\sigma}_{ml}(t_2) - \mathbf{d}_{lm}\hat{\sigma}_{lk}(t_2)\right) f_{21}(\omega + \omega_{km}) \\
& - \mathbf{E}^{\dagger}(\omega, t_2) \cdot \mathbf{d}_{km} \left(\hat{\sigma}_{kl}(t_2)\mathbf{d}_{nl} - \hat{\sigma}_{ln}(t_2)\mathbf{d}_{lk}\right) \cdot \mathbf{E}(\omega', t_2) f_{21}(\omega + \omega_{nk}) \\
& - \mathbf{E}^{\dagger}(\omega, t_2) \cdot \mathbf{d}_{km} \mathbf{E}^{\dagger}(\omega', t_2) \cdot \left(\mathbf{d}_{nl}\hat{\sigma}_{kl}(t_2) - \mathbf{d}_{lk}\hat{\sigma}_{ln}(t_2)\right) f_{21}(\omega + \omega_{nk}) \Big\} .
\end{aligned}
\tag{B.2}
$$

Note, that at this point only contributions with both $\mathbf{E}^{(\dagger)}(\omega)$ and $\mathbf{E}^{(\dagger)}(\omega')$ are considered. Other terms are disregarded in equation (3.20). In third order, the Markov approximation is used again. The sum runs over either r, s or p, q for any single term. For simplicity later on, terms including $\hat{\sigma}_{rs}$ stem from $\left[\mathbf{E}^{(\dagger)}(\omega'), \hat{H}\right]$ and terms including $\hat{\sigma}_{pq}$ stem from $\left[\mathbf{E}^{(\dagger)}(\omega), \hat{H}\right]$.

$$
\begin{aligned}
\dot{\hat{\sigma}}_{mn}(t_3) \sim \int_{t_0}^{t_3} \int_{t_0}^{t_2} \mathrm{d}t_1 \sum_{klrspq} \times \Big\{ & \\
& + \hat{\sigma}_{ml}(t_3)\mathbf{d}_{kl} \cdot \mathrm{Im}\boldsymbol{G}(\omega') \cdot \mathbf{d}_{rs}\hat{\sigma}_{rs}(t_3)\mathbf{d}_{nk} \cdot \mathbf{E}(\omega, t_3) f_{21}(-\omega + \omega_{km}) f_{32}(-\omega - \omega' - \omega_{lm}) \\
& + \hat{\sigma}_{ml}(t_3)\mathbf{d}_{kl} \cdot \mathbf{E}(\omega', t_3)\mathbf{d}_{nk} \cdot \mathrm{Im}\boldsymbol{G}(\omega) \cdot \mathbf{d}_{pq}\hat{\sigma}_{pq}(t_3) f_{21}(-\omega + \omega_{km}) f_{32}(-\omega - \omega' - \omega_{lm}) \\
& - \hat{\sigma}_{lk}(t_3)\mathbf{d}_{lm} \cdot \mathrm{Im}\boldsymbol{G}(\omega') \cdot \mathbf{d}_{rs}\hat{\sigma}_{rs}(t_3)\mathbf{d}_{nk} \cdot \mathbf{E}(\omega, t_3) f_{21}(-\omega + \omega_{km}) f_{32}(-\omega - \omega' + \omega_{kl}) \\
& - \hat{\sigma}_{lk}(t_3)\mathbf{d}_{lm} \cdot \mathbf{E}(\omega', t_3)\mathbf{d}_{nk} \cdot \mathrm{Im}\boldsymbol{G}(\omega) \cdot \mathbf{d}_{pq}\hat{\sigma}_{pq}(t_3) f_{21}(-\omega + \omega_{km}) f_{32}(-\omega - \omega' + \omega_{kl}) \\
& - \hat{\sigma}_{rs}(t_3)\mathbf{d}_{rs} \cdot \mathrm{Im}\boldsymbol{G}(\omega') \cdot \mathbf{d}_{kl}\hat{\sigma}_{ml}(t_3)\mathbf{d}_{nk} \cdot \mathbf{E}(\omega, t_3) f_{21}(-\omega + \omega_{km}) f_{32}(-\omega + \omega' + \omega_{lm}) \\
& + \mathbf{E}^{\dagger}(\omega', t_3) \cdot \mathbf{d}_{kl}\hat{\sigma}_{ml}(t_3)\mathbf{d}_{nk} \cdot \mathrm{Im}\boldsymbol{G}(\omega) \cdot \mathbf{d}_{pq}\hat{\sigma}_{pq}(t_3) f_{21}(-\omega + \omega_{km}) f_{32}(-\omega + \omega' + \omega_{lm}) \\
& + \hat{\sigma}_{rs}(t_3)\mathbf{d}_{rs} \cdot \mathrm{Im}\boldsymbol{G}(\omega') \cdot \mathbf{d}_{lm}\hat{\sigma}_{lk}(t_3)\mathbf{d}_{nk} \cdot \mathbf{E}(\omega, t_3) f_{21}(-\omega + \omega_{km}) f_{32}(-\omega + \omega' + \omega_{kl}) \\
& - \mathbf{E}^{\dagger}(\omega', t_3) \cdot \mathbf{d}_{lm}\hat{\sigma}_{lk}(t_3)\mathbf{d}_{nk} \cdot \mathrm{Im}\boldsymbol{G}(\omega) \cdot \mathbf{d}_{pq}\hat{\sigma}_{pq}(t_3) f_{21}(-\omega + \omega_{km}) f_{32}(-\omega + \omega' + \omega_{kl}) \\
& - \hat{\sigma}_{kl}(t_3)\mathbf{d}_{nl} \cdot \mathrm{Im}\boldsymbol{G}(\omega') \cdot \mathbf{d}_{rs}\hat{\sigma}_{rs}(t_3)\mathbf{d}_{km} \cdot \mathbf{E}(\omega, t_3) f_{21}(-\omega + \omega_{nk}) f_{32}(-\omega - \omega' + \omega_{lk}) \\
& - \hat{\sigma}_{kl}(t_3)\mathbf{d}_{nl} \cdot \mathbf{E}(\omega', t_3)\mathbf{d}_{km} \cdot \mathrm{Im}\boldsymbol{G}(\omega) \cdot \mathbf{d}_{pq}\hat{\sigma}_{pq}(t_3) f_{21}(-\omega + \omega_{nk}) f_{32}(-\omega - \omega' + \omega_{lk}) \\
& + \hat{\sigma}_{ln}(t_3)\mathbf{d}_{lk} \cdot \mathrm{Im}\boldsymbol{G}(\omega') \cdot \mathbf{d}_{rs}\hat{\sigma}_{rs}(t_3)\mathbf{d}_{km} \cdot \mathbf{E}(\omega, t_3) f_{21}(-\omega + \omega_{nk}) f_{32}(-\omega - \omega' + \omega_{nl}) \\
& + \hat{\sigma}_{ln}(t_3)\mathbf{d}_{lk} \cdot \mathbf{E}(\omega', t_3)\mathbf{d}_{km} \cdot \mathrm{Im}\boldsymbol{G}(\omega) \cdot \mathbf{d}_{pq}\hat{\sigma}_{pq}(t_3) f_{21}(-\omega + \omega_{nk}) f_{32}(-\omega - \omega' + \omega_{nl}) \\
& + \hat{\sigma}_{rs}(t_3)\mathbf{d}_{rs} \cdot \mathrm{Im}\boldsymbol{G}(\omega') \cdot \mathbf{d}_{nl}\hat{\sigma}_{kl}(t_3)\mathbf{d}_{km} \cdot \mathbf{E}(\omega, t_3) f_{21}(-\omega + \omega_{nk}) f_{32}(-\omega + \omega' + \omega_{lk})
\end{aligned}
$$

$$
\begin{aligned}
&- \mathbf{E}^{\dagger}(\omega', t_3) \cdot \mathbf{d}_{nl} \hat{\sigma}_{kl}(t_3) \mathbf{d}_{km} \cdot \mathrm{Im}\boldsymbol{G}(\omega) \cdot \mathbf{d}_{pq} \hat{\sigma}_{pq}(t_3) f_{21}(-\omega + \omega_{nk}) f_{32}(-\omega + \omega' + \omega_{lk}) \\
&- \hat{\sigma}_{rs}(t_3) \mathbf{d}_{rs} \cdot \mathrm{Im}\boldsymbol{G}(\omega') \cdot \mathbf{d}_{lk} \hat{\sigma}_{ln}(t_3) \mathbf{d}_{km} \cdot \mathbf{E}(\omega, t_3) f_{21}(-\omega + \omega_{nk}) f_{32}(-\omega + \omega' + \omega_{kl}) \\
&+ \mathbf{E}^{\dagger}(\omega', t_3) \cdot \mathbf{d}_{lk} \hat{\sigma}_{ln}(t_3) \mathbf{d}_{km} \cdot \mathrm{Im}\boldsymbol{G}(\omega) \cdot \mathbf{d}_{pq} \hat{\sigma}_{pq}(t_3) f_{21}(-\omega + \omega_{nk}) f_{32}(-\omega + \omega' + \omega_{kl}) \\
&- \hat{\sigma}_{pq}(t_3) \mathbf{d}_{pq} \cdot \mathrm{Im}\boldsymbol{G}(\omega) \cdot \mathbf{d}_{nk} \hat{\sigma}_{ml}(t_3) \mathbf{d}_{kl} \cdot \mathbf{E}(\omega', t_3) f_{21}(\omega + \omega_{km}) f_{32}(\omega - \omega' + \omega_{lm}) \\
&+ \mathbf{E}^{\dagger}(\omega, t_3) \cdot \mathbf{d}_{nk} \hat{\sigma}_{ml}(t_3) \mathbf{d}_{kl} \cdot \mathrm{Im}\boldsymbol{G}(\omega') \cdot \mathbf{d}_{rs} \hat{\sigma}_{rs}(t_3) f_{21}(\omega + \omega_{km}) f_{32}(\omega - \omega' + \omega_{lm}) \\
&+ \hat{\sigma}_{pq}(t_3) \mathbf{d}_{pq} \cdot \mathrm{Im}\boldsymbol{G}(\omega) \cdot \mathbf{d}_{nk} \hat{\sigma}_{lk}(t_3) \mathbf{d}_{lm} \cdot \mathbf{E}(\omega', t_3) f_{21}(\omega + \omega_{km}) f_{32}(\omega - \omega' + \omega_{kl} \\
&- \mathbf{E}^{\dagger}(\omega, t_3) \cdot \mathbf{d}_{nk} \hat{\sigma}_{lk}(t_3) \mathbf{d}_{lm} \cdot \mathrm{Im}\boldsymbol{G}(\omega') \cdot \mathbf{d}_{rs} \hat{\sigma}_{rs}(t_3) f_{21}(\omega + \omega_{km}) f_{32}(\omega - \omega' + \omega_{kl} \\
&- \hat{\sigma}_{pq}(t_3) \mathbf{d}_{pq} \cdot \mathrm{Im}\boldsymbol{G}(\omega) \cdot \mathbf{d}_{nk} \mathbf{E}^{\dagger}(\omega', t_3) \cdot \mathbf{d}_{kl} \hat{\sigma}_{ml}(t_3) f_{21}(\omega + \omega_{km}) f_{32}(\omega + \omega' + \omega_{lm}) \\
&- \mathbf{E}^{\dagger}(\omega, t_3) \cdot \mathbf{d}_{nk} \hat{\sigma}_{rs}(t_3) \mathbf{d}_{rs} \cdot \mathrm{Im}\boldsymbol{G}(\omega') \cdot \mathbf{d}_{kl} \hat{\sigma}_{ml}(t_3) f_{21}(\omega + \omega_{km}) f_{32}(\omega + \omega' + \omega_{lm}) \\
&+ \hat{\sigma}_{pq}(t_3) \mathbf{d}_{pq} \cdot \mathrm{Im}\boldsymbol{G}(\omega) \cdot \mathbf{d}_{nk} \mathbf{E}^{\dagger}(\omega', t_3) \cdot \mathbf{d}_{lm} \hat{\sigma}_{lk}(t_3) f_{21}(\omega + \omega_{km}) f_{32}(\omega + \omega' + \omega_{kl}) \\
&+ \mathbf{E}^{\dagger}(\omega, t_3) \cdot \mathbf{d}_{nk} \hat{\sigma}_{rs}(t_3) \mathbf{d}_{rs} \cdot \mathrm{Im}\boldsymbol{G}(\omega') \cdot \mathbf{d}_{lm} \hat{\sigma}_{lk}(t_3) f_{21}(\omega + \omega_{km}) f_{32}(\omega + \omega' + \omega_{kl}) \\
&+ \hat{\sigma}_{pq}(t_3) \mathbf{d}_{pq} \cdot \mathrm{Im}\boldsymbol{G}(\omega) \cdot \mathbf{d}_{km} \hat{\sigma}_{kl}(t_3) \mathbf{d}_{nl} \cdot \mathbf{E}(\omega', t_3) f_{21}(\omega + \omega_{nk}) f_{32}(\omega - \omega' + \omega_{lk}) \\
&- \mathbf{E}^{\dagger}(\omega, t_3) \cdot \mathbf{d}_{km} \hat{\sigma}_{kl}(t_3) \mathbf{d}_{nl} \cdot \mathrm{Im}\boldsymbol{G}(\omega') \cdot \mathbf{r}_{rs} \hat{\sigma}_{rs}(t_3) f_{21}(\omega + \omega_{nk}) f_{32}(\omega - \omega' + \omega_{lk}) \\
&- \hat{\sigma}_{pq}(t_3) \mathbf{d}_{pq} \cdot \mathrm{Im}\boldsymbol{G}(\omega) \cdot \mathbf{d}_{km} \hat{\sigma}_{ln}(t_3) \mathbf{d}_{lk} \cdot \mathbf{E}(\omega', t_3) f_{21}(\omega + \omega_{nk}) f_{32}(\omega - \omega' + \omega_{nl}) \\
&+ \mathbf{E}^{\dagger}(\omega, t_3) \cdot \mathbf{d}_{km} \hat{\sigma}_{ln}(t_3) \mathbf{d}_{lk} \cdot \mathrm{Im}\boldsymbol{G}(\omega') \cdot \mathbf{d}_{rs} \hat{\sigma}_{rs}(t_3) f_{21}(\omega + \omega_{nk}) f_{32}(\omega - \omega' + \omega_{nl}) \\
&+ \hat{\sigma}_{pq}(t_3) \mathbf{d}_{pq} \cdot \mathrm{Im}\boldsymbol{G}(\omega) \cdot \mathbf{d}_{km} \mathbf{E}^{\dagger}(\omega', t_3) \cdot \mathbf{d}_{nl} \hat{\sigma}_{kl}(t_3) f_{21}(\omega + \omega_{nk}) f_{32}(\omega + \omega' + \omega_{lk}) \\
&+ \mathbf{E}^{\dagger}(\omega, t_3) \cdot \mathbf{d}_{km} \hat{\sigma}_{rs}(t_3) \mathbf{d}_{rs} \cdot \mathrm{Im}\boldsymbol{G}(\omega') \cdot \mathbf{d}_{nl} \hat{\sigma}_{kl}(t_3) f_{21}(\omega + \omega_{nk}) f_{32}(\omega + \omega' + \omega_{lk}) \\
&- \hat{\sigma}_{pq}(t_3) \mathbf{d}_{pq} \cdot \mathrm{Im}\boldsymbol{G}(\omega) \cdot \mathbf{d}_{km} \mathbf{E}^{\dagger}(\omega', t_3) \cdot \mathbf{d}_{lk} \hat{\sigma}_{ln}(t_3) f_{21}(\omega + \omega_{nk}) f_{32}(\omega + \omega' + \omega_{nl}) \\
&- \mathbf{E}^{\dagger}(\omega, t_3) \cdot \mathbf{d}_{km} \hat{\sigma}_{rs}(t_3) \mathbf{d}_{rs} \cdot \mathrm{Im}\boldsymbol{G}(\omega') \cdot \mathbf{d}_{lk} \hat{\sigma}_{ln}(t_3) f_{21}(\omega + \omega_{nk}) f_{32}(\omega + \omega' + \omega_{nl}) \Big\} .
\end{aligned}
\tag{B.3}
$$

At this point, terms with 3 factors $\mathbf{E}^{(\dagger)}$ are omitted because they vanish after taking the vacuum expectation value in (3.20). In fourth order, Finally, after having solved the time integrals in fourth order according to (3.12), the fourth order equation of motion including all prefactors can be written as:

$$
\begin{aligned}
\dot{\hat{\sigma}}_{mn}(t) \approx -\mathrm{i} \sum_{klrspq} \int_0^{\infty} \mathrm{d}\omega \int_0^{\infty} \mathrm{d}\omega' \left(\frac{\mu_0}{\hbar\pi}\right)^2 \omega^2 \omega'^2 \times \{ \\
+ \frac{\hat{\sigma}_{mq}(t) \mathbf{d}_{kl} \cdot \mathrm{Im}\boldsymbol{G}(\omega') \cdot \mathbf{d}_{rs} \mathbf{d}_{nk} \cdot \mathrm{Im}\boldsymbol{G}(\omega) \cdot \mathbf{d}_{pq} \delta_{lr} \delta_{sp}}{(-\omega + \omega_{km} + \mathrm{i}\Gamma)(-\omega - \omega' + \omega_{lm} + \mathrm{i}\Gamma)(-\omega + \omega_{lm} + \omega_{sr} + \mathrm{i}\Gamma)} \\
+ \frac{\hat{\sigma}_{mq}(t) \mathbf{d}_{kl} \cdot \mathrm{Im}\boldsymbol{G}(\omega') \cdot \mathbf{d}_{rs} \mathbf{d}_{nk} \cdot \mathrm{Im}\boldsymbol{G}(\omega) \cdot \mathbf{d}_{pq} \delta_{lr} \delta_{sp}}{(-\omega + \omega_{km} + \mathrm{i}\Gamma)(-\omega - \omega' + \omega_{lm} + \mathrm{i}\Gamma)(-\omega' + \omega_{lm} + \omega_{qp} + \mathrm{i}\Gamma)} \\
- \frac{\hat{\sigma}_{lq}(t) \mathbf{d}_{lm} \cdot \mathrm{Im}\boldsymbol{G}(\omega') \cdot \mathbf{d}_{rs} \mathbf{d}_{nk} \cdot \mathrm{Im}\boldsymbol{G}(\omega) \cdot \mathbf{d}_{pq} \delta_{kr} \delta_{sp}}{(-\omega + \omega_{km} + \mathrm{i}\Gamma)(-\omega - \omega' + \omega_{kl} + \mathrm{i}\Gamma)(-\omega + \omega_{kl} + \omega_{sr} + \mathrm{i}\Gamma)}
\end{aligned}
$$

$$
\begin{aligned}
&- \frac{\hat{\sigma}_{lq}(t)\mathbf{d}_{lm}\cdot\mathrm{Im}\boldsymbol{G}(\omega')\cdot\mathbf{d}_{rs}\mathbf{d}_{nk}\cdot\mathrm{Im}\boldsymbol{G}(\omega)\cdot\mathbf{d}_{pq}\delta_{kr}\delta_{sp}}{(-\omega+\omega_{km}+\mathrm{i}\Gamma)(-\omega-\omega'+\omega_{kl}+\mathrm{i}\Gamma)(-\omega'+\omega_{kl}+\omega_{qp}+\mathrm{i}\Gamma)}\\
&- \frac{\hat{\sigma}_{rq}(t)\mathbf{d}_{rs}\cdot\mathrm{Im}\boldsymbol{G}(\omega')\cdot\mathbf{d}_{kl}\mathbf{d}_{nk}\cdot\mathrm{Im}\boldsymbol{G}(\omega)\cdot\mathbf{d}_{pq}\delta_{sm}\delta_{lp}}{(-\omega+\omega_{km}+\mathrm{i}\Gamma)(-\omega+\omega'+\omega_{lm}+\mathrm{i}\Gamma)(-\omega+\omega_{sr}+\omega_{lm}+\mathrm{i}\Gamma)}\\
&- \frac{\hat{\sigma}_{rq}(t)\mathbf{d}_{rs}\cdot\mathrm{Im}\boldsymbol{G}(\omega')\cdot\mathbf{d}_{kl}\mathbf{d}_{nk}\cdot\mathrm{Im}\boldsymbol{G}(\omega)\cdot\mathbf{d}_{pq}\delta_{sm}\delta_{lp}}{(-\omega+\omega_{km}+\mathrm{i}\Gamma)(-\omega+\omega'+\omega_{lm}+\mathrm{i}\Gamma)(\omega'+\omega_{lm}+\omega_{qp}+\mathrm{i}\Gamma)}\\
&+ \frac{\hat{\sigma}_{rq}(t)\mathbf{d}_{rs}\cdot\mathrm{Im}\boldsymbol{G}(\omega')\cdot\mathbf{d}_{lm}\mathbf{d}_{nk}\cdot\mathrm{Im}\boldsymbol{G}(\omega)\cdot\mathbf{d}_{pq}\delta_{sl}\delta_{kp}}{(-\omega+\omega_{km}+\mathrm{i}\Gamma)(-\omega+\omega'+\omega_{kl}+\mathrm{i}\Gamma)(-\omega+\omega_{sr}+\omega_{kl}+\mathrm{i}\Gamma)}\\
&+ \frac{\hat{\sigma}_{rq}(t)\mathbf{d}_{rs}\cdot\mathrm{Im}\boldsymbol{G}(\omega')\cdot\mathbf{d}_{lm}\mathbf{d}_{nk}\cdot\mathrm{Im}\boldsymbol{G}(\omega)\cdot\mathbf{d}_{pq}\delta_{sl}\delta_{kp}}{(-\omega+\omega_{km}+\mathrm{i}\Gamma)(-\omega+\omega'+\omega_{kl}+\mathrm{i}\Gamma)(\omega'+\omega_{kl}+\omega_{qp}+\mathrm{i}\Gamma)}\\
&- \frac{\hat{\sigma}_{kq}(t)\mathbf{d}_{nl}\cdot\mathrm{Im}\boldsymbol{G}(\omega')\cdot\mathbf{d}_{rs}\mathbf{d}_{km}\cdot\mathrm{Im}\boldsymbol{G}(\omega)\cdot\mathbf{d}_{pq}\delta_{lr}\delta_{sp}}{(-\omega+\omega_{nk}+\mathrm{i}\Gamma)(-\omega-\omega'+\omega_{lk}+\mathrm{i}\Gamma)(-\omega+\omega_{lk}+\omega_{sr}+\mathrm{i}\Gamma)}\\
&- \frac{\hat{\sigma}_{kq}(t)\mathbf{d}_{nl}\cdot\mathrm{Im}\boldsymbol{G}(\omega')\cdot\mathbf{d}_{rs}\mathbf{d}_{km}\cdot\mathrm{Im}\boldsymbol{G}(\omega)\cdot\mathbf{d}_{pq}\delta_{lr}\delta_{sp}}{(-\omega+\omega_{nk}+\mathrm{i}\Gamma)(-\omega-\omega'+\omega_{lk}+\mathrm{i}\Gamma)(-\omega'+\omega_{lk}+\omega_{qp}+\mathrm{i}\Gamma)}\\
&+ \frac{\hat{\sigma}_{lq}(t)\mathbf{d}_{lk}\cdot\mathrm{Im}\boldsymbol{G}(\omega')\cdot\mathbf{d}_{rs}\mathbf{d}_{km}\cdot\mathrm{Im}\boldsymbol{G}(\omega)\cdot\mathbf{d}_{pq}\delta_{nr}\delta_{sp}}{(-\omega+\omega_{nk}+\mathrm{i}\Gamma)(-\omega-\omega'+\omega_{nl}+\mathrm{i}\Gamma)(-\omega+\omega_{nl}+\omega_{sr}+\mathrm{i}\Gamma)}\\
&+ \frac{\hat{\sigma}_{lq}(t)\mathbf{d}_{lk}\cdot\mathrm{Im}\boldsymbol{G}(\omega')\cdot\mathbf{d}_{rs}\mathbf{d}_{km}\cdot\mathrm{Im}\boldsymbol{G}(\omega)\cdot\mathbf{d}_{pq}\delta_{nr}\delta_{sp}}{(-\omega+\omega_{nk}+\mathrm{i}\Gamma)(-\omega-\omega'+\omega_{nl}+\mathrm{i}\Gamma)(-\omega'+\omega_{nl}+\omega_{qp}+\mathrm{i}\Gamma)}\\
&+ \frac{\hat{\sigma}_{rq}(t)\mathbf{d}_{rs}\cdot\mathrm{Im}\boldsymbol{G}(\omega')\cdot\mathbf{d}_{nl}\mathbf{d}_{km}\cdot\mathrm{Im}\boldsymbol{G}(\omega)\cdot\mathbf{d}_{pq}\delta_{sk}\delta_{lp}}{(-\omega+\omega_{nk}+\mathrm{i}\Gamma)(-\omega+\omega'+\omega_{lk}+\mathrm{i}\Gamma)(-\omega+\omega_{sr}+\omega_{lk}+\mathrm{i}\Gamma)}\\
&+ \frac{\hat{\sigma}_{rq}(t)\mathbf{d}_{rs}\cdot\mathrm{Im}\boldsymbol{G}(\omega')\cdot\mathbf{d}_{nl}\mathbf{d}_{km}\cdot\mathrm{Im}\boldsymbol{G}(\omega)\cdot\mathbf{d}_{pq}\delta_{sk}\delta_{lp}}{(-\omega+\omega_{nk}+\mathrm{i}\Gamma)(-\omega+\omega'+\omega_{lk}+\mathrm{i}\Gamma)(\omega'+\omega_{lk}+\omega_{qp}+\mathrm{i}\Gamma)}\\
&- \frac{\hat{\sigma}_{rq}(t)\mathbf{d}_{rs}\cdot\mathrm{Im}\boldsymbol{G}(\omega')\cdot\mathbf{d}_{lk}\mathbf{d}_{km}\cdot\mathrm{Im}\boldsymbol{G}(\omega)\cdot\mathbf{d}_{pq}\delta_{sl}\delta_{np}}{(-\omega+\omega_{nk}+\mathrm{i}\Gamma)(-\omega+\omega'+\omega_{nl}+\mathrm{i}\Gamma)(-\omega+\omega_{sr}+\omega_{nl}+\mathrm{i}\Gamma)}\\
&- \frac{\hat{\sigma}_{rq}(t)\mathbf{d}_{rs}\cdot\mathrm{Im}\boldsymbol{G}(\omega')\cdot\mathbf{d}_{lk}\mathbf{d}_{km}\cdot\mathrm{Im}\boldsymbol{G}(\omega)\cdot\mathbf{d}_{pq}\delta_{sl}\delta_{np}}{(-\omega+\omega_{nk}+\mathrm{i}\Gamma)(-\omega+\omega'+\omega_{nl}+\mathrm{i}\Gamma)(\omega'+\omega_{nl}+\omega_{qp}+\mathrm{i}\Gamma)}\\
&- \frac{\hat{\sigma}_{ps}(t)\mathbf{d}_{pq}\cdot\mathrm{Im}\boldsymbol{G}(\omega)\cdot\mathbf{d}_{nk}\mathbf{d}_{kl}\cdot\mathrm{Im}\boldsymbol{G}(\omega')\cdot\mathbf{d}_{rs}\delta_{qm}\delta_{lr}}{(\omega+\omega_{km}+\mathrm{i}\Gamma)(\omega-\omega'+\omega_{lm}+\mathrm{i}\Gamma)(-\omega'+\omega_{qp}+\omega_{lm}+\mathrm{i}\Gamma)}\\
&- \frac{\hat{\sigma}_{ps}(t)\mathbf{d}_{pq}\cdot\mathrm{Im}\boldsymbol{G}(\omega)\cdot\mathbf{d}_{nk}\mathbf{d}_{kl}\cdot\mathrm{Im}\boldsymbol{G}(\omega')\cdot\mathbf{d}_{rs}\delta_{qm}\delta_{lr}}{(\omega+\omega_{km}+\mathrm{i}\Gamma)(\omega-\omega'+\omega_{lm}+\mathrm{i}\Gamma)(\omega+\omega_{lm}+\omega_{sr}+\mathrm{i}\Gamma)}\\
&+ \frac{\hat{\sigma}_{ps}(t)\mathbf{d}_{pq}\cdot\mathrm{Im}\boldsymbol{G}(\omega)\cdot\mathbf{d}_{nk}\mathbf{d}_{lm}\cdot\mathrm{Im}\boldsymbol{G}(\omega')\cdot\mathbf{d}_{rs}\delta_{ql}\delta_{kr}}{(\omega+\omega_{km}+\mathrm{i}\Gamma)(\omega-\omega'+\omega_{kl}+\mathrm{i}\Gamma)(-\omega'+\omega_{qp}+\omega_{kl}+\mathrm{i}\Gamma)}\\
&+ \frac{\hat{\sigma}_{ps}(t)\mathbf{d}_{pq}\cdot\mathrm{Im}\boldsymbol{G}(\omega)\cdot\mathbf{d}_{nk}\mathbf{d}_{lm}\cdot\mathrm{Im}\boldsymbol{G}(\omega')\cdot\mathbf{d}_{rs}\delta_{ql}\delta_{kr}}{(\omega+\omega_{km}+\mathrm{i}\Gamma)(\omega-\omega'+\omega_{kl}+\mathrm{i}\Gamma)(\omega+\omega_{kl}+\omega_{sr}+\mathrm{i}\Gamma)}\\
&+ \frac{\hat{\sigma}_{pl}(t)\mathbf{d}_{pq}\cdot\mathrm{Im}\boldsymbol{G}(\omega)\cdot\mathbf{d}_{nk}\mathbf{d}_{rs}\cdot\mathrm{Im}\boldsymbol{G}(\omega')\cdot\mathbf{d}_{kl}\delta_{qr}\delta_{sm}}{(\omega+\omega_{km}+\mathrm{i}\Gamma)(\omega+\omega'+\omega_{lm}+\mathrm{i}\Gamma)(\omega'+\omega_{qp}+\omega_{lm}+\mathrm{i}\Gamma)}\\
&+ \frac{\hat{\sigma}_{pl}(t)\mathbf{d}_{pq}\cdot\mathrm{Im}\boldsymbol{G}(\omega)\cdot\mathbf{d}_{nk}\mathbf{d}_{rs}\cdot\mathrm{Im}\boldsymbol{G}(\omega')\cdot\mathbf{d}_{kl}\delta_{qr}\delta_{sm}}{(\omega+\omega_{km}+\mathrm{i}\Gamma)(\omega+\omega'+\omega_{lm}+\mathrm{i}\Gamma)(\omega+\omega_{sr}+\omega_{lm}+\mathrm{i}\Gamma)}\\
&- \frac{\hat{\sigma}_{pk}(t)\mathbf{d}_{pq}\cdot\mathrm{Im}\boldsymbol{G}(\omega)\cdot\mathbf{d}_{nk}\mathbf{d}_{rs}\cdot\mathrm{Im}\boldsymbol{G}(\omega')\cdot\mathbf{d}_{lm}\delta_{qr}\delta_{sl}}{(\omega+\omega_{km}+\mathrm{i}\Gamma)(\omega+\omega'+\omega_{kl}+\mathrm{i}\Gamma)(\omega'+\omega_{qp}+\omega_{kl}+\mathrm{i}\Gamma)}
\end{aligned}
$$

$$
\begin{aligned}
&- \frac{\hat{\sigma}_{pk}(t)\mathbf{d}_{pq}\cdot\mathrm{Im}\boldsymbol{G}(\omega)\cdot\mathbf{d}_{nk}\mathbf{d}_{rs}\cdot\mathrm{Im}\boldsymbol{G}(\omega')\cdot\mathbf{d}_{lm}\delta_{qr}\delta_{sl}}{(\omega+\omega_{km}+\mathrm{i}\Gamma)(\omega+\omega'+\omega_{kl}+\mathrm{i}\Gamma)(\omega+\omega_{sr}+\omega_{kl}+\mathrm{i}\Gamma)} \\
&+ \frac{\hat{\sigma}_{ps}(t)\mathbf{d}_{pq}\cdot\mathrm{Im}\boldsymbol{G}(\omega)\cdot\mathbf{d}_{km}\mathbf{d}_{nl}\cdot\mathrm{Im}\boldsymbol{G}(\omega')\cdot\mathbf{d}_{rs}\delta_{qk}\delta_{lr}}{(\omega+\omega_{nk}+\mathrm{i}\Gamma)(\omega-\omega'+\omega_{lk}+\mathrm{i}\Gamma)(-\omega'+\omega_{qp}+\omega_{lk}+\mathrm{i}\Gamma)} \\
&+ \frac{\hat{\sigma}_{ps}(t)\mathbf{d}_{pq}\cdot\mathrm{Im}\boldsymbol{G}(\omega)\cdot\mathbf{d}_{km}\mathbf{d}_{nl}\cdot\mathrm{Im}\boldsymbol{G}(\omega')\cdot\mathbf{d}_{rs}\delta_{qk}\delta_{lr}}{(\omega+\omega_{nk}+\mathrm{i}\Gamma)(\omega-\omega'+\omega_{lk}+\mathrm{i}\Gamma)(\omega+\omega_{lk}+\omega_{sr}+\mathrm{i}\Gamma)} \\
&- \frac{\hat{\sigma}_{ps}(t)\mathbf{d}_{pq}\cdot\mathrm{Im}\boldsymbol{G}(\omega)\cdot\mathbf{d}_{km}\mathbf{d}_{lk}\cdot\mathrm{Im}\boldsymbol{G}(\omega')\cdot\mathbf{d}_{rs}\delta_{ql}\delta_{nr}}{(\omega+\omega_{nk}+\mathrm{i}\Gamma)(\omega-\omega'+\omega_{nl}+\mathrm{i}\Gamma)(-\omega'+\omega_{qp}+\omega_{nl}+\mathrm{i}\Gamma)} \\
&- \frac{\hat{\sigma}_{ps}(t)\mathbf{d}_{pq}\cdot\mathrm{Im}\boldsymbol{G}(\omega)\cdot\mathbf{d}_{km}\mathbf{d}_{lk}\cdot\mathrm{Im}\boldsymbol{G}(\omega')\cdot\mathbf{d}_{rs}\delta_{ql}\delta_{nr}}{(\omega+\omega_{nk}+\mathrm{i}\Gamma)(\omega-\omega'+\omega_{nl}+\mathrm{i}\Gamma)(\omega+\omega_{nl}+\omega_{sr}+\mathrm{i}\Gamma)} \\
&- \frac{\hat{\sigma}_{pl}(t)\mathbf{d}_{pq}\cdot\mathrm{Im}\boldsymbol{G}(\omega)\cdot\mathbf{d}_{km}\mathbf{d}_{rs}\cdot\mathrm{Im}\boldsymbol{G}(\omega')\cdot\mathbf{d}_{nl}\delta_{qr}\delta_{sk}}{(\omega+\omega_{nk}+\mathrm{i}\Gamma)(\omega+\omega'+\omega_{lk}+\mathrm{i}\Gamma)(\omega'+\omega_{qp}+\omega_{lk}+\mathrm{i}\Gamma)} \\
&- \frac{\hat{\sigma}_{pl}(t)\mathbf{d}_{pq}\cdot\mathrm{Im}\boldsymbol{G}(\omega)\cdot\mathbf{d}_{km}\mathbf{d}_{rs}\cdot\mathrm{Im}\boldsymbol{G}(\omega')\cdot\mathbf{d}_{nl}\delta_{qr}\delta_{sk}}{(\omega+\omega_{nk}+\mathrm{i}\Gamma)(\omega+\omega'+\omega_{lk}+\mathrm{i}\Gamma)(\omega+\omega_{sr}+\omega_{lk}+\mathrm{i}\Gamma)} \\
&+ \frac{\hat{\sigma}_{pn}(t)\mathbf{d}_{pq}\cdot\mathrm{Im}\boldsymbol{G}(\omega)\cdot\mathbf{d}_{km}\mathbf{d}_{rs}\cdot\mathrm{Im}\boldsymbol{G}(\omega')\cdot\mathbf{d}_{lk}\delta_{qr}\delta_{sl}}{(\omega+\omega_{nk}+\mathrm{i}\Gamma)(\omega+\omega'+\omega_{nl}+\mathrm{i}\Gamma)(\omega'+\omega_{qp}+\omega_{nl}+\mathrm{i}\Gamma)} \\
&+ \frac{\hat{\sigma}_{pn}(t)\mathbf{d}_{pq}\cdot\mathrm{Im}\boldsymbol{G}(\omega)\cdot\mathbf{d}_{km}\mathbf{d}_{rs}\cdot\mathrm{Im}\boldsymbol{G}(\omega')\cdot\mathbf{d}_{lk}\delta_{qr}\delta_{sl}}{(\omega+\omega_{nk}+\mathrm{i}\Gamma)(\omega+\omega'+\omega_{nl}+\mathrm{i}\Gamma)(\omega+\omega_{sr}+\omega_{nl}+\mathrm{i}\Gamma)}\Bigg\}. \qquad \text{(B.4)}
\end{aligned}
$$

Here, the relation $\hat{\sigma}_{mn}(t)\hat{\sigma}_{ij}(t) = \hat{\sigma}_{mj}(t)\delta_{ni}$ was used.

B.2. Calculation of the frequency integrals

Here, calculations for the two terms in equation (3.25) in section 3.3 are shown in detail. The first term has a linear pole at and the second term a quadratic pole at $\omega = \omega_{km}$, so contour integration techniques are applied.

B.2.1. Linear pole on real axis

Omitting the prefactors, the first term of equation 3.25 is

$$
\int_0^\infty \mathrm{d}\omega \int_0^\infty \mathrm{d}\omega'\, \mathcal{T}_1 = \int_0^\infty \mathrm{d}\omega \int_0^\infty \mathrm{d}\omega' \left\{ \frac{\omega^2 \mathrm{Im}G(\omega)\omega'^2 \mathrm{Im}G(\omega')}{(\omega-\omega_{km})(\omega'+\omega_{km})(\omega+\omega')} \right\}, \qquad \text{(B.5)}
$$

where the Green's tensor is split into frequency dependent part $G(\omega)$ and frequency independent matrix part $\tilde{\boldsymbol{G}}$ according to (A.16). The $\mathrm{d}\omega$-integral is performed first. To this end, one has to include the convergence factor $\mathrm{i}\Gamma$ from substitution (3.11) that was needed to solve the time

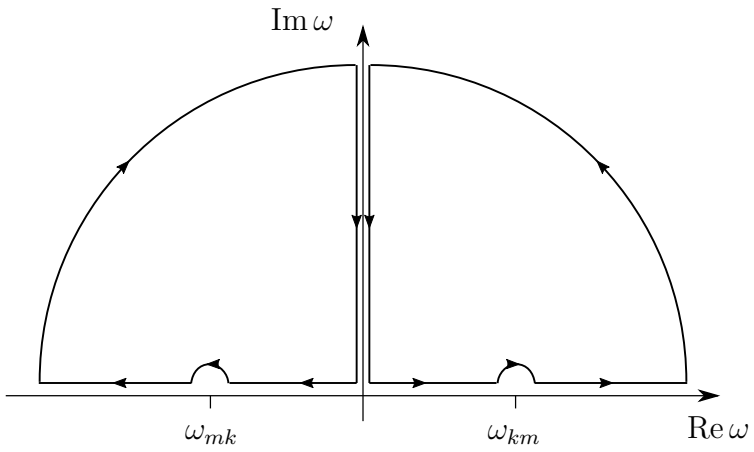

Figure B.1.: The integration contour for poles on the real axis. The integral along the quarter circles vanishes because of the high frequency limit (A.15) of the Green's tensor.

integral. Depending on the actual term, the convergence factor has positive or negative sign in these integrals as it can be easily seen from equation (B.4).

$$\int_0^\infty \mathrm{d}\omega\, \frac{\omega^2 \mathrm{Im}G(\omega)}{(\omega-\omega_{km}\pm \mathrm{i}\Gamma)(\omega+\omega')} = \mathcal{P}\int_0^\infty \mathrm{d}\omega\, \frac{\omega^2 \mathrm{Im}G(\omega)}{(\omega-\omega_{km})(\omega+\omega')} \mp \mathrm{i}\pi \frac{\omega_{km}^2 \mathrm{Im}G(\omega_{km})}{\omega'+\omega_{km}}. \tag{B.6}$$

Now, the principal value integral can be solved by firstly splitting the imaginary part of the Green's tensor according to $\mathrm{Im}G(\omega) = (G(\omega) - G(-\omega))/2\mathrm{i}$, so that

$$\begin{aligned}\mathcal{P}\int_0^\infty \mathrm{d}\omega\, \frac{\omega^2 \mathrm{Im}G(\omega)}{(\omega-\omega_{km})(\omega+\omega')} &= \frac{\mathcal{P}}{2\mathrm{i}}\int_0^\infty \mathrm{d}\omega\, \frac{\omega^2 G(\omega)}{(\omega-\omega_{km})(\omega+\omega')} \\ &\quad - \frac{\mathcal{P}}{2\mathrm{i}}\int_0^\infty \mathrm{d}\omega\, \frac{\omega^2 G(-\omega)}{(\omega-\omega_{km})(\omega+\omega')} \qquad \text{(B.7)} \\ &= \frac{\mathcal{P}}{2\mathrm{i}}\int_0^\infty \mathrm{d}\omega\, \frac{\omega^2 G(\omega)}{(\omega-\omega_{km})(\omega+\omega')} \\ &\quad + \frac{\mathcal{P}}{2\mathrm{i}}\int_0^{-\infty} \mathrm{d}\omega\, \frac{\omega^2 G(\omega)}{(\omega+\omega_{km})(\omega-\omega')}. \qquad \text{(B.8)}\end{aligned}$$

At this point, one can integrate along the integration contour from figure B.1. The integral along the quarter circles vanishes because of the high frequency limit (A.15). Therefore, the

principal value integral is

$$\begin{aligned}\mathcal{P}\int_0^\infty \mathrm{d}\omega\,\frac{\omega^2 \mathrm{Im}G(\omega)}{(\omega-\omega_{km})(\omega+\omega')} &= \frac{1}{2}\int_0^\infty \mathrm{d}\xi\,\frac{(\mathrm{i}\xi)^2 G(\mathrm{i}\xi)}{(\mathrm{i}\xi-\omega_{km})(\mathrm{i}\xi+\omega')} \\ &\quad + \frac{1}{2}\int_0^\infty \mathrm{d}\xi\,\frac{(\mathrm{i}\xi)^2 G(\mathrm{i}\xi)}{(\mathrm{i}\xi+\omega_{km})(\mathrm{i}\xi-\omega')} \\ &\quad + \frac{\pi}{2}\frac{\omega_{km}^2 G(\omega_{km})}{\omega'+\omega_{km}} - \frac{\pi}{2}\frac{\omega_{km}^2 G(-\omega_{km})}{-\omega'-\omega_{km}} \qquad \text{(B.9)} \\ &= \int_0^\infty \mathrm{d}\xi\,(\mathrm{i}\xi)^2 G(\mathrm{i}\xi)\mathrm{Re}\left[\frac{1}{(\mathrm{i}\xi-\omega_{km})(\mathrm{i}\xi+\omega')}\right] \\ &\quad + \pi\frac{\omega_{km}^2 \mathrm{Re}G(\omega_{km})}{\omega'+\omega_{km}}. \qquad \text{(B.10)}\end{aligned}$$

This leaves for the full $\mathrm{d}\omega$ integral including the residue term

$$\begin{aligned}\int_0^\infty \mathrm{d}\omega\,\frac{\omega^2 \mathrm{Im}G(\omega)}{(\omega-\omega_{km}\pm\mathrm{i}\Gamma)(\omega+\omega')} &= \int_0^\infty \mathrm{d}\xi\,(\mathrm{i}\xi)^2 G(\mathrm{i}\xi)\mathrm{Re}\left[\frac{1}{(\mathrm{i}\xi-\omega_{km})(\mathrm{i}\xi+\omega')}\right] \\ &\quad + \pi\frac{\omega_{km}^2 G(\mp\omega_{km})}{\omega'+\omega_{km}}. \qquad \text{(B.11)}\end{aligned}$$

Having transformed the integral like this, the $\mathrm{d}\omega'$ integration may be carried out numerically without any poles,

$$\begin{aligned}&\int_0^\infty \mathrm{d}\omega\int_0^\infty \mathrm{d}\omega'\,\mathcal{T}_1 \\ &= \int_0^\infty \mathrm{d}\omega'\,\frac{\omega'^2 \mathrm{Im}G(\omega')}{\omega'+\omega_{km}} \\ &\quad\times\left\{\int_0^\infty \mathrm{d}\xi\,(\mathrm{i}\xi)^2 G(\mathrm{i}\xi)\mathrm{Re}\left[\frac{1}{(\mathrm{i}\xi-\omega_{km})(\mathrm{i}\xi+\omega')}\right]\pi\frac{\omega_{km}^2}{\omega'+\omega_{km}}G(\mp\omega_{km})\right\}\end{aligned} \qquad \text{(B.12)}$$

Note, that the negative (positive) sign of the residue term proportional $G(\mp\omega_{km})$ results in an overall negative (positive) sign of the imaginary part. Together with the leading factor $-\mathrm{i}$ in equation (3.25), one finds that the change of sign of $\mathrm{i}\Gamma$ leads to the negative complex conjugate, i.e. $a(+\mathrm{i}\Gamma) = -a^*(-\mathrm{i}\Gamma)$, which, in turn, leads to the elements in the matrix $\mathbf{A}$ in equation (3.28).

B.2.2. Quadratic pole on real axis

The second integral features a quadratic pole at $\omega = \omega_{km}$,

$$\int_0^\infty \mathrm{d}\omega \int_0^\infty \mathrm{d}\omega'\, \mathcal{T}_2 = \int_0^\infty \mathrm{d}\omega \int_0^\infty \mathrm{d}\omega' \, \frac{\omega^2 \mathrm{Im}G(\omega)\omega'^2 \mathrm{Im}G(\omega')}{(\omega-\omega_{km})^2(\omega+\omega')} \tag{B.13}$$

Again, the $\mathrm{d}\omega$ integral is performed first. Integration by parts is applied along with the low and high frequency limits of $G(\omega)$, equation (A.14) and (A.15), respectively. Therefore,

$$\begin{aligned}\int_0^\infty \mathrm{d}\omega \, \frac{\omega^2 \mathrm{Im}G(\omega)}{(\omega-\omega_{km}\pm \mathrm{i}\Gamma)^2(\omega+\omega')} &= \int_0^\infty \mathrm{d}\omega \, \frac{1}{(\omega-\omega_{km}\pm \mathrm{i}\Gamma)} \frac{\partial}{\partial\omega} \frac{\omega^2 \mathrm{Im}G(\omega)}{\omega+\omega'} \qquad \text{(B.14)}\\ &= \mathcal{P}\int_0^\infty \mathrm{d}\omega \, \frac{1}{(\omega-\omega_{km})} \frac{\partial}{\partial\omega} \frac{\omega^2 \mathrm{Im}G(\omega)}{\omega+\omega'} \\ &\quad \mp \mathrm{i}\pi \, \frac{\partial}{\partial\omega} \frac{\mathrm{Im}G(\omega)}{\omega+\omega'}\bigg|_{\omega=\omega_{km}} \qquad \text{(B.15)}\end{aligned}$$

Again, the focus is on the principal value integral. One can repeat the steps from section B.2.1,

$$\begin{aligned}\mathcal{P}\int_0^\infty \frac{\mathrm{d}\omega}{(\omega-\omega_{km})} \frac{\partial}{\partial\omega} \frac{\omega^2 \mathrm{Im}G(\omega)}{\omega+\omega'} &= \frac{\mathcal{P}}{2\mathrm{i}}\int_0^\infty \frac{\mathrm{d}\omega}{(\omega-\omega_{km})} \frac{\partial}{\partial\omega} \frac{\omega^2 G(\omega)}{\omega+\omega'} \\ &\quad - \frac{\mathcal{P}}{2\mathrm{i}}\int_0^{-\infty} \frac{(-\mathrm{d}\omega)}{(-1)(\omega+\omega_{km})} \frac{\partial}{\partial(-\omega)} \frac{\omega^2 G(\omega)}{-\omega+\omega'} \qquad \text{(B.16)}\\ &= \frac{\mathcal{P}}{2\mathrm{i}}\int_0^\infty \frac{\mathrm{d}\omega}{(\omega-\omega_{km})} \frac{\partial}{\partial\omega} \frac{\omega^2 G(\omega)}{\omega+\omega'} \\ &\quad - \frac{\mathcal{P}}{2\mathrm{i}}\int_0^{-\infty} \frac{\mathrm{d}\omega}{\omega+\omega_{km}} \frac{\partial}{\partial\omega} \frac{\omega^2 G(\omega)}{\omega-\omega'}. \qquad \text{(B.17)}\end{aligned}$$

With the integration contour from figure B.1, (B.17) can be transformed further,

$$\begin{aligned}\text{(B.17)} &= \frac{1}{2}\int_0^\infty \frac{\mathrm{d}\xi}{(\mathrm{i}\xi-\omega_{km})} \frac{\partial}{\partial\omega} \frac{\omega^2 G(\omega)}{\omega+\omega'}\bigg|_{\omega=\mathrm{i}\xi} - \frac{1}{2}\int_0^\infty \frac{\mathrm{d}\xi}{(\mathrm{i}\xi+\omega_{km})} \frac{\partial}{\partial\omega} \frac{\omega^2 G(\omega)}{\omega-\omega'}\bigg|_{\omega=\mathrm{i}\xi} \\ &\quad + \frac{\pi}{2} \frac{\partial}{\partial\omega} \frac{\omega^2 G(\omega)}{\omega+\omega'}\bigg|_{\omega=\omega_{km}} + \frac{\pi}{2} \frac{\partial}{\partial\omega} \frac{\omega^2 G(\omega)}{\omega-\omega'}\bigg|_{\omega=-\omega_{km}} \qquad \text{(B.18)}\\ &= \int_0^\infty \mathrm{d}\xi \, \frac{\partial}{\partial\omega}\omega^2 G(\omega)\bigg|_{\omega=\mathrm{i}\xi} \mathrm{i}\mathrm{Im}\left[\frac{1}{(\mathrm{i}\xi-\omega_{km})(\mathrm{i}\xi+\omega')}\right] \\ &\quad - \int_0^\infty \mathrm{d}\xi \, (\mathrm{i}\xi)^2 G(\mathrm{i}\xi)\mathrm{Re}\left[\frac{1}{(\mathrm{i}\xi+\omega_{km})(\mathrm{i}\xi+\omega')^2}\right] \qquad \text{(B.19)}\\ &\quad + \frac{\pi}{2} \frac{\partial}{\partial\omega} \frac{\omega^2 G(\omega)}{\omega+\omega'}\bigg|_{\omega=\omega_{km}} + \frac{\pi}{2} \frac{\partial}{\partial\omega} \frac{\omega^2 G(\omega)}{\omega-\omega'}\bigg|_{\omega=-\omega_{km}}\end{aligned}$$

Together with the residue term from (B.15), one arrives at the final result

$$
\begin{aligned}
&\int_0^\infty \mathrm{d}\omega \int_0^\infty \mathrm{d}\omega'\, \mathcal{T}_2 \\
&= \int_0^\infty \mathrm{d}\omega'\, \omega'^2 \mathrm{Im} G(\omega') \times \Bigg\{ \\
&\qquad \int_0^\infty \mathrm{d}\xi \left[\frac{\partial}{\partial\omega} \omega^2 G(\omega) \bigg|_{\omega=\mathrm{i}\xi} \mathrm{iIm} \left[\frac{1}{(\mathrm{i}\xi - \omega_{km})(\mathrm{i}\xi + \omega')} \right] \right. \\
&\qquad\qquad \left. - (\mathrm{i}\xi)^2 G(\mathrm{i}\xi) \mathrm{Re} \left[\frac{1}{(\mathrm{i}\xi - \omega_{km})(\mathrm{i}\xi + \omega')^2} \right] \right] \\
&\qquad + \pi \frac{\partial}{\partial\omega} \frac{\omega^2 G(-\omega)}{\omega + \omega'} \bigg|_{\omega=\omega_{km}} \Bigg\}.
\end{aligned}
\tag{B.20}
$$

Appendix C.

Code from the pairinteraction package

In this appendix, the backend and frontend of the modified PAIRINTERACTION. PAIRINTERACTION is available as open-source along with some tutorials from the website [121]. Weber *et al.* [120] have also written an introductory article. For this work, the Green's tensor formalism was added to PAIRINTERACTION. During the writing of this thesis, corrections were made to the Green's tensor code. These corrections will be published in time.

C.1. Implementation of the Green's tensor

In this section, the implementation of the vacuum Green's tensor and the plate's Green's tensor (A.17) into PAIRINTERACTION is shown. The file GreenTensor.cpp belongs to the PAIRINTERACTION package. Due to the structure of the program the prefactor $1/4\pi$ is left out at this point.

```
//use from dtypes.h
//typedef Eigen::Matrix<double, 3, 3> eigen_matrix33;

//Implementation of vacuum Green's tensor for dipole-dipole interaction
eigen_matrix33 GreenTensor::getDDTensorVacuum(double x, double y, double z
    ) const {
    // Build distance vector
    Eigen::Matrix<double, 3, 1> distance;
    distance << x, y, z;

    // Construct Green tensor
    eigen_matrix33 vacuum_tensor =
        -Eigen::MatrixXd::Identity(3, 3) / std::pow(distance.norm(), 3.) +
```

```
        3. * distance * distance.transpose() / std::pow(distance.norm(),
    5.);

    return vacuum_tensor;
}

//Implementation of scattering Green's tensor of a plate for dipole-dipole
    interaction
eigen_matrix33 GreenTensor::getDDTensorPlate(double x, double zA, double
    zB) const {
    // Calculate distances to mirror dipole
    double zp = zA + zB;
    double rp = std::sqrt(x * x + zp * zp);

    // Construct Green tensor
    eigen_matrix33 plate_tensor_second_matrix;
    plate_tensor_second_matrix << x * x, 0., -x * zp, 0., 0., 0., x * zp,
    0., x * x;

    eigen_matrix33 plate_tensor =
        Eigen::Vector3d({1., 1., 2.}).asDiagonal().toDenseMatrix() / std::
    pow(rp, 3.) -
        3. * plate_tensor_second_matrix / std::pow(rp, 5);

    return plate_tensor;
}
```

C.2. Python frontend

This section briefly shows how to work with PAIRINTERACTION in a Python notebook environment. It shows how to produce figures like figure 4.4 from the main text. This tutorial was written by Sebastian Weber and Johannes Block. It is also published similarly on the PAIRINTERACTION website [121].

Rydberg Pair Potentials Near Surfaces

This tutorial is based on results that were published by J. Block and S. Scheel, "van der Waals interaction potential between Rydberg atoms near surfaces" Phys. Rev. A 96, 062509 (2017) (https://journals.aps.org/pra/abstract/10.1103/PhysRevA.96.062509). We will reproduce the pair potentials shown in Figure 4. The final result is that for states around the $|70p_{3/2}; 70p_{3/2}\rangle$-asymptote of Rubidium the strength of the pair interaction is reduced when placing the atoms in front of a perfect mirror (perfectly conducting plate) compared to the vacuum interaction.

As described in the introduction (https://pairinteraction.github.io/pairinteraction/sphinx/html/introduction.html), we start our code with some preparations and load the necessary modules.

In [1]:
```
%matplotlib inline

# Arrays
import numpy as np

# Plotting
import matplotlib.pyplot as plt
from itertools import product

# Operating system interfaces
import os, sys

# Parallel computing
from multiprocessing import Pool

# pairinteraction :-)
sys.path.append("/your/path/to/pairinteraction/build")
from pairinteraction import pireal as pi

# Create cache for matrix elements
if not os.path.exists("./cache"):
    os.makedirs("./cache")
cache = pi.MatrixElementCache("./cache")
```

The plate lies in the xy-plane with the surface at $z = 0$. The atoms lie in the xz-plane with $z > 0$.

We can set the angle between the interatomic axis and the z-axis `theta` and the center of mass distance from the surface `distance_surface`. `distance_atom` defines the interatomic distances for which the pair potential is plotted. The units of the respective quantities are given as comments.

Be careful: `theta = np.pi/2` corresponds to horizontal alignment of the two atoms with respect to the surface. For different angles, large interatomic distances `distance_atom` might lead to one of the atoms being placed inside the plate. Make sure that `distance_surface` is larger than `distance_atom*np.cos(theta)/2`.

In [2]:
```
theta = np.pi/2 # rad
distance_atom = np.linspace(7, 1.3, 50) # µm
distance_surface = 1 # µm
```

Next we define the state that we are interested in using pairinteraction's `StateOne` class . As shown in Figures 4 and 5 of Phys. Rev. A 96, 062509 (2017) (https://journals.aps.org/pra/abstract/10.1103/PhysRevA.96.062509) we expect large changes for the C_6 coefficient of the $|69s_{1/2}, m_j = 1/2; 72s_{1/2}, m_j = 1/2\rangle$ pair state, so this provides a good example.

We set up the one-atom system using restrictions of energy, main quantum number n and angular momentum l. This is done by means of the `restrict...` functions in `SystemOne` .

In [3]:
```
state_one1 = pi.StateOne("Rb", 69, 0, 0.5, 0.5)
state_one2 = pi.StateOne("Rb", 72, 0, 0.5, 0.5)

# Set up one-atom system
system_one = pi.SystemOne(state_one1.getSpecies(), cache)
system_one.restrictEnergy(min(state_one1.getEnergy(),state_one2.
getEnergy()) - 50, \
                          max(state_one1.getEnergy(),state_one2.
getEnergy()) + 50)
system_one.restrictN(min(state_one1.getN(),state_one2.getN()) -
2, \
                     max(state_one1.getN(),state_one2.getN()) +
2)
system_one.restrictL(min(state_one1.getL(),state_one2.getL()) -
2, \
                     max(state_one1.getL(),state_one2.getL()) +
2)
```

The pair state `state_two` is created from the one atom states `state_one1` and `state_one2` using the `StateTwo` class.

From the previously set up system_one we define system_two using `SystemTwo` class. This class also contains methods `set..` to set angle, distance, surface distance and to `enableGreenTensor` in order implement a surface.

In [4]:
```
# Set up pair state
state_two = pi.StateTwo(state_one1, state_one2)


# Set up two-atom system
system_two = pi.SystemTwo(system_one, system_one, cache)
system_two.restrictEnergy(state_two.getEnergy() - 5, state_two.g
etEnergy() + 5)

system_two.setAngle(theta)
system_two.enableGreenTensor(True)
system_two.setDistance(distance_atom[0])
system_two.setSurfaceDistance(distance_surface)
system_two.buildInteraction()
```

Next, we diagonalize the system for the given interatomic distances in distance_atom and compare the free space system to a system at `distance_surface` away from the perfect mirror. The energy is calculated with respect to a Rubidium $|70p_{3/2}, m_j = 3/2; 70p_{3/2}, m_j = 3/2\rangle$ two atom state, defined in `energyzero` .

In [5]:
```
# Diagonalize the two-atom system for different surface and inte
ratomic distances
def getDiagonalizedSystems(distances):
    system_two.setSurfaceDistance(distances[0])
    system_two.setDistance(distances[1])
    system_two.diagonalize(1e-3)
    return system_two.getHamiltonian().diagonal()

if sys.platform != "win32":
    with Pool() as pool:
        energies = pool.map(getDiagonalizedSystems, product([1e1
2, distance_surface], distance_atom))
else:
    energies = list(map(getDiagonalizedSystems, product([1e12, d
istance_surface], distance_atom)))

energyzero = pi.StateTwo(["Rb", "Rb"], [70, 70], [1, 1], [1.5,
1.5], [1.5, 1.5]).getEnergy()
y = np.array(energies).reshape(2, -1)-energyzero
x = np.repeat(distance_atom, system_two.getNumBasisvectors())
```

In [7]:
```
# Plot pair potentials
fig = plt.figure()
ax = fig.add_subplot(1,1,1)
ax.set_xlabel(r"Distance ($\mu m$)")
ax.set_ylabel(r"Energy (GHz)")
ax.set_xlim(np.min(distance_atom),np.max(distance_atom))
ax.set_ylim(-3, -1.6)
ax.plot(x, y[0], 'ko', ms=3, label = 'free space')
ax.plot(x, y[1], 'ro', ms=3, label = 'perfect mirror')
ax.legend();
```

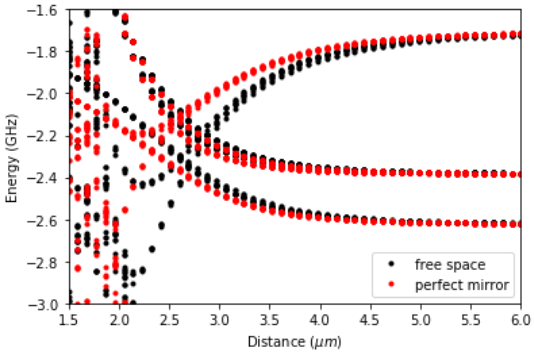

In [ ]:

Appendix D.

List of publications

D.1. Published papers

(I) J. Block and S. Scheel
"van der Waals interaction potential between Rydberg atoms near surfaces"
Phys. Rev. A **96**, 062509 (2017).

(II) J. Block and S. Scheel
"Casimir-Polder-induced Rydberg macrodimers"
Phys. Rev. A **100**, 062508 (2019).

D.2. Conference contributions

(I) 3rd International Conference on "Correlation Effects in Radiation Fields" CERF 2015
Rostock, Germany, 13/09 – 18/09/2015
J. Block and S. Scheel
Poster: "Quantum reflection of the helium dimer".

(II) DPG Spring Meeting 2017 (SAMOP section)
Mainz, Germany, 06/03 – 10/03/2017
J. Block and S. Scheel
Poster: "Van der Waals interactions of Rydberg excitons".

(III) 651. WE-Heraeus-Seminar: Longrange Interactions
Bad Honnef, Germany, 25/10 – 27/10/2017

J. Block and S. Scheel
Poster: “Multipolar interactions of Rydberg particles”.

(IV) DPG Spring Meeting 2018 (SAMOP section)
Erlangen, Germany, 04/03 – 09/03/2017
J. Block and S. Scheel
Talk: “Van der Waals interaction potential between Rydberg atoms near surfaces”.

(V) 2nd International Workshop on Rydberg Excitons in Semiconductors
Aarhus, Denmark, 03/05 – 04/05/2018
J. Block and S. Scheel
Poster: “Van der Waals interactions between Rydberg atoms near surfaces”.

(VI) International Conference on Atomic Physics ICAP 2018
Barcelona, Spain, 22/07 – 27/07/2018
J. Block and S. Scheel
Poster: “Van der Waals interactions of Rydberg particles near surfaces”.

(VII) DPG Spring Meeting 2019 (SAMOP section)
Rostock, Germany, 10/03 – 15/03/2017
J. Block, S. Weber and H. Menke
Poster: “Upgrading pairinteraction”.

Bibliography

[1] T. F. Gallagher, *Rydberg atoms* (Cambridge University Press, Cambridge, 2005).

[2] A. Schramm, J. Weber, J. Kreil, D. Klar, M.-W. Ruf, and H. Hotop, Phys. Rev. Lett. **81**, 778 (1998).

[3] A. Osterwalder and F. Merkt, Phys. Rev. Lett. **82**, 1831 (1999).

[4] J. D. Carter, O. Cherry, and J. Martin, Phys. Rev. A **86**, 053401 (2012).

[5] J. A. Sedlacek, A. Schwettmann, H. Kübler, R. Löw, T. Pfau, and J. P. Shaffer, Nat. Phys. **8**, 819 (2012).

[6] J. Sedlacek, A. Schwettmann, H. Kübler, and J. Shaffer, Phys. Rev. Lett. **111**, 063001 (2013).

[7] H. Fan, S. Kumar, J. Sedlacek, H. Kübler, S. Karimkashi, and J. P. Shaffer, J. Phys. B. Atom. Molec. Phys. **48**, 202001 (2015).

[8] S. Kumar, H. Fan, H. Kübler, A. J. Jahangiri, and J. P. Shaffer, Optics express **25**, 8625 (2017).

[9] D. H. Meyer, Z. A. Castillo, K. C. Cox, and P. D. Kunz, J. Phys. B. Atom. Molec. Phys. **53**, 034001 (2020).

[10] Y. Peng, J. Wang, C. Li, X. Lu, Y. Qi, A. Yang, and J. Wang, Optical and Quantum Electronics **52**, 1 (2020).

[11] W. Vogel and D.-G. Welsch, *Quantum optics* (John Wiley & Sons, 2006).

[12] S. Scheel and S. Buhmann, Acta Phys. Slov. **58**, 675 (2008).

[13] S. Y. Buhmann, *Dispersion Forces I* (Springer Tracts in Modern Physics, 2012).

[14] S. Y. Buhmann, *Dispersion forces II : Many-body effects, excited atoms, finite temperature and quantum friction* (Springer Tracts in Modern Physics, 2012).

[15] H. B. Casimir, in *Proc. Kon. Ned. Akad. Wet.*, Vol. 51 (1948) p. 793.

[16] I. E. Dzyaloshinskii, E. M. Lifshitz, and L. P. Pitaevskii, Phys.-Uspekhi **4**, 153 (1961).

[17] J. N. Munday, F. Capasso, and V. A. Parsegian, Nature **457**, 170 (2009).

[18] M. Gierling, P. Schneeweiss, G. Visanescu, P. Federsel, M. Häffner, D. Kern, T. Judd, A. Günther, and J. Fortágh, Nat. Nanotechnol. **6**, 446 (2011).

[19] M. D. Lukin, M. Fleischhauer, R. Cote, L. Duan, D. Jaksch, J. I. Cirac, and P. Zoller, Phys. Rev. Lett. **87**, 037901 (2001).

[20] M. Saffman, T. G. Walker, and K. Mølmer, Rev. Mod. Phys. **82**, 2313 (2010).

[21] M. Saffman, J. Phys. B. Atom. Molec. Phys. **49**, 202001 (2016).

[22] C. S. Adams, J. D. Pritchard, and J. P. Shaffer, J. Phys. B. Atom. Molec. Phys. **53**, 012002 (2019).

[23] D. Jaksch, J. Cirac, P. Zoller, S. Rolston, R. Côté, and M. Lukin, Phys. Rev. Lett. **85**, 2208 (2000).

[24] M. Safronova, C. J. Williams, and C. W. Clark, Phys. Rev. A **67**, 040303 (2003).

[25] S. E. Anderson, K. Younge, and G. Raithel, Phys. Rev. Lett. **107**, 263001 (2011).

[26] H. Weimer, M. Müller, I. Lesanovsky, P. Zoller, and H. P. Büchler, Nat. Phys. **6**, 382 (2010).

[27] L. Sárkány, J. Fortágh, and D. Petrosyan, Phys. Rev. A **92**, 030303 (2015).

[28] H. Hattermann, D. Bothner, L. Ley, B. Ferdinand, D. Wiedmaier, L. Sárkány, R. Kleiner, D. Koelle, and J. Fortágh, Nature communications **8**, 1 (2017).

[29] H. Safari and M. R. Karimpour, Phys. Rev. Lett. **114**, 013201 (2015).

[30] J. D. Jackson, *Classical electrodynamics* (American Association of Physics Teachers, 1999).

[31] R. Kubo, Rep. Prog. Phys. **29**, 255 (1966).

[32] S. E. Anderson and G. Raithel, Nat. Commun. **4**, 1 (2013).

[33] E. Lifshitz *et al.*, Sov. Phys. JETP **2**, 73 (1956).

[34] S. M. Rytov, V. I. Tatarski, and Y. A. Kravtsov, *Principles of Statistical Radiophysics: Elements of random fields* (Springer-Verlag, 1989).

[35] P. Milonni, Phys. Rev. A **25**, 1315 (1982).

[36] S. K. Lamoreaux, Rep. Prog. Phys. **68**, 201 (2004).

[37] Á. M. Alhambra, A. Kempf, and E. Martín-Martínez, Phys. Rev. A **89**, 033835 (2014).

[38] R. E. Grisenti, W. Schöllkopf, J. P. Toennies, G. C. Hegerfeldt, and T. Köhler, Phys. Rev. Lett. **83**, 1755 (1999).

[39] T. Peyrot, N. Šibalić, Y. Sortais, A. Browaeys, A. Sargsyan, D. Sarkisyan, I. Hughes, and C. Adams, Phys. Rev. A **100**, 022503 (2019).

[40] A. Salam, Long-Range Intermolecular Interactions (2010).

[41] C. Sukenik, M. Boshier, D. Cho, V. Sandoghdar, and E. Hinds, Phys. Rev. Lett. **70**, 560 (1993).

[42] K. A. Milton, E. Abalo, P. Parashar, N. Pourtolami, I. Brevik, and S. Å. Ellingsen, Phys. Rev. A **83**, 062507 (2011).

[43] K. A. Milton, E. Abalo, P. Parashar, N. Pourtolami, I. Brevik, and S. Å. Ellingsen, J. Phys. A Math. Theor. **45**, 374006 (2012).

[44] P. S. Venkataram, S. Molesky, P. Chao, and A. W. Rodriguez, Phys. Rev. A **101**, 052115 (2020).

[45] D. Harber, J. Obrecht, J. McGuirk, and E. A. Cornell, Phys. Rev. A **72**, 033610 (2005).

[46] H. Bender, P. Courteille, C. Zimmermann, and S. Slama, Appl. Phys. B **96**, 275 (2009).

[47] F. Shimizu, Phys. Rev. Lett. **86**, 987 (2001).

[48] V. Druzhinina and M. DeKieviet, Phys. Rev. Lett. **91**, 193202 (2003).

[49] T. A. Pasquini, Y. Shin, C. Sanner, M. Saba, A. Schirotzek, D. E. Pritchard, and W. Ketterle, Phys. Rev. Lett. **93**, 223201 (2004).

[50] A. Y. Voronin and P. Froelich, J. Phys. B. Atom. Molec. Phys. **38**, L301 (2005).

[51] P.-P. Crépin, E. Kupriyanova, R. Guérout, A. Lambrecht, V. Nesvizhevsky, S. Reynaud, S. Vasiliev, and A. Y. Voronin, EPL **119**, 33001 (2017).

[52] J. J. Balmer, Annalen der physik **261**, 80 (1885).

[53] X. Ling, B. Lindsay, K. Smith, and F. Dunning, Phys. Rev. A **45**, 242 (1992).

[54] S. Ye, X. Zhang, T. C. Killian, F. B. Dunning, M. Hiller, S. Yoshida, S. Nagele, and J. Burgdörfer, Phys. Rev. A **88**, 043430 (2013).

[55] C. L. Holloway, J. A. Gordon, S. Jefferts, A. Schwarzkopf, D. A. Anderson, S. A. Miller, N. Thaicharoen, and G. Raithel, IEEE Transactions on Antennas and Propagation **62**, 6169 (2014).

[56] D. B. Branden, T. Juhasz, T. Mahlokozera, C. Vesa, R. O. Wilson, M. Zheng, A. Kortyna, and D. A. Tate, J. Phys. B. Atom. Molec. Phys. **43**, 015002 (2009).

[57] T. G. Walker and M. Saffman, Phys. Rev. A **77**, 032723 (2008).

[58] D. Tong, S. Farooqi, J. Stanojevic, S. Krishnan, Y. Zhang, R. Côté, E. Eyler, and P. Gould, Phys. Rev. Lett. **93**, 063001 (2004).

[59] V. Vuletic, Nat. Phys. **2**, 801 (2006).

[60] O. Firstenberg, C. S. Adams, and S. Hofferberth, J. Phys. B. Atom. Molec. Phys. **49**, 152003 (2016).

[61] Y. Dudin and A. Kuzmich, Science **336**, 887 (2012).

[62] F. Ripka, H. Kübler, R. Löw, and T. Pfau, Science **362**, 446 (2018).

[63] M. Saffman and T. Walker, Phys. Rev. A **66**, 065403 (2002).

[64] I. Beterov, M. Saffman, E. Yakshina, D. Tretyakov, V. Entin, G. Hamzina, and I. Ryabtsev, J. Phys. B. Atom. Molec. Phys. **49**, 114007 (2016).

[65] M. Fleischhauer and M. D. Lukin, Phys. Rev. A **65**, 022314 (2002).

[66] S. Beck and I. E. Mazets, Phys. Rev. A **95**, 013818 (2017).

[67] E. Urban, T. A. Johnson, T. Henage, L. Isenhower, D. D. Yavuz, T. G. Walker, and M. Saffman, Nat. Phys. **5**, 110 (2009).

[68] C. H. Greene, A. S. Dickinson, and H. R. Sadeghpour, Phys. Rev. Lett. **85**, 2458 (2000).

[69] V. Bendkowsky, B. Butscher, J. Nipper, J. P. Shaffer, R. Löw, and T. Pfau, Nature **458**, 1005 (2009).

[70] B. Butscher, V. Bendkowsky, J. Nipper, J. B. Balewski, L. Kukota, R. Löw, T. Pfau, W. Li, T. Pohl, and J. M. Rost, J. Phys. B. Atom. Molec. Phys. **44**, 184004 (2011).

[71] H. Saßmannshausen, J. Deiglmayr, and F. Merkt, Eur. Phys. J. ST **225**, 2891 (2016).

[72] J. P. Shaffer, S. T. Rittenhouse, and H. R. Sadeghpour, Nat. Commun. **9**, 1965 (2018).

[73] M. T. Eiles, J. Phys. B. Atom. Molec. Phys. **52**, 113001 (2019).

[74] E. L. Hamilton, C. H. Greene, and H. Sadeghpour, J. Phys. B. Atom. Molec. Phys. **35**, L199 (2002).

[75] T. Schmid, C. Veit, N. Zuber, R. Löw, T. Pfau, M. Tarana, and M. Tomza, Phys. Rev. Lett. **120**, 153401 (2018).

[76] J. A. Fernández, P. Schmelcher, and R. González-Férez, J. Phys. B. Atom. Molec. Phys. **49**, 124002 (2016).

[77] C. Boisseau, I. Simbotin, and R. Côté, Phys. Rev. Lett. **88**, 133004 (2002).

[78] S. M. Farooqi, D. Tong, S. Krishnan, J. Stanojevic, Y. P. Zhang, J. R. Ensher, A. S. Estrin, C. Boisseau, R. Côté, E. E. Eyler, and P. L. Gould, Phys. Rev. Lett. **91**, 183002 (2003).

[79] H. Saßmannshausen and J. Deiglmayr, Phys. Rev. Lett. **117**, 083401 (2016).

[80] S. Hollerith, J. Zeiher, J. Rui, A. Rubio-Abadal, V. Walther, T. Pohl, D. M. Stamper-Kurn, I. Bloch, and C. Gross, Science **364**, 664 (2019).

[81] N. Samboy and R. Côté, Phys. Rev. A **87**, 032512 (2013).

[82] N. Kryukov and E. Oks, Eur. Phys. J. D **74**, 82 (2020).

[83] F. Merkt, Annu. Rev. Phys. Chem. **48**, 675 (1997).

[84] E. Gross, Il Nuovo Cimento (1955-1965) **3**, 672 (1956).

[85] A. Chernikov, T. C. Berkelbach, H. M. Hill, A. Rigosi, Y. Li, O. B. Aslan, D. R. Reichman, M. S. Hybertsen, and T. F. Heinz, Phys. Rev. Lett. **113**, 076802 (2014).

[86] T. Wang, Z. Li, Y. Li, Z. Lu, S. Miao, Z. Lian, Y. Meng, M. Blei, T. Taniguchi, K. Watanabe, *et al.*, Nano Letters **20**, 7635 (2020).

[87] T. Kazimierczuk, D. Fröhlich, S. Scheel, H. Stolz, and M. Bayer, Nature **514**, 343 (2014).

[88] M. A. Versteegh, S. Steinhauer, J. Bajo, T. Lettner, A. Soro, A. Romanova, S. Gyger, L. Schweickert, A. Mysyrowicz, and V. Zwiller, arXiv preprint arXiv:2105.07942 (2021).

[89] J. Thewes, J. Heckötter, T. Kazimierczuk, M. Aßmann, D. Fröhlich, M. Bayer, M. Semina, and M. Glazov, Phys. Rev. Lett. **115**, 027402 (2015).

[90] S. O. Krüger and S. Scheel, Phys. Rev. B **100**, 085201 (2019).

[91] M. Khazali, K. Heshami, and C. Simon, J. Phys. B. Atom. Molec. Phys. **50**, 215301 (2017).

[92] M. Donaire, M. P. Gorza, A. Maury, R. Guérout, and A. Lambrecht, EPL **109**, 24003 (2015).

[93] A. Ashourvan, M. Miri, and R. Golestanian, Phys. Rev. Lett. **98**, 140801 (2007).

[94] S. Scheel, S. Y. Buhmann, C. Clausen, and P. Schneeweiss, Phys. Rev. A **92**, 043819 (2015).

[95] A. Manjavacas, F. J. Rodríguez-Fortuño, F. J. G. De Abajo, and A. V. Zayats, Phys. Rev. Lett. **118**, 133605 (2017).

[96] S. Koller, M. Grifoni, M. Leijnse, and M. Wegewijs, Phys. Rev. B **82**, 235307 (2010).

[97] S. Koller, *Spin phenomena and higher order effects in transport across interacting quantum-dots*, Ph.D. thesis, Universität Regensburg (2010).

[98] D. A. Steck, "Rubidium 87 d line data," `https://steck.us/alkalidata` (2003).

[99] S. Y. Buhmann, M. R. Tarbutt, S. Scheel, and E. A. Hinds, Phys. Rev. A **78**, 052901 (2008).

[100] F. Reiter and A. S. Sørensen, Phys. Rev. A **85**, 032111 (2012).

[101] T. Amthor, M. Reetz-Lamour, S. Westermann, J. Denskat, and M. Weidemüller, Phys. Rev. Lett. **98**, 023004 (2007).

[102] M. Reetz-Lamour, J. Deiglmayr, T. Amthor, and M. Weidemüller, New J. Phys. **10**, 045026 (2008).

[103] L. Beguin, A. Vernier, R. Chicireanu, T. Lahaye, and A. Browaeys, Phys. Rev. Lett. **110**, 263201 (2013).

[104] R. Faoro, C. Simonelli, M. Archimi, G. Masella, M. Valado, E. Arimondo, R. Mannella, D. Ciampini, and O. Morsch, Phys. Rev. A **93**, 030701 (2016).

[105] J. Block and S. Scheel, Phys. Rev. A **96**, 062509 (2017).

[106] J. Block and S. Scheel, Phys. Rev. A **100**, 062508 (2019).

[107] C.-T. Tai, *Dyadic Green functions in electromagnetic theory* (IEEE, 1994).

[108] S. Baur, D. Tiarks, G. Rempe, and S. Dürr, Phys. Rev. Lett. **112**, 073901 (2014).

[109] H. T. Dung, S. Y. Buhmann, and D.-G. Welsch, Phys. Rev. A **74**, 023803 (2006).

[110] J. A. Crosse, S. Å. Ellingsen, K. Clements, S. Y. Buhmann, and S. Scheel, Phys. Rev. A **82**, 010901(R) (2010).

[111] J. Stanojevic, R. Côté, D. Tong, E. E. Eyler, and P. L. Gould, Phys. Rev. A **78**, 052709 (2008).

[112] J. S. Cabral, J. M. Kondo, L. F. Gonçalves, V. A. Nascimento, L. G. Marcassa, D. Booth, J. Tallant, A. Schwettmann, K. R. Overstreet, J. Sedlacek, and J. P. Shaffer, J. Phys. B. Atom. Molec. Phys. **44**, 184007 (2011).

[113] W. Li, I. Mourachko, M. Noel, and T. Gallagher, Phys. Rev. A **67**, 052502 (2003).

[114] J. Han, Y. Jamil, D. Norum, P. J. Tanner, and T. Gallagher, Phys. Rev. A **74**, 054502 (2006).

[115] J. E. Sansonetti, J. Phys. Chem. Ref. Data **35**, 301 (2006).

[116] J. E. Sansonetti, J. Phys. Chem. Ref. Data **37**, 1183 (2008).

[117] M. Mack, F. Karlewski, H. Hattermann, S. Höckh, F. Jessen, D. Cano, and J. Fortágh, Phys. Rev. A **83**, 052515 (2011).

[118] J. Blatt, J. Comput. Phys **1**, 382 (1967).

[119] N. Šibalić, J. D. Pritchard, C. S. Adams, and K. J. Weatherill, Comput. Phys. Commun. **220**, 319 (2017).

[120] S. Weber, C. Tresp, H. Menke, A. Urvoy, O. Firstenberg, H. P. Büchler, and S. Hofferberth, J. Phys. B. Atom. Molec. Phys. **50**, 133001 (2017).

[121] S. Weber, C. Tresp, H. Menke, A. Urvoy, O. Firstenberg, H. P. Büchler, and S. Hofferberth, "Pairinteraction - a rydberg interaction calculator," `https://www.`

pairinteraction.org (2017).

[122] J. Crosse and S. Scheel, Phys. Rev. A **79**, 062902 (2009).

[123] J. Deiglmayr, Phys. Scr. **91**, 104007 (2016).

[124] J. Deiglmayr, H. Saßmannshausen, P. Pillet, and F. Merkt, Phys. Rev. Lett. **113**, 193001 (2014).

[125] A. Schwettmann, K. R. Overstreet, J. Tallant, and J. P. Shaffer, J. Mod. Opt. **54**, 2551 (2007).

[126] A. Chakraborty, S. Mishra, S. Ram, S. Tiwari, and H. Rawat, J. Phys. B **49**, 075304 (2016).

[127] I. I. Beterov, I. I. Ryabtsev, D. B. Tretyakov, and V. M. Entin, Phys. Rev. A **79**, 052504 (2009).

[128] X. Han, S. Bai, Y. Jiao, L. Hao, Y. Xue, J. Zhao, S. Jia, and G. Raithel, Phys. Rev. A **97**, 031403(R) (2018).

[129] C. W. Clark, Phys. Lett. A **70**, 295 (1979).

[130] A. Thiel, J. Phys. G **16**, 867 (1990).

[131] N. Samboy, Phys. Rev. A **95**, 032702 (2017).

[132] N. Ashcroft and N. Mermin, *Solid State Physics* (Saunders College Publishing, Fort Worth, 1976).

[133] R. Legaie, C. J. Picken, and J. D. Pritchard, JOSA B **35**, 892 (2018).

[134] A. Tauschinsky, R. M. T. Thijssen, S. Whitlock, H. B. van Linden van den Heuvell, and R. J. C. Spreeuw, Phys. Rev. A **81**, 063411 (2010).

[135] G. Epple, K. S. Kleinbach, T. G. Euser, N. Y. Joly, T. Pfau, P. S. J. Russell, and R. Löw, Nat. Commun. **5**, 4132 (2014).

[136] M. Langbecker, M. Noaman, N. Kjaergaard, F. Benabid, and P. Windpassinger, Phys. Rev. A **96**, 041402(R) (2017).

[137] H. Hattermann, M. Mack, F. Karlewski, F. Jessen, D. Cano, and J. Fortágh, Phys. Rev. A **86**, 022511 (2012).

[138] J. Sedlacek, E. Kim, S. Rittenhouse, P. Weck, H. Sadeghpour, and J. Shaffer, Phys. Rev. Lett. **116**, 133201 (2016).

[139] A. R. Barnea, B. A. Stickler, O. Cheshnovsky, K. Hornberger, and U. Even, Phys. Rev. A **95**, 043639 (2017).

[140] J. Petersen, E. Pollak, and S. Miret-Artes, Phys. Rev. A **97**, 042102 (2018).

[141] G. Rojas-Lorenzo, J. Rubayo-Soneira, S. Miret-Artés, and E. Pollak, Phys. Rev. A **98**, 063604 (2018).

[142] S. Hollerith, J. Rui, A. Rubio-Abadal, K. Srakaew, D. Wei, J. Zeiher, C. Gross, and I. Bloch, Phys. Rev. Res. **3**, 013252 (2021).

[143] J. Gurian, P. Cheinet, P. Huillery, A. Fioretti, J. Zhao, P. Gould, D. Comparat, and P. Pillet, Phys. Rev. Lett. **108**, 023005 (2012).

[144] D. Petrosyan and K. Mølmer, Phys. Rev. Lett. **113**, 123003 (2014).

[145] M. Khazali and K. Mølmer, Phys. Rev. X **10**, 021054 (2020).

[146] S. D. Hogan, J. A. Agner, F. Merkt, T. Thiele, S. Filipp, and A. Wallraff, Phys. Rev. Lett. **108**, 063004 (2012).

[147] A. Morgan and S. Hogan, Phys. Rev. Lett. **124**, 193604 (2020).

[148] T. Thiele, J. Deiglmayr, M. Stammeier, J.-A. Agner, H. Schmutz, F. Merkt, and A. Wallraff, Phys. Rev. A **92**, 063425 (2015).

[149] T. F. Gallagher and P. Pillet, Adv. At. Mol. Opt. Phys. **56**, 161 (2008).

Acknowledgements

This work was supported financially by the Landesgraduiertenförderung Mecklenburg-Vorpommern and the Deutsche Forschungsgemeinschaft (DFG) within the SPP 1929 'Giant Interactions in Rydberg Systems' (GiRyd).

Personally, I would like thank Prof. Dr. Stefan Scheel for his supervision, his knowledge and, last not least, his patience. I would like to thank the whole working group Quantenoptik makroskopischer Systeme at Universität Rostock for many discussions, many of them regarding physics. Both the bare knowledge and their ability to ask the right questions of Dr. Sjard-Ole Krüger, Dr. Dirk Semkat, Dr. Florian Schöne, Dr. Lucas Teuber, Dr. Markus Kurz, Dr. Wijnand Broer, Dr. Johannes Fiedler, Thomas Stielow, Helge Dobbertin, Robin Schmidt and Julien Pinske contributed significantly to this work. Many of the seminars I was privileged to hold to enlighten younger students would not have been possible without the help Prof. Dr. Oliver Kühn, Prof. Dr. Ronald Redmer, Prof. Dr. Boris Hage, Martin Preising, Sergey Bokarev and of course again Prof. Dr. Stefan Scheel. Any PhD student, and everyone else at a university for that matter, also benefits significantly from great non-academic staff. I would like to thank Peggy Preuss for managing everything from our conference trips to buying new hardware or birthday presents.

Sebastian Weber from Universiät introduced me to PAIRINTERACTION and helped a lot with the implementation of the Green's tensor formalism. It was really great to work on somebody else's piece of software and be able to contribute to it.

Although sometimes more non-academic, the discussions during coffee break were always worth it to take the two-door and later half-hallway journey for some fresh coffee. Therefore, I would also like to thank Prof. Dr.

Heinrich Stolz, Prof. Dr. Wolf Kraefft and also the other aforementioned coffee drinkers.

Next up is my girlfriend Ines. While she has a great number of positive character traits she also put the kind of ultimate pressure on me by simply moving to New Zealand leaving me with a fixed deadline. That was probably the best motivation there could be.

Talking about ultimate, I would like to thank everyone that has ever played Ultimate Frisbee with me and of course especially the Rostock team Endzonis. I have great memories both on and off the pitch and practice and tournaments were the much needed distraction from the rest. On the other hand, I would not unconditionally like to thank Ultimate Frisbee itself because the distraction was probably sometimes too much.

Finally, I would also like to thank all my other friends and last not least my parents and my sister. Their optimism, jokes and tolerance of my jokes helped me through a lot. Without all of you, I could have never written this thesis.